

Role of Oxygen Vacancies on Ferromagnetism in Oxide Dilute Magnetic Semiconductors (CeO₂/TiO₂)

by

Md. Abdullah Al Mamun

Student ID: 0417172002

This thesis paper is submitted in partial fulfillment of the requirements
for the degree of

MASTER OF SCIENCE

in

Glass and Ceramic Engineering



Department of Glass and Ceramic Engineering

BANGLADESH UNIVERSITY OF ENGINEERING AND TECHNOLOGY

Dhaka-1000, Bangladesh

February 12, 2020

CANDIDATE'S DECLARATION

IT IS HEREBY DECLARED THAT THIS THESIS PAPER OR ANY PART OF
IT HAS NOT BEEN SUBMITTED ANYWHERE ELSE FOR THE AWARD OF
ANY DEGREE

Md. Abdullah Al Mamun

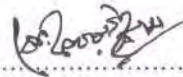
.....

Md. Abdullah Al Mamun

M.Sc. Engineering, GCE, BUET

The thesis titled “Role of Oxygen Vacancies on Ferromagnetism in Oxide Dilute Magnetic Semiconductors (CeO₂/TiO₂)” submitted by Md. Abdullah Al Mamun, Student No. 0417172002, Session April 2017, has been accepted as satisfactory in partial fulfillment of the requirements for the degree of Master of Science in Glass and Ceramic Engineering on February 12, 2020.

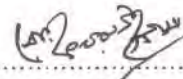
Board of Examiners



Chairman

Dr. Md. Fakhru Islam

Professor, Dept. of Glass & Ceramic Engineering, BUET, Dhaka-1000



Head

Member (Ex-Officio)

Dept. of Glass & Ceramic Engineering, BUET, Dhaka-1000



Member

Dr. Md. Abdullah Zubair

Assistant Professor, Dept. of Glass & Ceramic Engineering, BUET, Dhaka-1000



Member

Dr. Muhammad Hasanuzzaman

Assistant Professor, Dept. of Glass & Ceramic Engineering, BUET, Dhaka-1000



Member (External)

Dr. Md. Rezwan Khan

Professor and Director, Institute of Engineering & Scientific Research (IESR)
Dept. of Electrical & Electronic Engineering, United International University
(UIU), Dhaka-1212

To Almighty Allah

&

To my beloved parents and family

ACKNOWLEDGEMENTS

In the Name of Allah, the Most Gracious and the Most Merciful

Alhamdulillah, all praises to Almighty Allah for the strengths and His blessing in completing this thesis. I would like to thank my supervisor **Dr. Md. Fakhrul Islam** for giving me the opportunity to work in the department of Glass and Ceramic Engineering at BUET. There are not enough words for expressing my sincere gratitude for his willingness to share his knowledge with me through numerous discussions and support since the time of my coursework to completion this degree.

I am immensely grateful to **Dr. A. K. M. Abdul Hakim** for his interest in my work, and encouragement and insight through these years. It was his guidance and support that helped me through all the difficult time. I will surely benefit from his creative thoughts, suggestions and dedication throughout the rest of my life. The same gratitude goes to **Dr. M. A. Matin** for his kind help and support on my research and my life during the past two years.

I also want to thank **Dr. Md. Abdullah Zubair** for thoughtful discussions and sharing his knowledge which inspired me to become a perfectionist researcher in coming years. I would like to express a special word of thanks to my teachers **Dr. Muhammad Hasanuzzaman, Arman Hussain & Mehedi Hasan Rizvi** for their continuous support and inspiration during my M.Sc. study.

My warmest thanks go to **Dr. S. A. M. Tofail** from University of Limerick, Ireland for giving his valuable time and thoughts for my thesis work including the state of the art laboratory facilities to characterize my samples. I would like to express my gratitude to **Dr. Vasily Lebedev** and **Dr. Karrina McNamara** at University of Limerick, Ireland for carrying out the TEM and XPS measurements of my samples. I also want to thank **Dr. Sheikh Manjura Hoque**, Chief Scientific Officer and Head, Materials Science Division, Atomic Energy Centre, Bangladesh Atomic Energy Commission, for her support with the magnetic characterization facilities.

I would like to convey my heartiest regards to all of the faculty members, technical and official staff of Department of Glass and Ceramic Engineering at BUET for their assistance and cooperation during this whole time.

Finally, I want to thank my beloved parents and my wife **Manifa Noor** for being there for me. Without their love, understanding and encouragement, this work would be close to impossible to finish.

ABSTRACTS

The fascinating concept of substituting the cation of oxide based dilute magnetic semiconductors (DMS) with transition/rare earth metal ions shows tremendous prospects because of their usefulness in ultrafast spin-charge transport phenomena and their applications. The aim of this thesis is focused on studying the effects of Sm^{3+} substitution for Ti^{4+} ion in TiO_2 lattice from 0 mol% to as high as 20 mol%. Both X-Ray diffraction and electron diffraction analysis show that the substitution of Sm inhibited the grain growth and phase transition from Anatase to Rutile. The particle size distribution estimated from Transmission Electron Microscopy (TEM) shows that particle size was reduced from $53(\pm 10)$ nm to $10(\pm 3)$ nm due to addition of Sm content. The photoluminescence and UV-Vis-NIR spectroscopy suggest that all samples exhibit indirect bandgap and addition of Sm content reduces the bandgap because of the presence of shallow trap centers created by oxygen vacancies just below the conduction band. The magnetization vs. applied field (M-H) exhibit dilute ferromagnetic behavior at 300 K for all samples while an evolution of paramagnetic response along with ferromagnetic behavior was noticed with increasing Sm content at 5 K which might be attributed to the presence of the amorphous samarium oxide. Such promising results suggest that the role of oxygen vacancies in formation of amorphous second phase of bulk dopants which might contribute to the net ferromagnetic behavior of dilute magnetic semiconductors (DMS) are worthy of further investigation.

Contents

1	Introduction	1
1.1	Background of the research	1
1.2	Dilute Magnetic Semiconductors (DMS)	2
1.3	Current challenges in DMS research	4
1.4	Objective of this research	4
1.5	Thesis overview	5
2	Literature Review	6
2.1	X-ray Absorption Spectroscopy	6
2.2	X-ray Magnetic Circular Dichroism	7
2.3	Angle Resolved Photoemission Spectroscopy	8
2.4	Recent advances in DMS research	9
2.5	Origin of ferromagnetism in DMS	14
2.6	Role of oxygen vacancy in oxide based DMS	16
2.7	Prospects of TiO ₂ as DMS	17
3	Experimental Methodology	20
3.1	Materials synthesis	20
3.2	X-Ray Diffraction	22
3.3	X-Ray Photoelectron Spectroscopy	23
3.4	DSC And TG	24
3.5	FESEM and EDS	24
3.6	TEM, SAED and STEM-EDX	24
3.7	Photoluminescence and UV-Vis-NIR Spectroscopy	24
3.8	Vibrating Sample Magnetometer	25
4	Results & Discussions	26
4.1	Structural analysis by X-Ray Diffraction	26
4.2	Thermal property analysis by DSC-TG	30
4.3	Morphology analysis by FESEM	31
4.4	Structural and morphology analysis by Transmission Electron Microscopy	33
4.5	Chemical and electronic states analysis by XPS	37
4.6	Optical property analysis by UV-Vis-NIR and Photoluminescence Spectroscopy	41
4.7	Magnetic property analysis by Vibrating Sample Magnetometer	44
5	Conclusions	48
6	Suggestions for future work	50

List of Figures

1.1	(a-c) Difference between ferromagnetic material, non-ferromagnetic material and dilute magnetic semiconductor. (d-i) Density of states of different types of semiconductor, ideal half metal and half-metallic semiconductors	3
2.1	Schematic principle of X-ray absorption spectroscopy. (images are taken from the webpage of SLAC, Stanford University)	6
2.2	Difference in 3d orbital due to crystal field splitting in Fe^{3+}	7
2.3	(a) Schematic principle of X-ray magnetic circular dichroism (XMCD) (b) Difference between XAS and XMCD principle [20]	8
2.4	Schematic diagram of angle resolved photoemission spectroscopy	8
2.5	(a) Magnetic-field vs. Hall resistivity ρ_{Hall} and resistivity ρ of $Ga_{(1-x)}Mn_xAs$ vs. temperature. Mn concentration is $x=0.053$. The change of spontaneous magnetization M_s with temperature is showed in inset [4] (b) X-ray absorption and X-ray magnetic circular dichroism spectra of $Ga_{0.98}Mn_{0.02}As$ [22]	9
2.6	(a) Magnetization vs. temperature of as-implanted and laser annealed (A and B) $In_{0.95}Mn_{0.05}P$ samples (b) XAS and XMCD study of $In_{0.95}Mn_{0.05}P$ [23]	10
2.7	Experimental observation of half-metallic behavior in $Ga_{0.97}Mn_{0.03}As$ by Hard X-ray angle resolved photoemission spectroscopy [25]	10
2.8	Experimental observation of half-metallic behavior in $Ga_{0.975}Mn_{0.025}As$ by soft X-ray angle resolved photoemission spectroscopy [26]	11
2.9	(a) Bound magnetic polaron controlling the ferromagnetism in $Ga_{0.975}Mn_{0.025}As$. (b) Schematic image of magnetic interaction in $Ga_{0.975}Mn_{0.025}As$ crystal structure [26]	11
2.10	Magnetization vs. applied field in $Zn_{(1-x)}Cr_xTe$ [29]	12
2.11	(a) Magnetization vs. applied field (b) Magnetization vs. temperature graph of $Ti_{0.93}Co_{0.07}O_2$ sample [9]	12
2.12	Intrinsic ferromagnetism in transition metal doped TiO_2 thin films	13
2.13	(a) Magnetization vs. applied field (b) XAS and (c) XMCD spectra of $Ti_{0.95}Co_{0.05}O_2$ thin film [39]	13
2.14	Bright field STEM image of $Ti_{0.90}Co_{0.10}O_2$ grown on $LaAlO_3$ substrate. The HAADF and EDX images show the homogeneous doping of Cobalt in TiO_2 [38]	13
2.15	Magnetization vs. applied field in $Ti_{(1-x)}Co_xO_2$ nanoparticles [49]	14
2.16	Dilute ferromagnetism observed in undoped non-magnetic oxides due to oxygen vacancies [14]	15
2.17	RKKY type exchange interaction of frustrated spins in $CePO_4$ [50]	15

2.18	Role of oxygen vacancies in CeO_2 [59]	17
2.19	Crystal Structure of three polymorphs of TiO_2 ($\alpha = \beta = \gamma = 90^\circ$ for all polymorphs)	18
2.20	Difference in bond length and bond angles in rutile and anatase TiO_2	19
3.1	Annealing cycle for Pristine TiO_2 and $Ti_{1-x}Sm_xO_2$ ($x = 5, 10, 15$ and 20%)	22
3.2	(a) Principle of X-Ray Diffraction (b) Schematic geometry of X-Ray Diffractometer	23
3.3	Principle of X-ray photoelectron spectroscopy	23
4.1	(a) X – ray diffraction patterns of Pristine TiO_2 samples annealed at 400, 500 and 600 °C (b) Comparison between pristine TiO_2 samples annealed at 600 and 700 °C. In 700 °C annealed sample, a small percentage of rutile TiO_2 was noticed which was absent in 600 °C annealed TiO_2 sample.	26
4.2	(a) & (b) X – ray diffraction patterns of $Ti_{(1-x)}Sm_{(x)}O_2$ samples annealed at 400 and 700 °C.	27
4.3	(a) Slowly scanned X – ray diffraction patterns of $Ti_{(1-x)}Sm_{(x)}O_2$ samples annealed at 700 °C. (b) Comparison between fast scanned and slow scanned XRD patterns of $Ti_{0.8}Sm_{0.2}O_2$ sample.	27
4.4	(a-e) Rietveld refinement patterns of $Ti_{(1-x)}Sm_{(x)}O_2$ samples. The observed and calculated data are showed as red filled circle and black straight line respectively. The difference between observed and calculated values is plotted with blue straight line. The Bragg peak positions for Anatase and Sm_2O_3 are showed with vertical lines. (f-g) The estimated lattice parameters from rietveld refinement. The polynomial curve fitting clearly shows a deviation of Vegard’s law for the higher percentage of Sm substitution in TiO_2	28
4.5	X-Ray Diffraction patterns of pure Sm_2O_3 and mechanically mixed pure Sm_2O_3 with pure TiO_2	29
4.6	DSC-TG analysis of pure and Sm: TiO_2 samples	30
4.7	Field emission scanning electron microscopy images of Pristine, 5 and 10% Sm: TiO_2 samples	31
4.8	Field emission scanning electron microscopy images of 15 and 20% Sm: TiO_2 samples	32
4.9	Energy dispersive X-ray analysis of elemental composition of 5 and 10% Sm: TiO_2 samples	32
4.10	Energy dispersive X-ray analysis of elemental composition of 15 and 20% Sm: TiO_2 samples	33
4.11	(a-f) Comparison of TEM images and grain size distributions of Pristine and 5% Sm: TiO_2 samples	33
4.12	(a-i) Comparison of TEM images and grain size distributions of 10, 15 and 20% Sm: TiO_2 samples	34
4.13	High Resolution TEM images and their corresponding FFT images for lattice spacing estimation of Pristine TiO_2	35
4.14	Comparison of Selective Area Electron Diffraction (SAED) patterns of Pristine, 5% and 15% Sm: TiO_2 samples	36

4.15	EDX mapping shows the homogeneous distribution of Sm, O and Ti in 5% and 15% Sm:TiO ₂ samples	37
4.16	X-ray photoelectron spectra of Pristine and 5% Sm:TiO ₂ samples . . .	38
4.17	X-ray photoelectron spectra of C 1s in 5% Sm:TiO ₂ sample	39
4.18	X-ray photoelectron spectra of O 1s in 5% Sm:TiO ₂ sample	39
4.19	X-ray photoelectron spectra of Ti 2p in 5% Sm:TiO ₂ sample	40
4.20	X-ray photoelectron spectra of Sm 3d in 5% Sm:TiO ₂ sample	40
4.21	Valence band spectra of pristine and 5% Sm:TiO ₂ samples	41
4.22	Absorption spectra of pristine and Sm:TiO ₂ samples obtained from diffused reflectance spectroscopy	41
4.23	Optical bandgap of pristine and Sm:TiO ₂ samples estimated by using Kubelka-Munk function	42
4.24	(a) Photoluminescence of Pristine TiO ₂ and 5% Sm:TiO ₂ (<i>excitation wavelength=270 nm</i>) (b) Energy level diagram of anatase TiO ₂ (c-i) Fitted curve of PL spectra	43
4.25	M-H graph of Pristine TiO ₂	44
4.26	M-H graph of 5% Sm:TiO ₂	45
4.27	M-H graph of 10% Sm:TiO ₂	45
4.28	M-H graph of 15% Sm:TiO ₂	46
4.29	M-H graph of 20% Sm:TiO ₂	46
4.30	Magnetization vs. applied field of pristine and Sm:TiO ₂ samples at 5 K and 300 K	47

CHAPTER 1

INTRODUCTION

1.1 Background of the research

Modern technology stands on the shoulder of semiconductor materials for their immensely useful adaptabilities of physical properties specially the electrical conductivity with an applied electrical field. Despite of having superior conductivity, metals have been outcast by the uniqueness of semiconductor materials in controlling the flow of current. For example, in order to perform a logic function, the ability to distinguish between one and zero is necessary. Semiconductor materials have the capability to transform from insulating to conducting with the help of very small amount of voltage known as gate voltage. When the gate voltage is above a certain level, current flows through a small channel between source and drain; making the material conductive. Again, this flow of current is interrupted when gate voltage is below the level. This directional flow of current in semiconductor is basically driven by very dilute concentration of dopants into a host semiconductor (i.e. 10^{13} to 10^{18} dopant atoms/cm³ in Si as host material which contains 5×10^{22} atoms/cm³). By inducing such excess or shortage of electrons via doping, variable electrical resistance can be achieved which makes semiconductor materials useful for switching, amplification or energy conversion applications. This class of semiconductor is known as Transistor and they led the most important paradigm shift in technology by miniturization of devices which in turns reduces the energy utilization by thousand folds. The placement of these transistors on the integrated circuit (IC) is important because the more miniaturized dense IC could be made, the less heat loss would happen which eventually will raise the speed of information process. In 1965, Gordon Moore, one of the cofounder of Intel, predicted that the number of transistors placed on an IC will double in every two years. Companies like Intel, Samsung and NVidia are now fabricating transistors less than 20 nm in size at mass scale and NVidia's new graphics card GF100 is an example of how dense miniaturized a device can become which contains more than 3 Billion transistors. But, this miniaturization to speed up the information process has now reached its saturation limit since it is almost at the edge of atomic scale. On the other side, we are producing more than 2.5 quintillion bytes of data everyday according to Forbes. With days passing by, we are becoming fonder of online based social and financial activities. The energy required for processing this large amount of data is causing global warming at an increased alarming rate. As, the miniaturization of device can no longer provide benefits to us in energy conservation via faster communication, we now must have to think otherwise.

In electronics, only the charge of the electron is utilized while it's another degree of freedom "Spin" remains less remembered. If the spin states can be incorporated with electronic charge to store and process information, the communication will increase by many folds which has been a fascination for decades. Spintronics, an

acronym for SPIN TRansport electrONICS, is one of such promising areas which brought us the novel concept of utilizing both the charge and spin of the electrons. Apart from the formerly known classical states of electron's spinning i.e. rotating clockwise or anticlockwise, there are infinite number of spin states that an electron can possess according to quantum mechanics. If these spin states could be controlled like the current flow in transistor, we would have more options beside the conventional switching technique i.e. current off(0) or on(1). That being said, the electrons carry the spin state must be non-volatile as well as spin polarized and the ferromagnetism needs to be capable of gating. For example, Kreutz *et al.* showed that an organic monolayer, deposited on surface, can provide electrons to compensate the hole carriers of GaMnAs which restrain the ferromagnetism ($T_C < 170K$) [1]. The control over ferromagnetism by changing carrier concentration like Kreutz's research is what we want to achieve at room temperature.

Initially, spin injection attempts were limited to the heterostructure comprising a metallic ferromagnet on semiconductor device [2,3]. But due to serious deficiency of spin injection at metal-semiconductor interface, this idea was replaced by a quest for the ferromagnetism in semiconductor. The concept of ferromagnetic semiconductor was initiated by introducing dilute concentration of magnetic dopants (Mn^{2+}) into a semiconductor material, $Ga_{(1-x)}Mn_xAs$ ($x = 0.015-0.071$) [4]. The ferromagnetism observed in such non-magnetic semiconductors are supposed to be carrier mediated. The excess electrons provided by the dopants delocalize near the fermi level. For certain cases, these delocalized impurity bands become spin polarized and tend to show half-metallic behavior. The materials showed such property were started to be termed as "Dilute Magnetic Semiconductor (DMS)". In an ideal DMS, the charge carriers are spin polarized and behave like half-metallic which enable the charge carriers to be transported by inducing very small applied electrical or magnetic field. By showing high promises of carrier mediated spin-charge transport, DMS materials have raised a lot of enthusiasm in scientific community in the recent years to extend the established CMOS (Complementary Metal Oxide Semiconductor) based electronics towards spintronics devices.

1.2 Dilute Magnetic Semiconductors (DMS)

Dilute magnetic semiconductors are actually non – magnetic materials containing very small amounts of magnetic ions as dopants. Due to these magnetic dopants, the non – magnetic materials show dilute ferromagnetism. But the basic difference between DMS and other ferromagnetic materials is DMS's half metallic behavior which alone controls the spin-charge transport in these materials. Hence, it is noteworthy to revisit the concept of spin polarization and half metallic behavior before going further about DMS.

Spin polarization can be expressed as the ratio of the density of states of up-spin and down-spin electrons at fermi level. The degree of polarization is $P = \frac{N_{up} - N_{down}}{N_{up} + N_{down}}$ where up-spin (N_{up}) and down-spin (N_{down}) electrons denote the electrons polarized in opposite directions. In paramagnetic materials, the degree of polarization is 0 and in conventional ferromagnetic materials the value is between 0 and 1. Only

for the cases of half-metal, the degree of polarization is 1. The schematic density of states of an ideal half metal is given in Fig 1(g). In an ideal half-metal, for specific polarized electrons (either N_{up} or N_{down}) will have density of states in fermi level which does not have any gap between conduction and valence band. For other set of polarized electrons, there will be no density of states in fermi level just like an intrinsic semiconductor. This means that all electrons at fermi level in half-metal are completely polarized and for the presence of gapless density of states at fermi level, the polarized electrons will behave like free electrons of metal. For this reason, these materials are called as half-metal. The concept of half-metal was first predicted by Groot *et al.* during the electronic band structure calculation of NiMnSb and PtMnSb [5]. Coey *et al.* explained the half metallic behavior in CrO_2 and predicted that the half-metallicity in semiconductors can be classified in two types as showed in Fig 1 (h) & (i) [6].

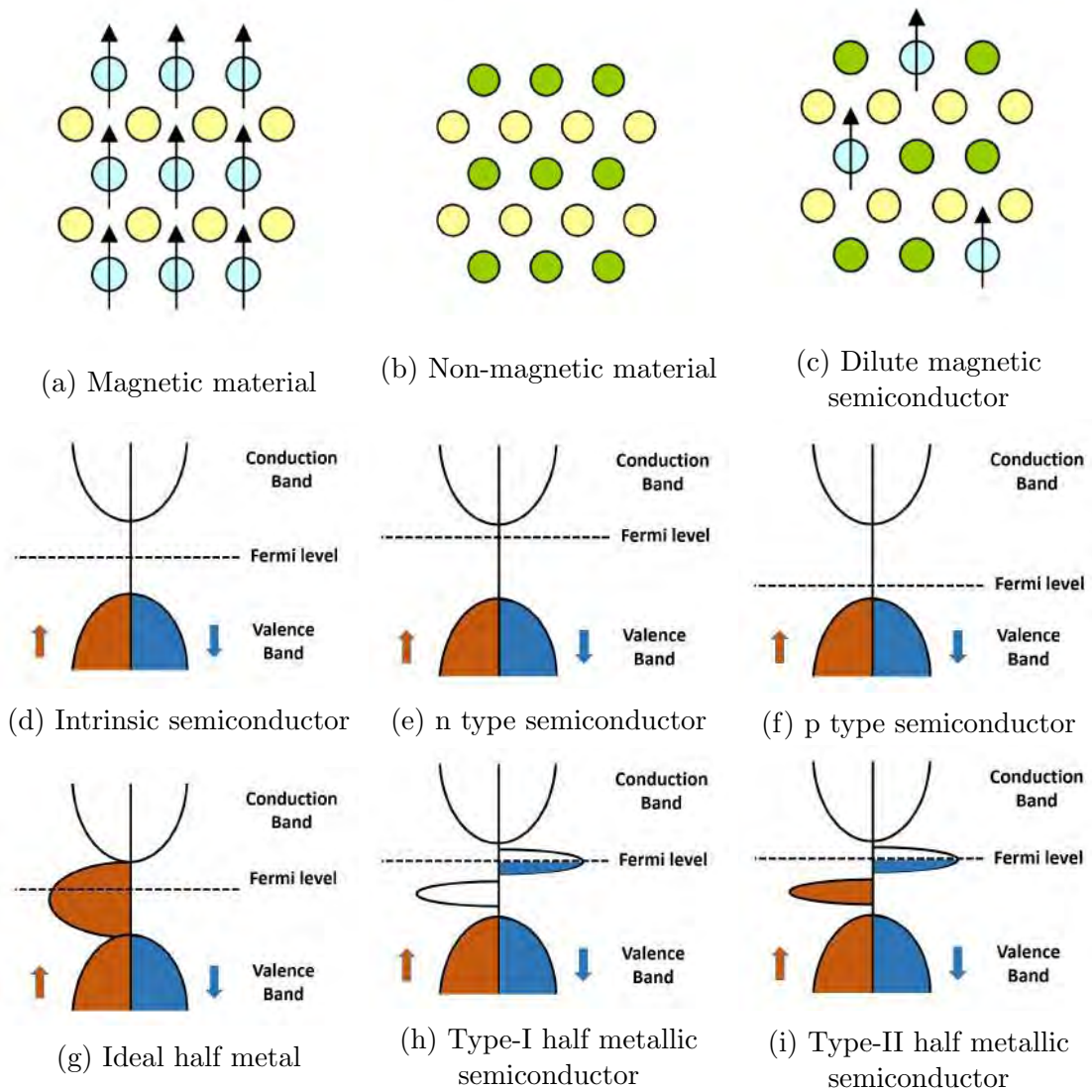


Figure 1.1: (a-c) Difference between ferromagnetic material, non-ferromagnetic material and dilute magnetic semiconductor. (d-i) Density of states of different types of semiconductor, ideal half metal and half-metallic semiconductors

The bands at fermi level are originated from the delocalized d or f orbital electrons in both types of half-metallic semiconductors. From Fig 1 (h) & (i), it can be clearly understood that the bands in type I material are comprised of less than half filled d or f orbital electrons while in type II, the bands are comprised of more than half-filled d or f orbital electrons. Although the density of states of half-metallic semiconductor deviate from the gapless states of half-metals, the spin polarized delocalized electrons can be transported by hopping from one site to another [6].

In dilute magnetic semiconductor, the magnetic dopants have excess electrons which delocalize at fermi level. It is noteworthy to mention that the dilute magnetic semiconductors should have non-zero spin polarization to achieve half-metallicity. If the half-metallic behavior can be made stable at room temperature, only then the DMS materials will be able to bring a paradigm shift in technology by integrated in logic devices, spin polarized light emitting diodes, non – volatile memory storages, spin field effect transistors etc.

1.3 Current challenges in DMS research

The earliest discovery of dilute magnetic semiconductors were reported for Mn doped II-IV and III-V alloys. In 1988, Furdyna *et al.* studied the physical properties of $Cd_{(1-x)}Mn_xSe$ and $Hg_{(1-x)}Mn_xTe$ but the curie temperature was around 40 K [7]. In 1989, Munekata *et al.* observed the properties of dilute magnetic semiconductor in $Ga_{(1-x)}Mn_xAs$ while the curie temperature was around 100 K [8]. Since then half metallic behavior in these materials specially in $Ga_{(1-x)}Mn_xAs$ was deliberately studied but the curie temperature could not be raised above 170 K. The quest for a room temperature DMS got a new dimension when Matsumoto *et al.* reported extrinsic ferromagnetism in $Ti_{(1-x)}Co_xO_2$ which has very high curie temperature (600 K) [9]. To this day, dilute ferromagnetism at room temperature has been observed in non-magnetic oxides like ZnO, In_2O_3 , CeO_2 , SnO_2 , CuO_2 etc [10–13]. But the concept of making DMS by doping of magnetic impurities was changed when room temperature ferromagnetism was observed in undoped non-magnetic oxides. Besides, magnetic clusters and secondary phases have been found to contribute to extrinsic ferromagnetism in these oxides [14–16]. Therefore, creation of any spintronics device based on these oxide based DMS materials remains halted due to the true understanding of the origin of ferromagnetism in these materials.

1.4 Objective of this research

The aim of this research is focused on the dilute ferromagnetism in $Ti_{(1-x)}Sm_xO_2$ ($0 \leq x \leq 0.2$) nanoparticles. Among the wide bandgap semiconductors, TiO_2 is the most extensively studied material for its superior chemical stability and high curie temperature. The primary reason for Sm^{3+} substitution in TiO_2 is to create oxygen vacancy. The electronic configuration of Sm and Ti are $[Xe] 4f^6 6s^2$ and $[Ar] 3d^2 4s^2$ respectively. But the preference of Sm^{3+} ($Sm^{3+}=[Xe] 4f^5$) substitution stems from the fact that it has odd number of excess electrons when it substitutes Ti^{4+} in TiO_2 . The number of excess electrons is important because they are supposed to be delocalized and induced non-zero spin polarization at fermi level. The delocalized electrons tend to pair themselves by crystal field splitting for energy minimization.

For example, Fe^{2+} ($[Ar] 3d^6$) has four unpaired d orbital electrons but after crystal field splitting Fe^{2+} tends to have 3 pairs of d electrons which in turns yield near to zero spin polarization. On another case, Fe^{3+} ($[Ar] 3d^5$) five unpaired electrons in valence band. Because having odd number of electrons, it is impossible to nullify the net spin polarization of Fe^{3+} by electron's ownelves pairing mechanism. However, in this research Sm^{3+} was chosen for its odd numbers of f orbital electrons in valence band which are supposed to exhibit strong spin-orbit interaction.

Another reason of Sm^{3+} substitution in TiO_2 is its larger ionic radius ($Sm^{3+}=1.08 \text{ \AA}$ and $Ti^{4+}=0.68 \text{ \AA}$). One of the main goals of this research is to investigate what happens beyond the solid solubility limit of Sm^{3+} substitution. As it is previously stated that there are discrepancies on the origin of ferromagnetism in oxide DMS materials which mostly revolve around the nature of substitution. Hence it is crucial to investigate the structural purity beyond solid solubility limit of substitution such as the formation & growth of the interface of any 2nd phase and their effect on optical and magnetic properties. So, the aim of this research can be summarized as:

- To study the effect of Sm^{3+} substitution on the structural, optical and magnetic properties of TiO_2
- To investigate the nature of formation and growth of any second phase beyond solid solubility limit of substitution

1.5 Thesis overview

Chapter 2 starts with a brief review on recent progress in dilute magnetic semiconductors and the experimental techniques to investigate the spin polarization in these materials. It will also discuss several theoretical models on the origin of ferromagnetism in DMS. Finally there will be a brief review on recent theoretical and experimental research on TiO_2 . Chapter 3 describes the experimental methodology and introduces the detailed synthesis process followed by the structural, morphology, optical and magnetic characterization techniques. Chapter 4 discusses the results obtained from experiments and how they support an elucidation of this research which is concisely given in Chapter 5.

CHAPTER 2

LITERATURE REVIEW

The requirement of dilute magnetic semiconductor is its non-volatile ferromagnetism which must have non-zero spin polarization at fermi level. To this day, extensive research have been performed on dilute magnetic semiconductors. During exploitation the prospects of DMS in any material a number of questions must be carefully resolved. The primary questions are definitely about the structural purity of the sample such as any presence of 2nd phase in X-ray and electron diffraction study, any presence of metallic cluster of dopants in X-ray photoelectron study, any presence of satellite peaks due to oxygen vacancies in the valence band spectra etc. If these questions are resolved then next questions will come forward which are about the spin polarization nature. Before going further on the spin polarization in DMS, it is required to revisit the concepts of three fascinating photoemission spectroscopy techniques which are X-ray absorption spectroscopy (XAS), X-ray magnetic circular dichroism (XMCD) and angle resolved X-ray photoelectron spectroscopy (ARPES). This chapter begins with a plain explanation of these powerful spectroscopy techniques.

2.1 X-ray Absorption Spectroscopy

X-ray absorption spectroscopy provides a clear picture of valence shell by exciting a core level electron to an empty valence shell. In magnetic materials, the valence shell is typically 3d or 4f and they are partially filled. The excited photoelectrons take position in the empty places in d or f orbitals and eventually return to ground state by emitting a fluorescent/ Auger electrons. The detector in XAS capture and analyze the Auger electrons. Peaks are splitted due to spin-orbit interaction of core level electrons.

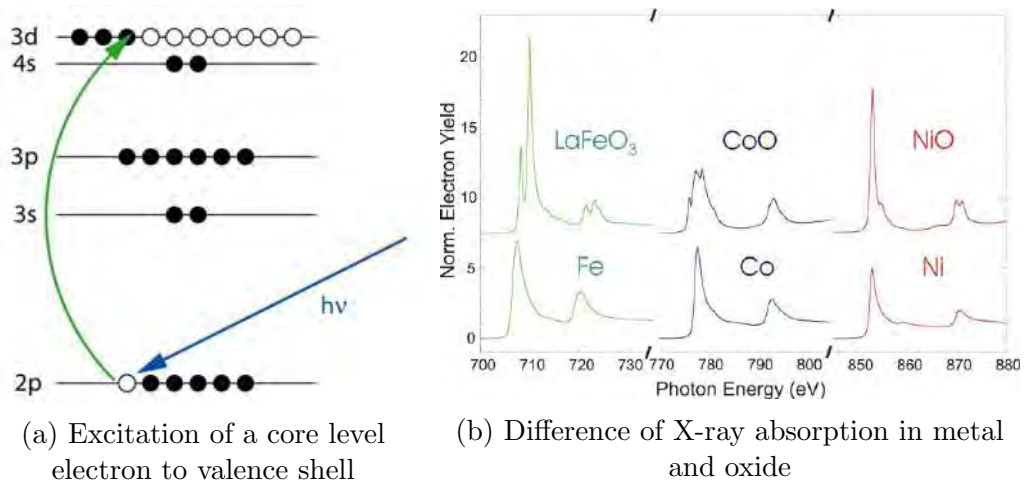


Figure 2.1: Schematic principle of X-ray absorption spectroscopy. (images are taken from the webpage of SLAC, Stanford University)

Usually metal shows 2 peaks in XAS while oxides show multiplets as spin-orbit interactions are more localized in oxide materials. Total intensity of the peaks is proportional to the empty d or f orbital density of states. Although XAS can depict the density of states in valence band but it cannot provide any details of spin polarization. For example, the electron configuration of Fe is $[\text{Ar}] 3d^6 4s^2$ and for Fe^{3+} it is $[\text{Ar}] 3d^5$.

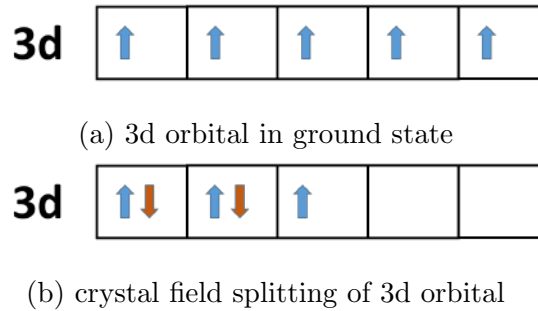


Figure 2.2: Difference in 3d orbital due to crystal field splitting in Fe^{3+}

In XAS, the photo-excited core level electrons just fill up the empty states in 3d orbital and there will be no difference in the observed absorption spectra for crystal field splitting. During investigation of spin polarization, observation of only density of states is not enough. For example, XAS cannot differentiate between the density of states for 5 spin-up electrons showed in Fig 2.2(a) and the density of states for 3 spin-up & 2 spin-down electrons showed in Fig 2.2(b). This problem has been resolved by X-ray magnetic circular dichroism spectroscopy.

2.2 X-ray Magnetic Circular Dichroism

X-ray magnetic circular dichroism (XMCD) is a special feature of X-ray absorption spectroscopy (XAS). Dichroism means polarization dependent light absorption of any materials. In simple terms, XMCD is basically an XAS placed in a magnetic field where the incident light is polarized. The left or right circularly polarized photons transfer their angular momentum to the core level electrons. Since change of spin momentum is forbidden in electric dipole transition, the photo-ejected electrons carry the same angular momentum to the valence band. The theory of XMCD was first proposed by Erskine *et al.* in 1986 and the experimental proof of XMCD was demonstrated by Gerrit van der Laan *et al.* in 1986 [17, 18]. A list of synchrotron facilities for XMCD around the world is given in the reference [19].

Fig 2.3 shows a schematic mechanism of XMCD. At ground state, 2p electrons of Cobalt metal are usually splitted in $j = \frac{3}{2}$ level (L_3 edge) and $j = \frac{1}{2}$ level (L_2 edge). It is noteworthy to mention that spin and orbit are coupled parallel in L_3 edge and antiparallel in L_2 edge. At first, the right circularly polarized incident light excites the 2p electrons which are parallel to the helicity of the light (spin-up electrons). Similarly the left circularly polarized light excites the antiparallel electrons at 2p core states (spin-down electrons). These electrons carry the angular momentum and fill up the unoccupied empty states in 3d orbital. The net difference of available places for spin-up and spin-down electrons in unoccupied 3d orbitals can be understood by the XMCD graph.

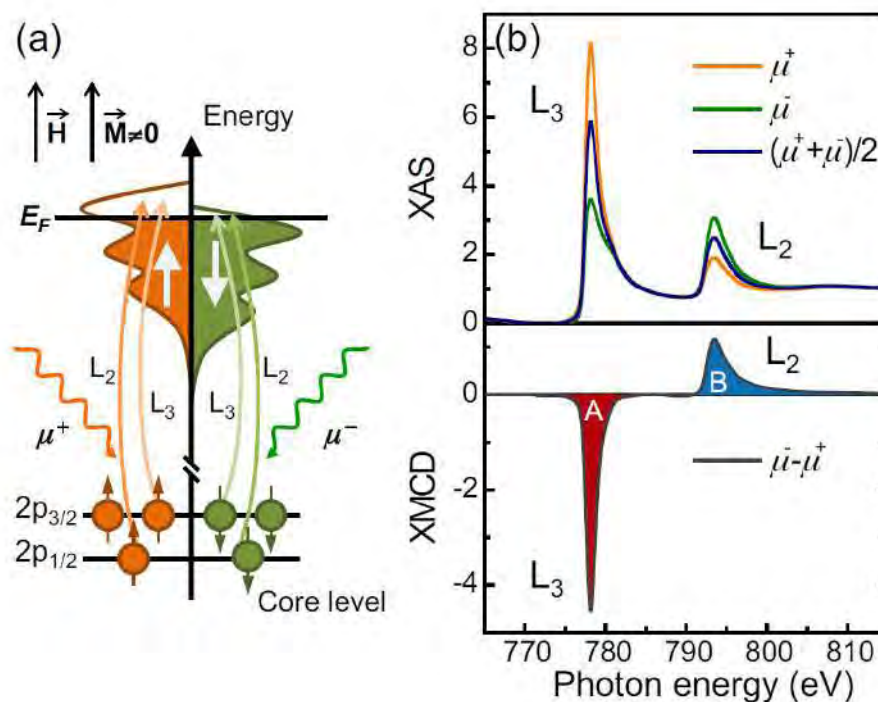


Figure 2.3: (a) Schematic principle of X-ray magnetic circular dichroism (XMCD)
 (b) Difference between XAS and XMCD principle [20]

2.3 Angle Resolved Photoemission Spectroscopy

Angle resolved photo emission spectroscopy is the characterization technique for direct observation of the electronic band structure of any crystalline material.

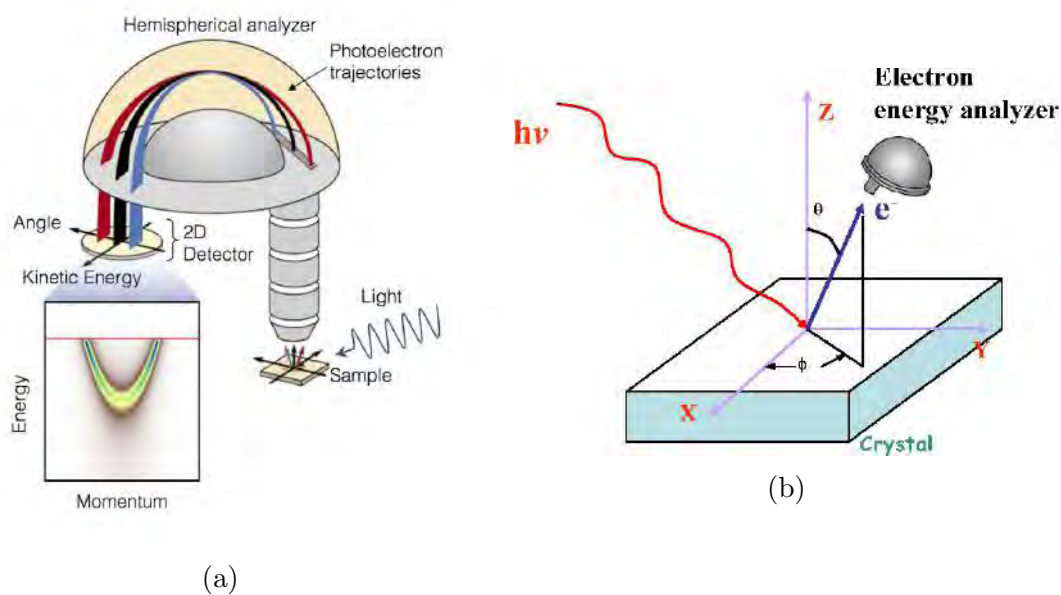


Figure 2.4: Schematic diagram of angle resolved photoemission spectroscopy

Like the other photoemission spectroscopy, ARPES is based on the photoelectric effect which was pioneered by Einstein. When a sample is irradiated by incident

light with sufficient energy, an electron from the surface of the material can absorb the energy of photon and escape the surface. The kinetic energy required for this process is $h\nu - \phi$ ($h\nu$ is the photon energy and ϕ is the work function of the material). ARPES measures the kinetic energy of a photoelectron and calculates its original binding energy using the energy conservation law. Electrons having different momentum will escape from the surface at different angles and hence the momentum resolution of the photojected electrons can be determined by analyzing the angle of the photoemission.

2.4 Recent advances in DMS research

This section will briefly present a review on recent progress in DMS research. Over last few decades extensive research were performed on DMS properties in III-V, II-VI and oxide materials. The seminal research work by Munekata *et al.* first demonstrated the DMS properties in III-V materials [8]. In their work, they have grown $In_{(1-x)}Mn_xAs$ ($x \leq 0.18$) on both InAs and GaAs substrates by molecular beam epitaxy. The films showed intrinsic semiconducting behavior (n-type) but the curie temperature was far below room temperature. Hayashi *et al.* found extraordinary magnetoresistance in $Ga_{(1-x)}Mn_xAs$ [21]. The curie temperature and magnetization were increased with Mn concentration. Matsukura *et al.* explained that the ferromagnetism observed in $Ga_{(1-x)}Mn_xAs$ follows Ruderman-Kittel-Kasuya-Yosida (RKKY) exchange interaction [4].

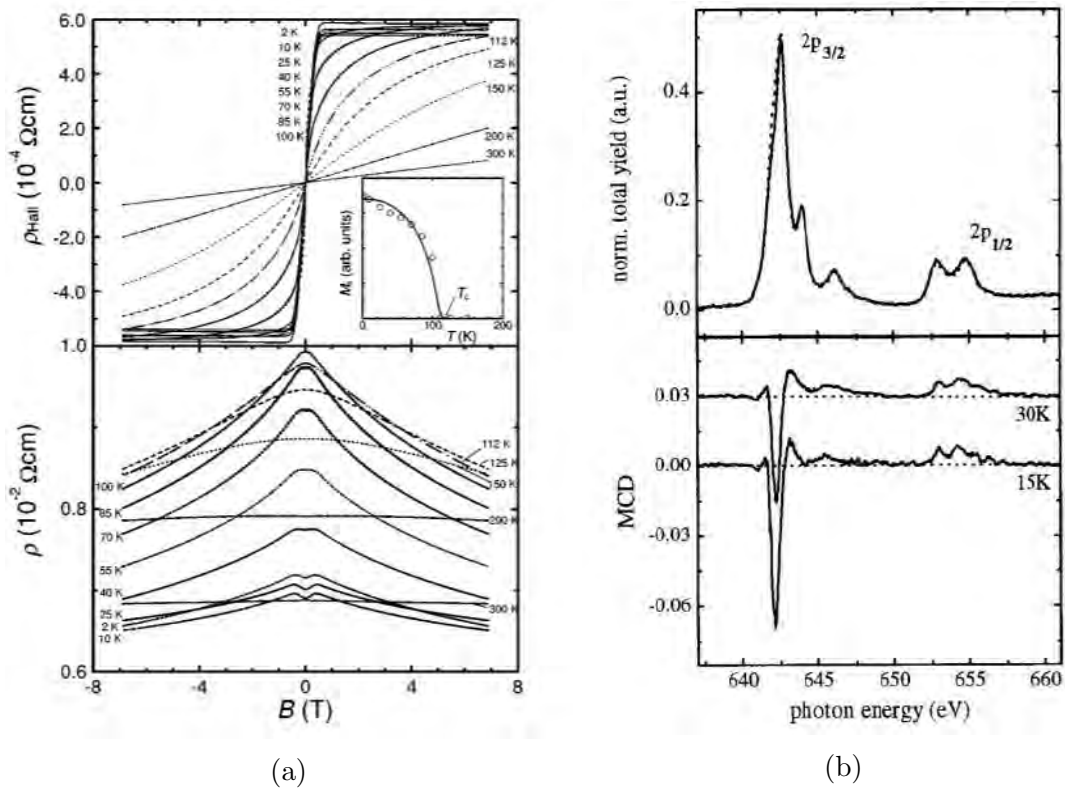


Figure 2.5: (a) Magnetic-field vs. Hall resistivity ρ_{Hall} and resistivity ρ of $Ga_{(1-x)}Mn_xAs$ vs. temperature. Mn concentration is $x=0.053$. The change of spontaneous magnetization M_s with temperature is showed in inset [4] (b) X-ray absorption and X-ray magnetic circular dichroism spectra of $Ga_{0.98}Mn_{0.02}As$ [22]

Khalid *et al.* found strong spin polarization at fermi level in $In_{0.95}Mn_{0.05}P$ sample which showed intrinsic semiconducting behavior and negative magnetoresistance [23]. Scarpulla *et al.* reported carrier mediated ferromagnetism in $Ga_{0.94}Mn_{0.06}P$ where strongly localized hole states are created just above the valence band due to Mn doping [24]. But for both $Ga_{(1-x)}Mn_xP$ and $In_{(1-x)}Mn_xP$ the curie temperature remains around 60 K.

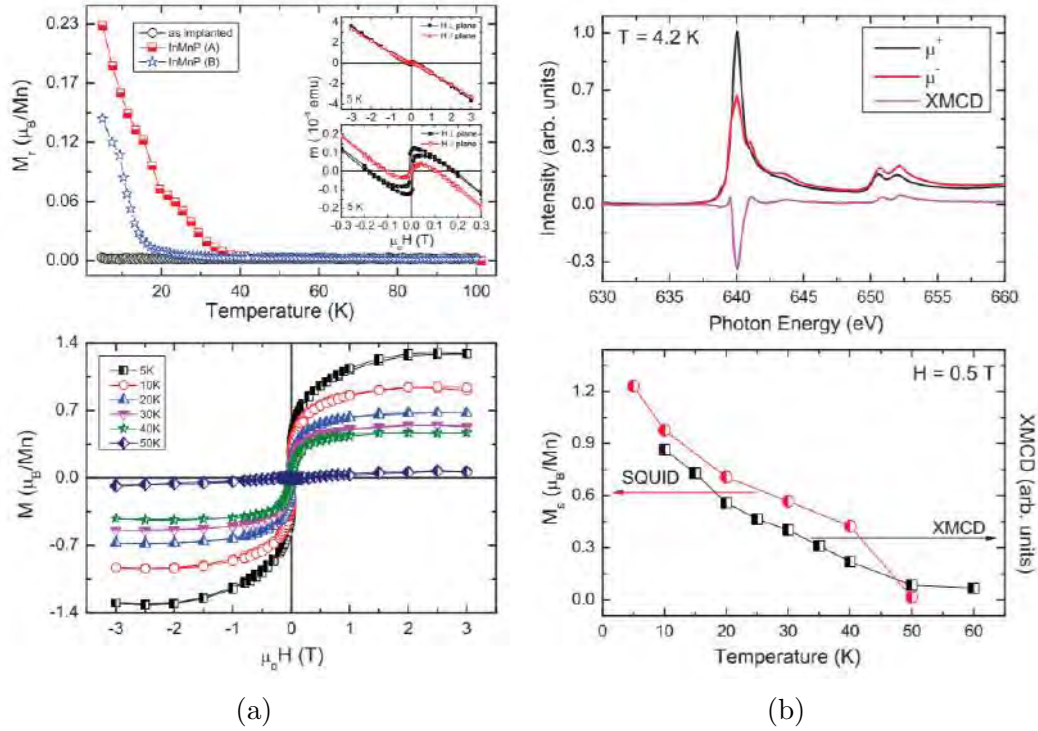


Figure 2.6: (a) Magnetization vs. temperature of as-implanted and laser annealed (A and B) $In_{0.95}Mn_{0.05}P$ samples (b) XAS and XMCD study of $In_{0.95}Mn_{0.05}P$ [23]

Gray *et al.* experimentally proved the half-metallic behavior of $Ga_{0.97}Mn_{0.03}As$ by analyzing the electronic band structure using Hard X-ray angle resolved photoemission spectroscopy [25]. The Mn induced density of states were observed between fermi level and valence band maxima in their experiment.

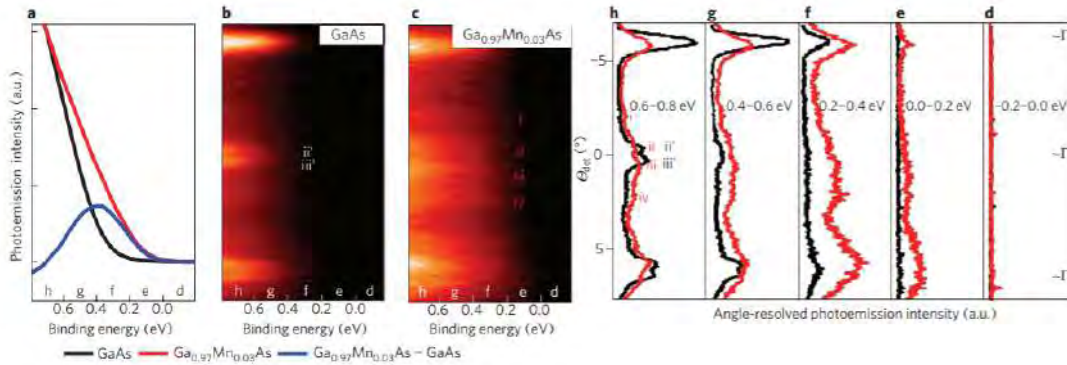


Figure 2.7: Experimental observation of half-metallic behavior in $Ga_{0.97}Mn_{0.03}As$ by Hard X-ray angle resolved photoemission spectroscopy [25]

Kobayashi *et al.* also reported half-metallic behavior of $Ga_{0.975}Mn_{0.025}As$ in

their seminal research paper [26]. Nemvsak *et al.* also reported half-metallic behavior in $Ga_{0.95}Mn_{0.05}As$ by using standing wave angle resolve photoemission spectroscopy (SW-ARPES) [27]. Keqi *et al.* investigated the electronic structure of $Ga_{0.98}Mn_{0.02}P$ by using hard X-ray angle resolved photoemission spectroscopy and observed Mn induced impurity states near valence band maxima [28].

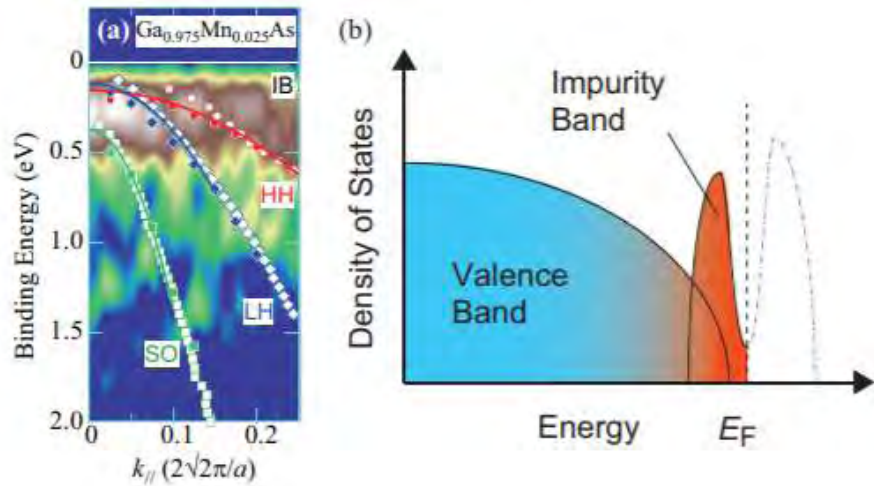


Figure 2.8: Experimental observation of half-metallic behavior in $Ga_{0.975}Mn_{0.025}As$ by soft X-ray angle resolved photoemission spectroscopy [26]

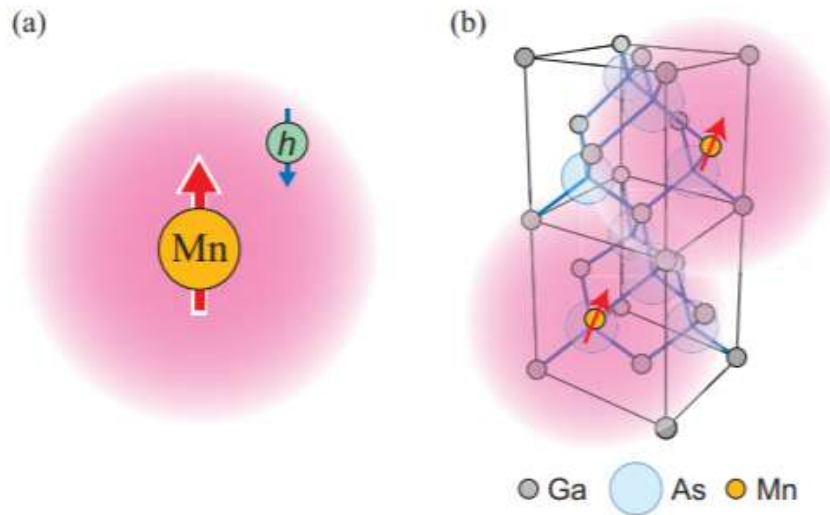


Figure 2.9: (a) Bound magnetic polaron controlling the ferromagnetism in $Ga_{0.975}Mn_{0.025}As$. (b) Schematic image of magnetic interaction in $Ga_{0.975}Mn_{0.025}As$ crystal structure [26]

Furdyna *et al.* first reported II-VI based dilute magnetic semiconductors ($Cd_{(1-x)}Mn_xSe$ and $Hg_{(1-x)}Mn_xTe$) in 1988 [7]. Zhao *et al.* reported short-range magnetic ordering in $Zn_{(1-x)}Cr_xTe$ [29]. Observation of similar short-range ferromagnetic interaction in II-VI based DMS have been reported in many literatures in last few decades [30–32].

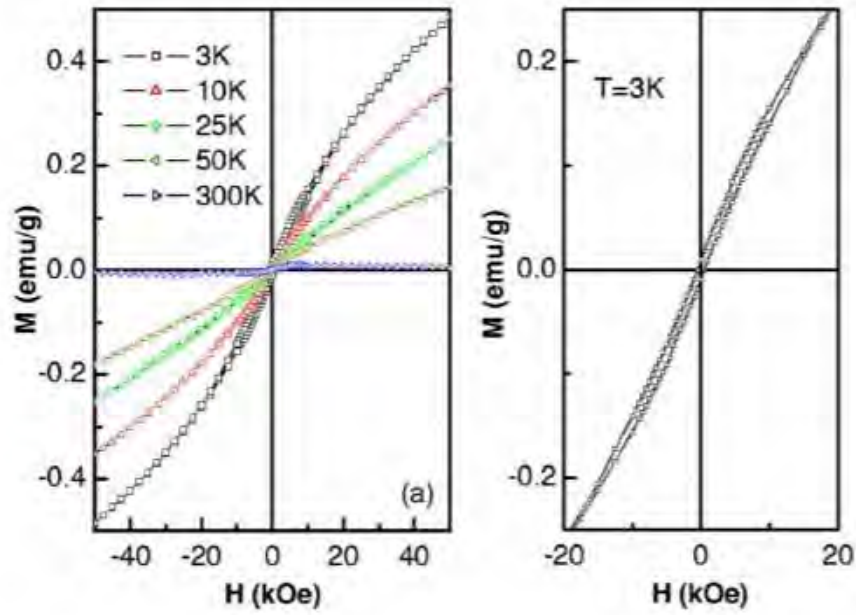


Figure 2.10: Magnetization vs. applied field in $Zn_{(1-x)}Cr_xTe$ [29]

Matsumoto *et al.* first demonstrated the intrinsic ferromagnetism in $Co:TiO_2$ which showed high curie temperature [9]. This groundbreaking discovery led to extensive research on DMS in oxide based materials since 2001 [33–37]. Yamada *et al.* reported electrically induced ferromagnetism in $Ti_{0.90}Co_{0.10}O_2$ at room temperature [38]. Saadaoui *et al.* reported intrinsic ferromagnetism observed in $Ti_{0.95}Co_{0.05}O_2$ thin film is controlled by oxygen vacancy [39]. Several seminal research works also exhibit intrinsic carrier mediated ferromagnetism in other non-magnetic oxides like ZnO , In_2O_3 , CeO_2 [10, 40–46].

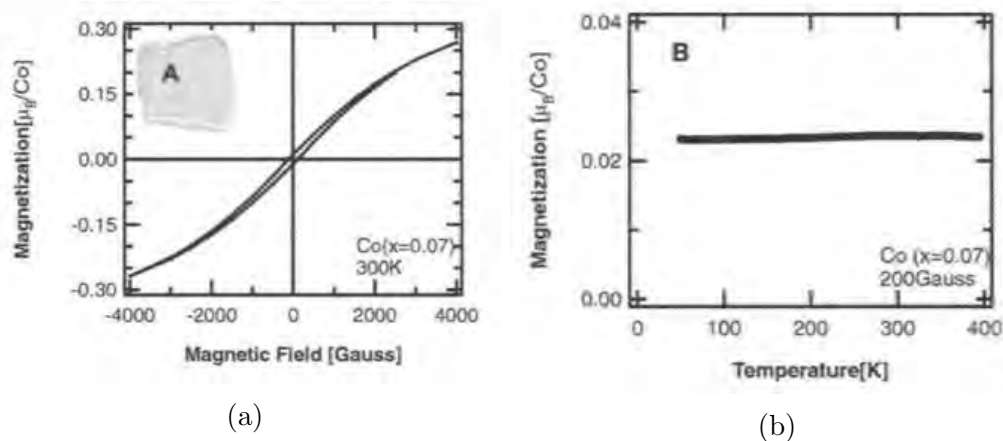
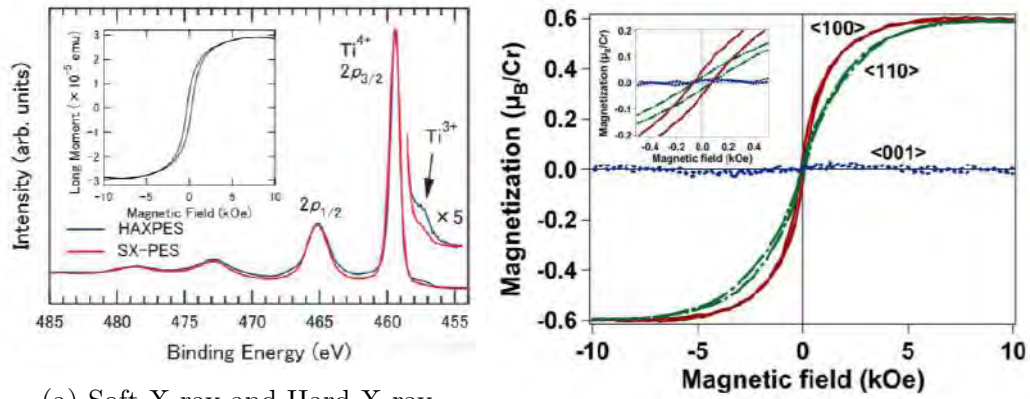


Figure 2.11: (a) Magnetization vs. applied field (b) Magnetization vs. temperature graph of $Ti_{0.93}Co_{0.07}O_2$ sample [9]



(a) Soft X-ray and Hard X-ray photoemission spectroscopy of $Ti_{0.95}Co_{0.05}O_2$ thin film [47]

(b) Magnetization vs. applied field in $Ti_{0.91}Co_{0.09}O_2$ thin film [48]

Figure 2.12: Intrinsic ferromagnetism in transition metal doped TiO_2 thin films

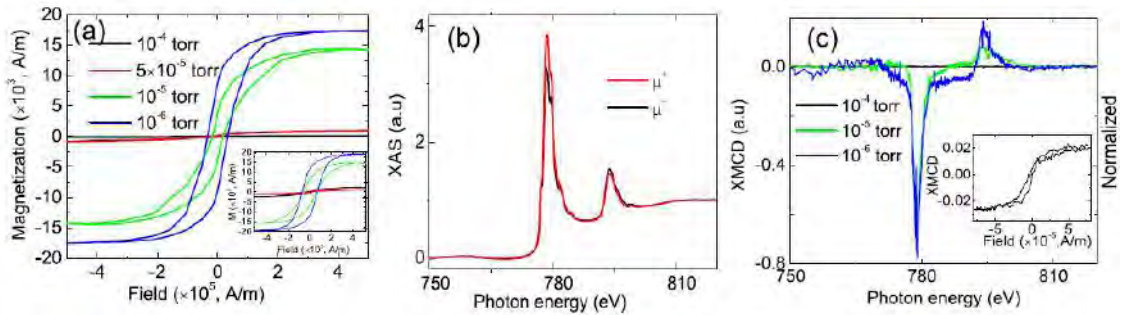


Figure 2.13: (a) Magnetization vs. applied field (b) XAS and (c) XMCD spectra of $Ti_{0.95}Co_{0.05}O_2$ thin film [39]

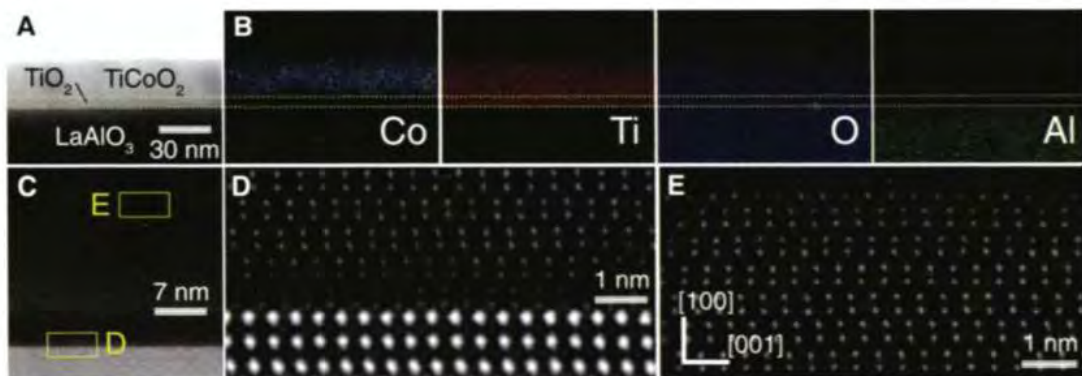


Figure 2.14: Bright field STEM image of $Ti_{0.90}Co_{0.10}O_2$ grown on $LaAlO_3$ substrate. The HAADF and EDX images show the homogeneous doping of Cobalt in TiO_2 [38]

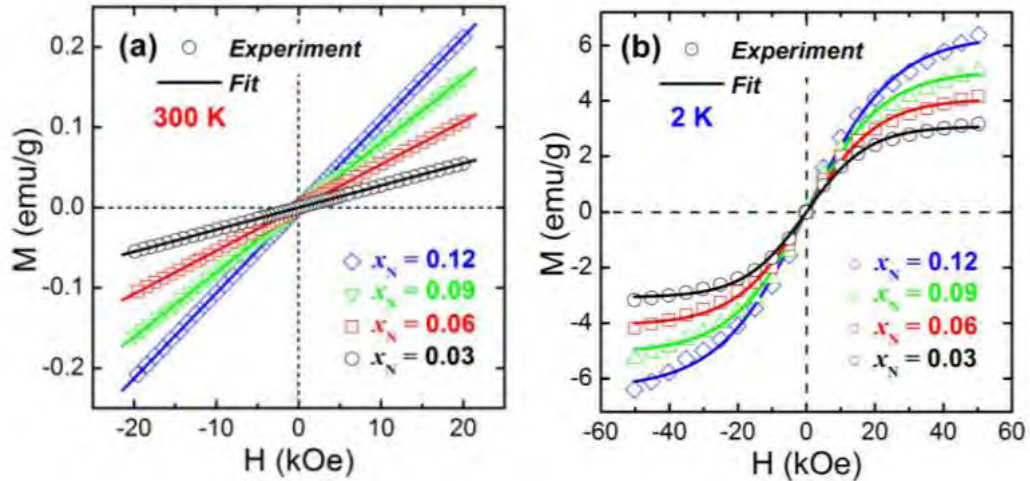


Figure 2.15: Magnetization vs. applied field in $Ti_{(1-x)}Co_xO_2$ nanoparticles [49]

2.5 Origin of ferromagnetism in DMS

Despite extensive research have been performed on DMS over last few decades, the true origin of ferromagnetism remains still unclear. The principle concept of DMS is to induce ferromagnetism by adding magnetic dopants in a non-magnetic semiconductor material. But Sunderasan *et al.* showed that ferromagnetism might be found in non-magnetic materials if their particle size is in nanoscale range [14]. In their research, they found that variation of annealing temperature of undoped non-magnetic oxides like ZnO , In_2O_3 , CeO_2 and Al_2O_3 is related to observed dilute ferromagnetism. In explanation they attributed this phenomena to be controlled by the concentration of oxygen vacancies on surface of the nanoparticles. According to Sunderasan *et al.* the surface oxygen vacancies create localized electron spin moments which follow Ruderman-Kittel-Kasuya-Yosida (RKKY) interaction. The RKKY interaction is basically a long range exchange interaction between d or f orbital electrons and it decays in an algebraic manner with respect to the distance between spins. The theory of RKKY type exchange interaction was inspired from mean field Zener model which pioneered the theoretical proof of DMS properties in Mn doped II-VI and III-V semiconductors.

Zener model suggests that delocalized charge carriers enhances the ferromagnetic interaction of localized spins in metallic system. But the exchange interaction in DMS is different than the short range d-d exchange interaction in 3d metal. Applying the mean field theory to the Zener model, it's found that the ferromagnetism in DMS can be well described by the long range p-d exchange interaction between localized and delocalized spins. According to this theory, doped holes redistribute themselves by maintaining favorable delocalization length so that the energy of the system becomes less. The mean field Zener model established an exchange constant (J_{p-d}) which can be experimentally determined. This model not only predicted a number of DMS candidates including zinc blende and wurzite type wide band gap oxides and nitrides but also presented a mechanism to increase curie temperature in those materials. According to the suggestion, cure temperature can be raised by enhancing the hybridization energy which is proportional to a^{-3} (a is the lattice constant).

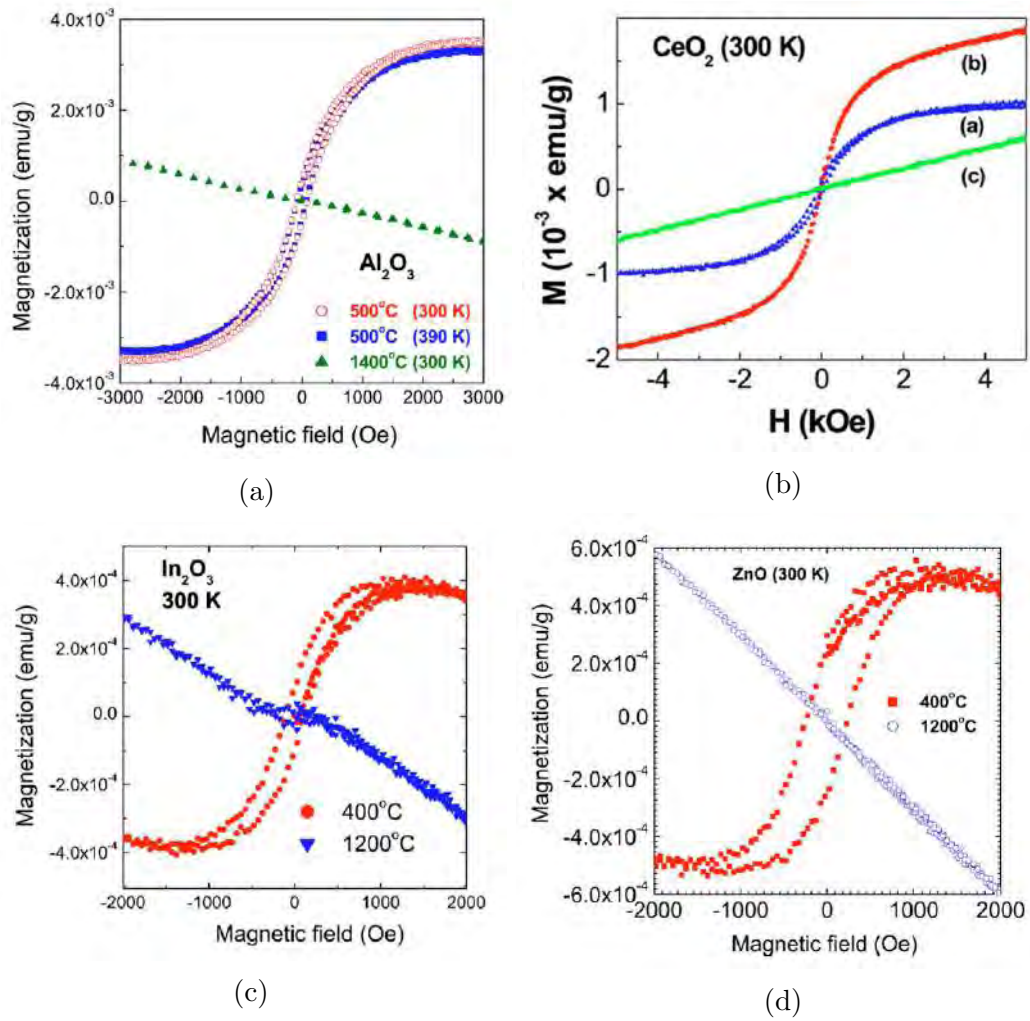


Figure 2.16: Dilute ferromagnetism observed in undoped non-magnetic oxides due to oxygen vacancies [14]

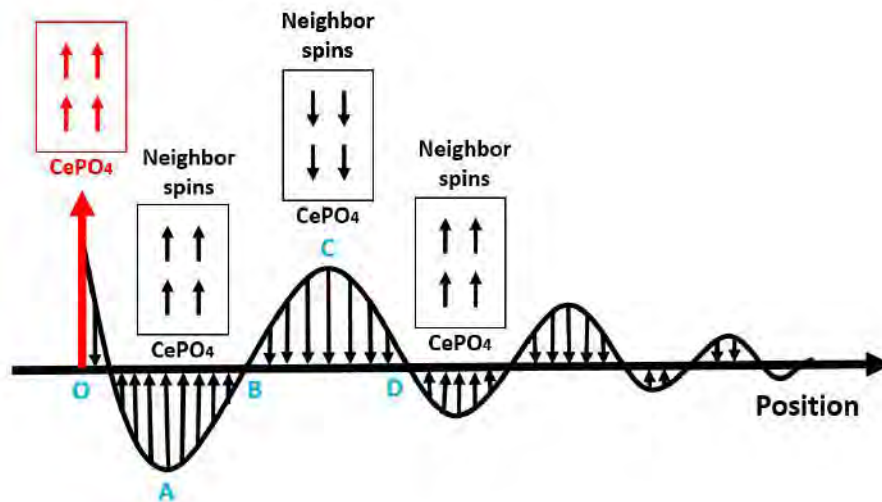


Figure 2.17: RKKY type exchange interaction of frustrated spins in CePO_4 [50]

The mean field Zener model predicted p-type DMS candidates where the hole

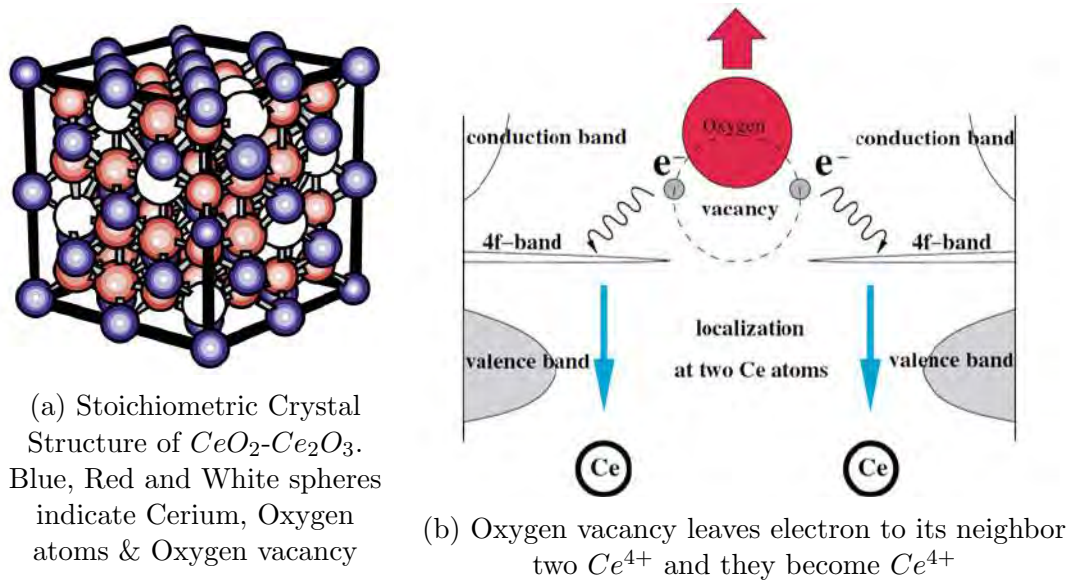
induced bands will be just above the valence band. This theory was proved wrong when it was found that the predicted DMS candidates showed n-type semiconducting behavior. Actually Zener model considered d orbital electrons will not participate in charge transport and it was based on Mn induced band states. The case is different for other transition metal ions as Mn has a unique orbital levels which is not like the other transition metal ions. However, RKKY interaction resolved the issue which focused on charge carrier mediated interaction in the DMS. The concept of mean field Zener model and RKKY is almost same. RKKY explains the ferromagnetic-antiferromagnetic interaction when the concentration of holes is larger than that of spins which cannot be explained by Zener model.

In contrast to direct and indirect exchange interaction described by mean field Zener model and RKKY model, there are also some additional exchange interaction which have been found non-trivial to explain the ferromagnetism in DMS. Among them the concept of bound magnetic polaron is most relevant. When the delocalized spins act as a cluster and their behavior is controlled by the effective mass of the cluster. The polaronic interaction increases with decrease in temperature. The interaction between the localized polaron is antiferromagnetic. This model has become popular to explain the ferromagnetism observed in a low carrier density DMS. It is noteworthy to mention that none of these theories can alone truly describe the universal nature of the ferromagnetism in DMS.

2.6 Role of oxygen vacancy in oxide based DMS

Oxide based DMS have showed high promises for room temperature intrinsic ferromagnetic behavior but the fundamental limitation is the true understanding of ferromagnetism in these materials. Oxygen vacancies play crucial role in determination of ferromagnetic interaction which have extensively studied by both computational and experimental approaches. In previous section, the research of Sunderasan *et al.* clearly demonstrated the influence of oxygen vacancies on the observed ferromagnetism in undoped non-magnetic oxides. Oxygen vacancy induced band states strongly interact with delocalized electrons and are capable of nullifying the non-zero spin polarization at fermi level. Hence the role of oxygen vacancy has been deliberately studied since the discovery of intrinsic ferromagnetism in $Co : TiO_2$.

Bryan *et al.* showed that the oxygen vacancies at grain boundaries are responsible for the high curie temperature ferromagnetism in Cr and Co doped TiO_2 nanomaterials [51]. Chowdhury *et al.* reported that Mn doping distorts the TiO_2 crystal structure generating oxygen vacancies at surface which reduce the mobility of charge carriers. They attributed the ferromagnetic interaction to be controlled by oxygen vacancies via forming bound magnetic polarons in the system [52]. Such kind of surface oxygen vacancy induced ferromagnetism has been reported for TiO_2 , SnO_2 , TiO_2 and ZnO in many literatures [53–58].

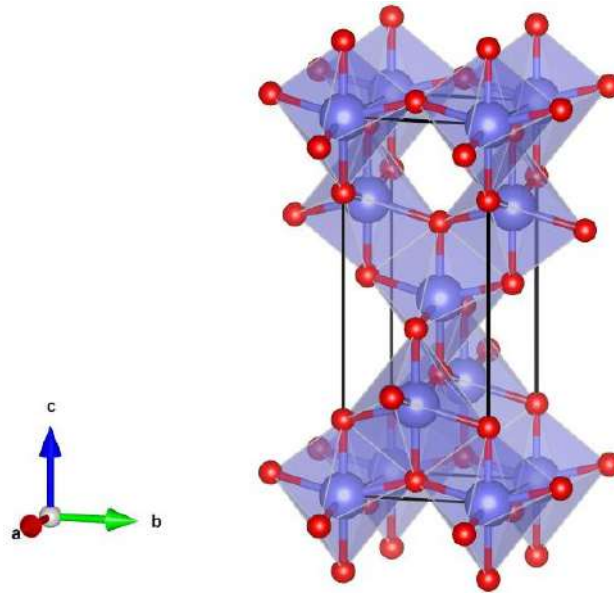
Figure 2.18: Role of oxygen vacancies in CeO_2 [59]

2.7 Prospects of TiO_2 as DMS

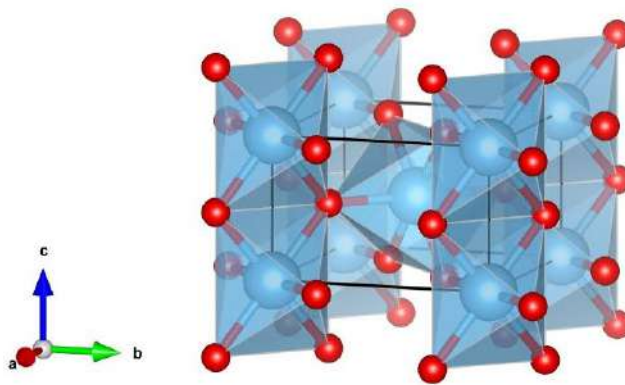
The groundbreaking discovery of $Co:TiO_2$ pioneered the quest for a DMS showing intrinsic semiconducting behavior at room temperature. Although, the prospects of DMS have been reported for other non-magnetic oxides like ZnO , In_2O_3 and CeO_2 , the superior stability of TiO_2 makes itself a unique candidate for DMS. For example, CeO_2 has almost the similar lattice matching with Si but due to the instability the DMS prospects in CeO_2 are considered much volatile than the others. The exceptional capability of charge transfer between Ce^{3+} and Ce^{4+} enables CeO_2 as an outstanding material for oxygen storage and catalyst like applications. But this instability is a serious concern when it comes to any device application. From this perspective, TiO_2 outruns the other oxide DMS candidates.

TiO_2 has three stable polymorphs - anatase, rutile and brookite. Among them rutile is the most stable one in bulk and anatase is most stable in nanoscale range due to less surface energy [60]. Both anatase and rutile have tetragonal crystal structure while the titanium atom is surrounded by six oxygen atoms in an octahedral arrangement. During heat treatment, anatase undergoes a phase transition in the temperature range 600-700 °C. Although, the bandgap of anatase (3.2 eV) is larger than rutile (3 eV), photoactivity of anatase is greater than the rutile due to anatase's electronic structure and surface morphology.

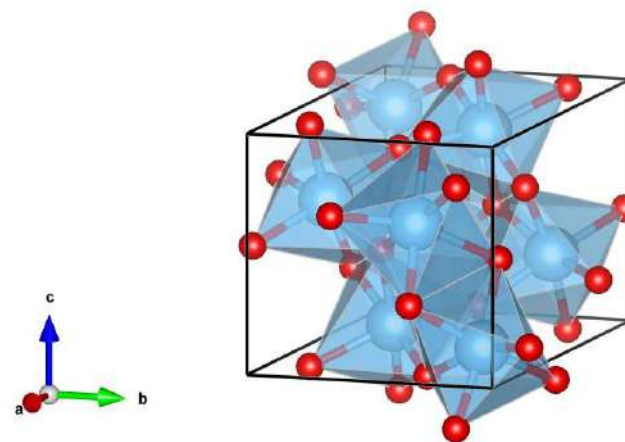
Transition and rare earth metal doped TiO_2 thin films and nanoparticles have been widely studied. Among them few literatures studied Sm doped TiO_2 nanoparticles and thin films. Xiao *et al.* synthesized $Ti_{(1-x)}Sm_xO_2$ ($0 \leq x \leq 0.015$) via sol-gel autocombustion technique. In their research they investigated the photocatalytic properties of rutile-anatase heterostructure and did not carry out the magnetic characterization [61].



(a) Anatase ($a = b = 3.78\text{\AA}$, $c = 9.51\text{\AA}$)



(b) Rutile ($a = b = 4.59\text{\AA}$, $c = 2.95\text{\AA}$)



(c) Brookite ($a = 5.45\text{\AA}$, $b = 9.18\text{\AA}$, $c = 5.14\text{\AA}$)

Figure 2.19: Crystal Structure of three polymorphs of TiO_2 ($\alpha = \beta = \gamma = 90^\circ$ for all polymorphs)

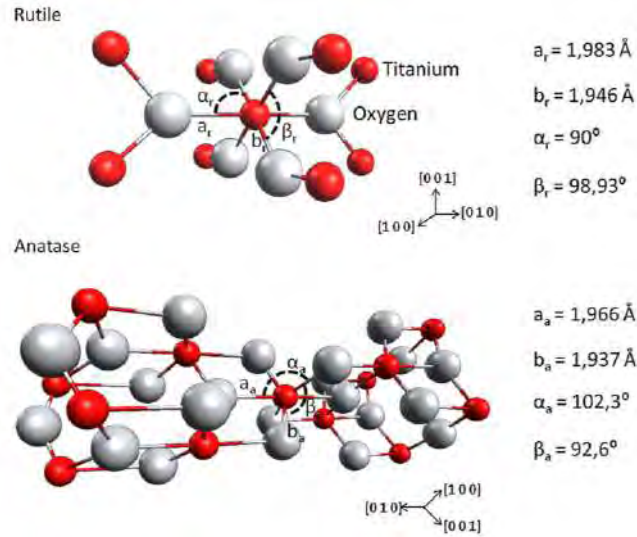


Figure 2.20: Difference in bond length and bond angles in rutile and anatase TiO_2

Cao *et al.* synthesized $Ti_{(1-x)}Sm_xO_2$ ($0 \leq x \leq 0.08$) via sol-gel technique [62]. Above $550^\circ C$ anatase to rutile phase transition started which became complete above $750^\circ C$. The authors have investigated the absorption spectra but they also did not characterize the magnetic property of the samples. Shi *et al.* also investigated the photocatalytic properties of $Ti_{0.99}Sm_{0.01}O_2$ nanoparticles and observed that Sm doping suppressed the particle size. The reduction in particle size was attributed to be beneficial in photocatalytic properties of the nanoparticles [63]. Hu *et al.* studied luminescence properties of Sm: TiO_2 nanoparticles and reported highest luminescence for 0.75 mol% Sm: TiO_2 nanoparticles [64]. Promising photoluminescence and photocatalytic properties of Sm: TiO_2 were also reported in some other literatures [65–69]. None of the above mentioned research work investigated the ferromagnetic behavior of the synthesized samples. Tseng *et al.* synthesized rutile $Ti_{(1-x)}Sm_xO_2$ ($0 \leq x \leq 0.02$) by molten salt method and observed that dilute ferromagnetism of Sm doped TiO_2 became weaker than the ferromagnetism of undoped TiO_2 nanoparticles [70]. However, no detailed study on Sm: TiO_2 has been reported so far to the best knowledge of the author of this thesis.

CHAPTER 3

EXPERIMENTAL METHODOLOGY

In this chapter, experimental methods employed in the thesis are described chronologically. First, materials synthesis is presented with details which has been performed repeatedly in order to ensure the reproducibility of the methodology. The structural characterization by X – Ray Diffraction (XRD), X – Ray Photoemission Spectroscopy (XPS), Differential Scanning Calorimetry (DSC) and Thermogravimetry (TG) analysis are described followed by Field Emission Scanning Electron Microscopy (FESEM) and Transmission Electron Microscopy (TEM) analysis. The optical properties were investigated using UV-Visible Spectroscopy and Photoluminescence analysis. Finally, the magnetic properties of the samples were observed using Vibrating Sample Magnetometer (VSM) at room temperature.

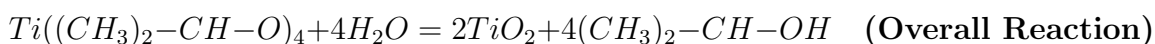
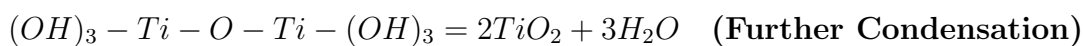
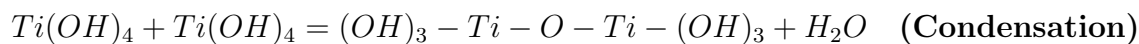
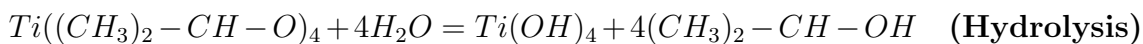
3.1 Materials synthesis

Pristine TiO_2 and $\text{Ti}_{1-x}\text{Sm}_x\text{O}_2$ ($x = 5, 10, 15$ and 20%) nanoparticles have been synthesized by sol-gel method using Titanium (IV) Tetra – isopropoxide (TTIP) and Samarium (III) Nitrate Hexahydrate as host and dopant precursors. The other reagents used in the synthesis are acetic acid and ethanol as chelating agent and solvent respectively. The chemicals that are used in materials synthesis are listed in Table 3.1. Synthesis methodology is discussed here hierarchically:

- 60 mL ethanol was taken in a beaker and then stoichiometric proportion of TTIP were dissolved in to the ethanol.
- 6 mL glacial acetic acid was slowly added and the mixed solution was stirred for 15 minutes.
- Stoichiometric proportion of deionized water (DI) was taken in another beaker and for Sm doped TiO_2 samples, stoichiometric proportion of samarium (III) nitrates were added with DI water followed by 15 minutes stirring.
- The solution which contains DI water and metal nitrates (for doped samples) was then added drop wise in to the solution which contains TTIP, ethanol and acetic acid.
- During drop wise addition of DI water, the solution color gradually turned in to white from golden.
- After addition, the mixed solution was then stirred for 1 hour at $80\text{ }^\circ\text{C}$.
- At the end of 1 hour stirring, the white solution became completely thick and dense which precludes the stirring.
- The beaker containing thick gel was then placed in to an oven at $110\text{ }^\circ\text{C}$ for 24 hours.

- The dried gel was then collected and ground using a quartz mortar and pestle. The fine powders were then thermally treated at elevated temperatures for gaining phase purity and better crystallinity.

The overall reaction can be described by following equations –



It is noteworthy to answer a simple question which could be raised from the above stated reaction equations – the synthesis process is basically a hydrolysis reaction where Titanium (IV) Tetra – isopropoxide (TTIP) reacts with water and produces TiO_2 nanoparticles, then what might be the reasons for using ethanol and acetic acid. It is true that the highly reactive TTIP precursor is sufficient to make TiO_2 nanoparticles by reaction with water but this synthesis process is too fast to control the homogeneity of the as synthesized nanoparticles. During direct hydrolysis reaction, the fast nucleation disrupts the homogeneous crystallite formation as well as the particle size distribution. For this reason, if these as synthesized nanomaterials are annealed at higher temperatures their growth would follow large variation. Another most important concern is that TiO_2 goes through a phase transition at 650 °C from anatase to rutile, so, if the growth during heat treatment follow large variation, control over phase purity will also be hampered. For these reasons, direct hydrolysis reaction is avoided and, ethanol and acetic acid have been used as solvent and chelating agents. In this process, the hydrolysis reaction is slowed which results in to formation of $Ti(OH)_4$ nanoparticles during initial condensation. For further condensation, all $Ti(OH)_4$ nanoparticles then turn in to TiO_2 which ensures homogeneous nucleation and growth of crystallites and helps to achieve uniform particle size distribution during heat treatment of the samples at elevated temperatures. However, due to precision control, amount of TTIP were fixed as multiples of five and other stoichiometric reagents were calculated and balanced. The details of synthesis parameters are listed in Table 3.2.

Table 3.1: The list of reagents used for materials synthesis

Chemical Name	Formula	Grade (%)	Supplier
Titanium (IV) Tetra – isopropoxide	Ti $[(CH_3)_2CHO]_4$	97 %	Aldrich
Samarium (III) Nitrate Hexahydrate	Sm(NO ₃) ₃ .6H ₂ O	99.9 %	Aldrich
Glacial Acetic Acid	CH ₃ COOH	99.5 %	Guanghua Sci – Tech, JHD
Ethanol	C ₂ H ₅ OH	97 %	Aldrich

Table 3.2: Detailed Synthesis Parameters for Pristine TiO_2 and $\text{Ti}_{1-x}\text{Sm}_x\text{O}_2$ ($x = 5, 10, 15$ and 20%) nanoparticles using sol-gel method:

Sample ID	TTIP (mL)	Ethanol (mL)	Acetic Acid (mL)	DI Water (mL)	Sm (III) Nitrate (gm)
TiO_2	15	60	6	15	–
$\text{Ti}_{0.95}\text{Sm}_{0.05}\text{O}_2$	15	60	6	15	1.15
$\text{Ti}_{0.90}\text{Sm}_{0.10}\text{O}_2$	15	60	6	15	2.43
$\text{Ti}_{0.85}\text{Sm}_{0.15}\text{O}_2$	10	55	5	10	2.568
$\text{Ti}_{0.80}\text{Sm}_{0.20}\text{O}_2$	5	55	5	5	1.82

The dried samples were then thermally treated in order to get rid of organic compounds which came from precursor materials and this heat treatment helped to achieve better crystallinity of the nanomaterials. A muffle furnace (Nabertherm GmbH Bahnhofstr, 20, Lilienthal / Bremen Germany) was used for annealing the dried samples at $400 - 700\text{ }^\circ\text{C}$ in air atmosphere. A basic heat treatment cycle has been shown in Figure 3.1.

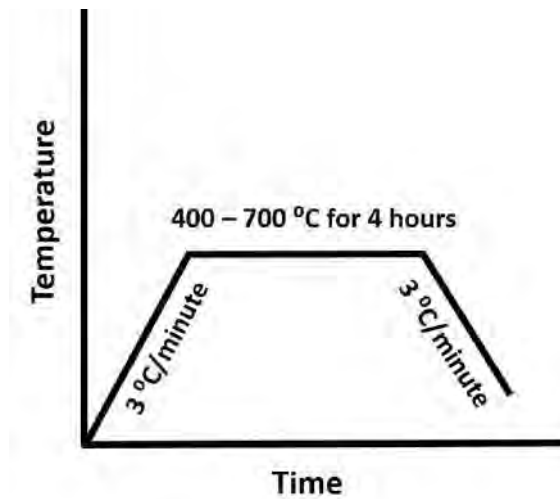


Figure 3.1: Annealing cycle for Pristine TiO_2 and $\text{Ti}_{1-x}\text{Sm}_x\text{O}_2$ ($x = 5, 10, 15$ and 20%)

3.2 X-Ray Diffraction

Crystal structures of the pristine TiO_2 and $\text{Ti}_{1-x}\text{Sm}_x\text{O}_2$ ($x = 5, 10, 15$ and 20%) samples were determined by using an X-Ray Diffractometer (EMPYREAN, PANalytical, Almelo, Netherland, Ni – filtered Cu $K\alpha$ radiation at 298 K , λ : $K\alpha_1 = 1.540598\text{ \AA}$ and $K\alpha_2 = 1.544426\text{ \AA}$) within the scanning range of $10 - 80^\circ$. In order to obtain the structural parameters, rietveld refinement of the XRD patterns were performed using X'Pert Highscore Plus software. Pseudo – Voigt function was used for modelling the Bragg peak shapes. Background, zero shift, scale factors, lattice parameters, FWHM parameters, peak asymmetry parameters and atomic positions were carefully refined.

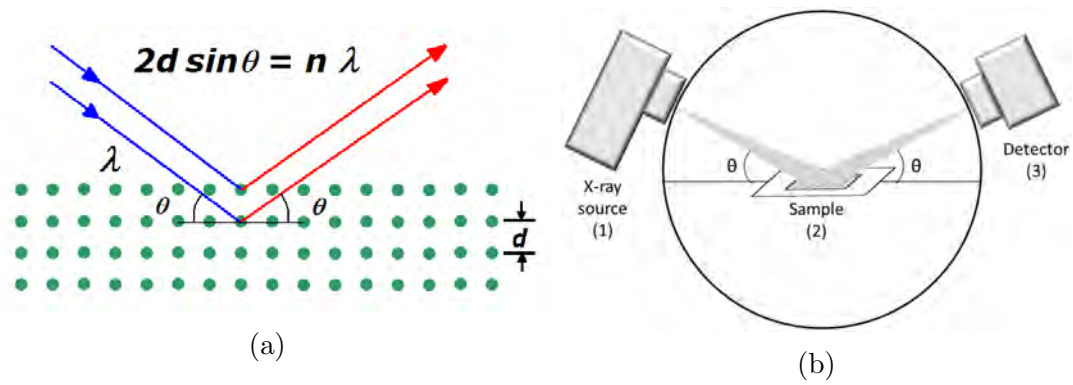


Figure 3.2: (a) Principle of X-Ray Diffraction (b) Schematic geometry of X-Ray Diffractometer

3.3 X-Ray Photoelectron Spectroscopy

X-ray photoelectron spectroscopy is a powerful characterization technique that can analyze the surface of the sample up to 2-5 nm depth. When X-rays irradiate the surface with sufficient energy, some electrons are able to attain enough energy to escape the atom. By measuring the kinetic energy of the photo-ejected electron, it is possible to determine the chemical states of the electrons. The kinetic energy, $E_{kinetic} = h\nu - E_{binding}$ where $h\nu$ is the energy of photon and $E_{binding}$ is the energy required for removing the electrons from the surface. The binding energy depends on several factors such as the element from which the electron is ejected, the orbital from which the electron is ejected, the chemical environment of the atom from which the electron is ejected. The chemical states of the elements from surface of the $Ti_{1-x}Sm_xO_2$ samples were studied by using a X-ray photoelectron spectroscopy (monochromated Al $K\alpha$ 1486 eV operated at room temperature).

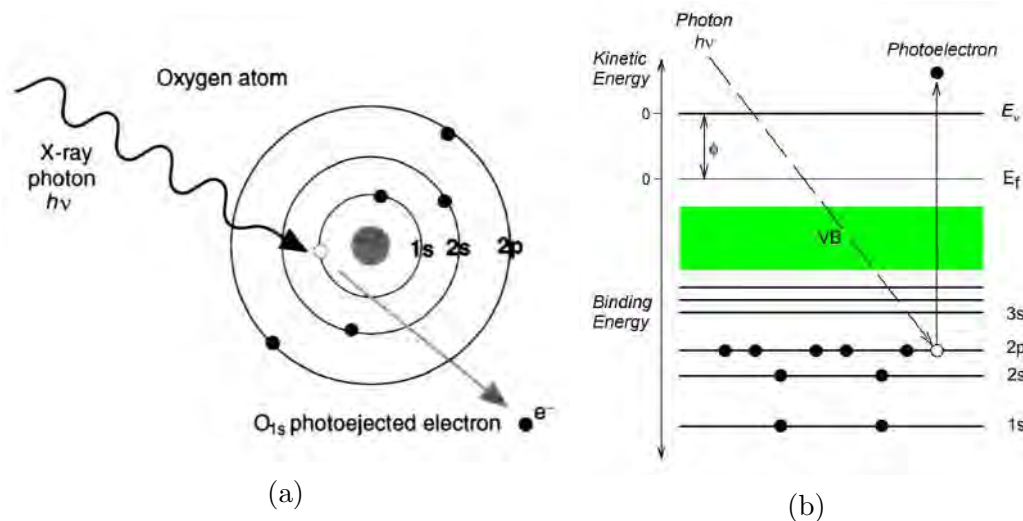


Figure 3.3: Principle of X-ray photoelectron spectroscopy

3.4 DSC And TG

Differential Scanning Calorimetry (DSC) and Thermogravimetry Analysis (TGA) were performed using a simultaneous thermal analyzer (NETZSCH STA 449 F3 Jupiter) within a heating range of 25 – 900 °C at a heating rate of 10 °C/min. DSC – TGA was performed to investigate any mass gain or mass loss of the samples due to decomposition, oxidation or moisture evaporation. Since TiO₂ undergoes a phase transition from anatase to rutile in the temperature range of 600 – 700 °C, DSC – TGA results were very useful to determine the annealing temperature to avoid the rutile phase formation during annealing.

3.5 FESEM and EDS

Morphology of the nanoparticles were observed using a Field Emission Scanning Electron Microscope (JSM 7600F, JEOL, Japan) operated with an accelerating voltage of 5 kV at 298 K. Powdered samples were dispersed in acetone followed by 10 minutes ultrasonication and then adhered with carbon tape that was attached to a Cu stub. To make these samples conductive, they were coated with Pt using ion sputtering method. Finally the Cu stub was mounted on a sample holder and inserted in FESEM. To investigate the surface and interface, cross-section polishing of the sintered pellets were performed. Atomic composition was observed by using an Energy Dispersive X – Ray Spectroscopy (EDS) detector attached with the FESEM. Multiple locations from the surface of each sintered pellets were analyzed to confirm the consistency of the average atomic composition.

3.6 TEM, SAED and STEM-EDX

Bright-field transmission electron microscopy (TEM) and measurements of electron diffraction patterns (ED) were performed with the use of JEOL 2100F microscope, operating at 200kV. Sample preparation involved dispersion of sample powders in isopropyl alcohol (HPLC grade), ultrasonication for few minutes, and dropwise addition on the surface of lacey-carbon coated TEM grid with the following removal of excesses. Selected area electron diffraction (SAED) patterns were collected from 1 μ m diameter areas. High-angle annular dark-field (HAADF) images were taken to observe the distribution of Sm throughout the samples.

3.7 Photoluminescence and UV-Vis-NIR Spectroscopy

Diffused Reflectance Spectra of the nanoparticles were collected within a wavelength range of 250 – 800 nm at 298 K using UV-Vis-NIR Spectrophotometer (LAMBDA 1050, Perkin-Elmer, USA). The optical absorbance, F(R) was estimated from diffused reflectance spectra of the powdered samples. Optical band gaps of the samples can be estimated from the following expression proposed by Tauc where $n=2$ & $\frac{1}{2}$ for indirect and direct bandgaps respectively.

$$(\alpha h\nu)^{\frac{1}{n}} = A(h\nu - E_g)$$

Here, A is the proportional constant and α is the absorption coefficient which can be written as Kubelka – Munk function $F(R) = \frac{(1-R)^2}{2R}$ where R is the reflectance found for the samples. So, substituting α with F(R) in the above equation:

$$[F(R)h\nu]^{\frac{1}{n}} = A(h\nu - E_g)$$

The slope on the $[F(R)h\nu]^{\frac{1}{n}}$ vs. photon energy (E) graph cuts x axis at $[F(R)h\nu]^{\frac{1}{n}} = 0$ which corresponds to the optical bandgap, E_g of the particular sample.

Photoluminescence spectra were collected by using a fluorescence spectrometer (Hitachi F-7000 equipped with a Xe lamp as excitation source) with 270 nm laser excitation which corresponds to 4.6 eV. Before measurement, 1 mg of nanoparticles were taken in distilled water and diluted until the solution looks like transparent. At first, experiment was performed for only distilled water for baseline correction and then emission peaks were observed for pristine and Sm:TiO₂ samples.

3.8 Vibrating Sample Magnetometer

Vibrating sample magnetometer (VSM) was used to study magnetization vs. applied field characteristics of the samples at 300 K and 5 K. The principle of VSM is basically the law of induction proposed by Faraday which implies that a change in magnetic field will produce an electric field. During VSM, the sample was placed in constant magnetic field and the larger the applied field, the stronger magnetization of the sample will be noticed. The magnetic dipole moments/spins induce a magnetic field around the sample. The sample is constantly vibrated and the change in the position will change the magnetic field of sample. This change in magnetic field as a function of time is recorded by pick-up coils. The electric field sensed by the pick-up coils are amplified and used to measure the degree of magnetization of the samples. In this research, the magnetic property of Ti_{1-x}Sm_xO₂ samples were measured by using a VSM detection module in Quantum Design Physical Property Measurement System (PPMS).

CHAPTER 4

RESULTS & DISCUSSIONS

4.1 Structural analysis by X-Ray Diffraction

The as synthesized TiO_2 nanoparticles were sintered at elevated temperatures in the range of 400 to 700 °C. At 400 °C, the TiO_2 nanoparticles show pure anatase phase (space group $I41/amd$) which has been found persistent in the TiO_2 nanoparticles sintered at 600 °C as showed in Fig 4.1(a). At 700 °C, a small peak appeared at $2\theta=27^\circ$ which can be indexed as (110) plane of rutile phase. The percentage of this rutile phase was 2% according to the rietveld refinement of the XRD pattern. From Fig 4.1 (a) & (b) it seems that the sintering of the nanoparticles only reduces the peak broadening which indicates an increase in crystal size of the nanoparticles with sintering temperature. However, no peak shift was noticed due to sintering of the pristine TiO_2 nanoparticles.

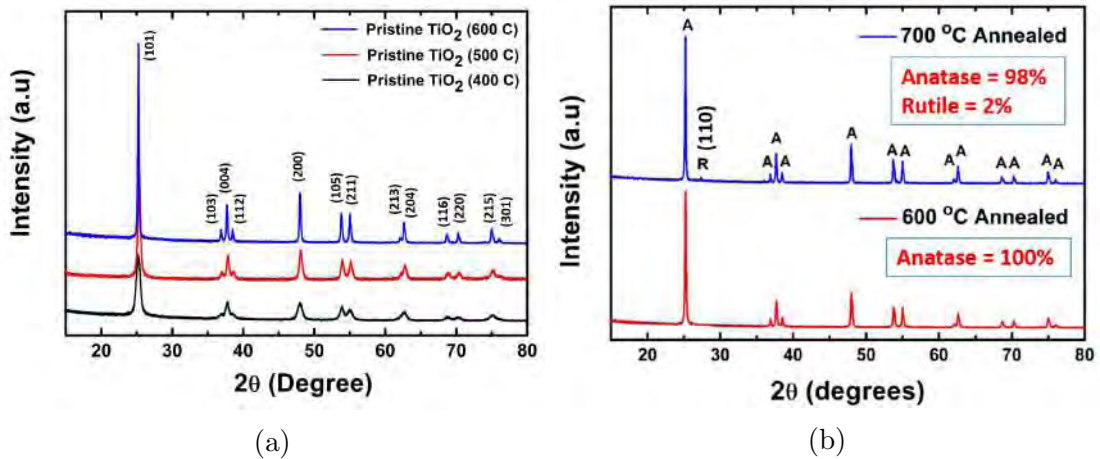


Figure 4.1: (a) X – ray diffraction patterns of Pristine TiO_2 samples annealed at 400, 500 and 600 °C (b) Comparison between pristine TiO_2 samples annealed at 600 and 700 °C. In 700 °C annealed sample, a small percentage of rutile TiO_2 was noticed which was absent in 600 °C annealed TiO_2 sample.

Fig 4.2 (a) & (b) shows the XRD patterns of $\text{Sm}:\text{TiO}_2$ samples sintered at 400 and 700 °C. From the peak broadening it can be clearly seen that the Sm substitution suppressed the crystallinity. Although, there's no peak of rutile phase was found in the XRD pattern of the $\text{Sm}:\text{TiO}_2$ samples at least within the XRD detection limit, there's an amorphous hump in the 2θ range of 25 to 30°. For this reason, slow scan of XRD patterns of the $\text{Sm}:\text{TiO}_2$ samples sintered at 700 °C were performed using the same diffractometer setup as before. The scanning rate was fixed to be 0.041683 °/sec. The slow scanned XRD patterns are showed in Fig 4.3 (a) which reveals the presence of a semi-crystalline phase other than anatase in $\text{Ti}_{0.8}\text{Sm}_{0.2}\text{O}_2$ sample. The small peak at $2\theta=27.5^\circ$ can be indexed as (222) of cubic Sm_2O_3 phase and the percentage of this semi-crystalline phase is around 2.8%.

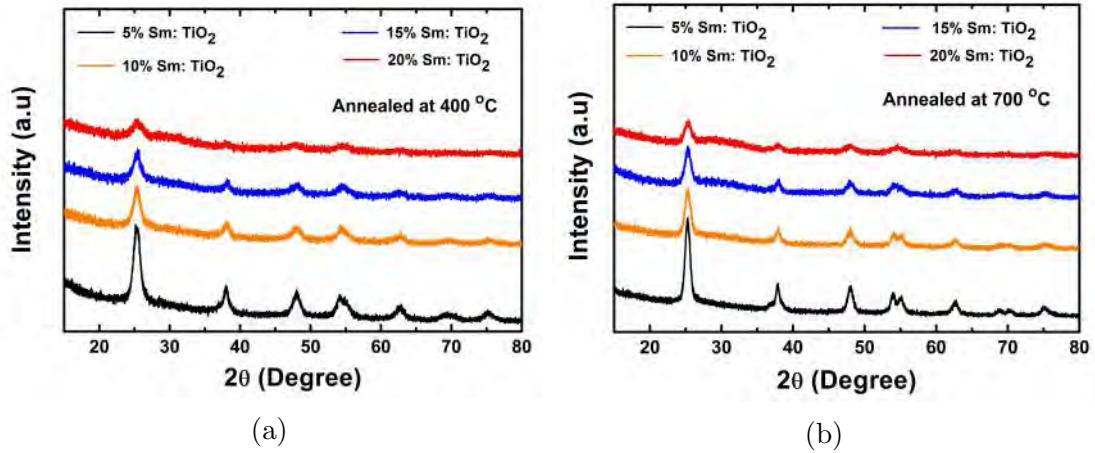


Figure 4.2: (a) & (b) X – ray diffraction patterns of $\text{Ti}_{(1-x)}\text{Sm}_{(x)}\text{O}_2$ samples annealed at 400 and 700 °C.

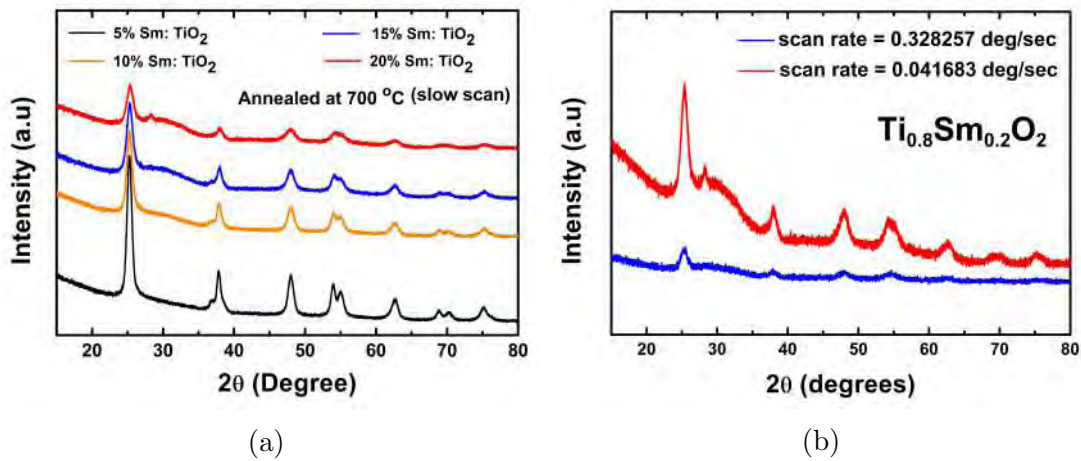


Figure 4.3: (a) Slowly scanned X – ray diffraction patterns of $\text{Ti}_{(1-x)}\text{Sm}_{(x)}\text{O}_2$ samples annealed at 700 °C. (b) Comparison between fast scanned and slow scanned XRD patterns of $\text{Ti}_{0.8}\text{Sm}_{0.2}\text{O}_2$ sample.

From the XRD patterns showed in Fig 4.3 (a) and the rietveld refinement, it can be safely elucidated that the amorphous hump seen in the 10 and 15% Sm:TiO₂ samples also came from the cubic Sm₂O₃ phase. The lattice parameters estimated from rietveld refinement are showed in Fig 4.4 (f) & (g). Vegard's law suggests that within solid solubility limit the cationic substitution changes the lattice parameters in a linear manner. It implies that Vegard's law was not followed for 15 and 20 % Sm:TiO₂ samples. Besides, the trend of turning the amorphous hump in to a semi-crystalline curve indicates that the Sm₂O₃ phase might form in a very amorphous thin layer in $\text{Ti}_{0.95}\text{Sm}_{0.05}\text{O}_2$ sample and the thickness of the layer increased with higher percentage of Sm substitution. According to this concept, the thickness of the amorphous layer around the anatase increased beyond a critical limit for 20% Sm substitution which might be the reason of the appearance of the semi-crystalline Sm₂O₃ phase in $\text{Ti}_{0.8}\text{Sm}_{0.2}\text{O}_2$ sample.

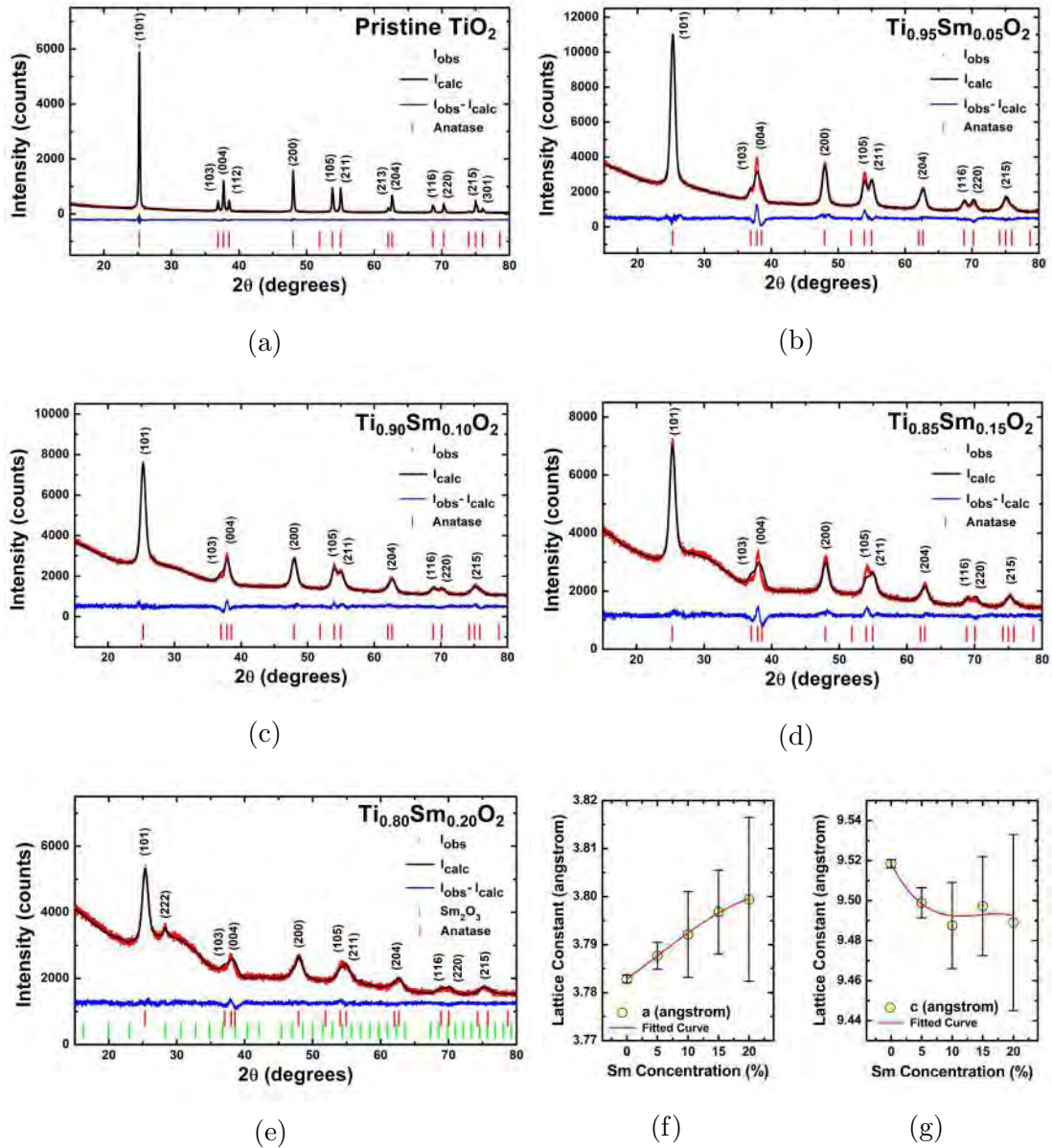


Figure 4.4: (a-e) Rietveld refinement patterns of $\text{Ti}_{(1-x)}\text{Sm}_{(x)}\text{O}_2$ samples. The observed and calculated data are showed as red filled circle and black straight line respectively. The difference between observed and calculated values is plotted with blue straight line. The Bragg peak positions for Anatase and Sm_2O_3 are showed with vertical lines. (f-g) The estimated lattice parameters from rietveld refinement. The polynomial curve fitting clearly shows a deviation of Vegard's law for the higher percentage of Sm substitution in TiO_2

The percentage of Sm substitution can be estimated from rietveld refinement. For 5% Sm: TiO_2 sample, the structural refinement shows that the percentage of Sm in anatase was $2.6(\pm 0.6)\%$. It can be stated that the solid solubility limit of Sm substitution in anatase might exceed even in 5% Sm: TiO_2 sample. However, the possibility of Sm_2O_3 phase's presence in segregated grain is ruled out due to the nature of the amorphous hump's transition in to a semi-crystalline phase with higher percentage of Sm substitution. A rough estimation of crystallite size was obtained

Table 4.1: Estimated lattice parameters a & c , crystallite size (D) & refinement factors for $Ti_{1-x}Sm_xO_2$ ($x = 0, 5, 10, 15$ and 20%)

Sample ID	a (Å)	c (Å)	D (nm)	R_p	R_{wp}	R_{exp}	GoF
Pristine TiO_2	3.7829(8)	9.518(2)	44.68	6.13	8.17	7.29	1.12
$Ti_{0.95}Sm_{0.05}O_2$	3.788(3)	9.499(8)	10.25	2.61	4.09	2.22	1.84
$Ti_{0.90}Sm_{0.10}O_2$	3.792(9)	9.49(2)	9.68	1.98	2.66	2.17	1.22
$Ti_{0.85}Sm_{0.15}O_2$	3.797(9)	9.50(2)	8.48	2.0	3.01	1.97	1.52
$Ti_{0.80}Sm_{0.20}O_2$	3.80(2)	9.49(4)	8.24	1.69	2.21	1.98	1.11

from the FWHM and 2θ values of (101) peak of anatase phase by using Scherrer's formula, $D = \frac{0.9 \times \lambda}{\beta \times \cos \theta}$. The lattice parameters, crystallite size and the refinement factors are listed in Table 4.1.

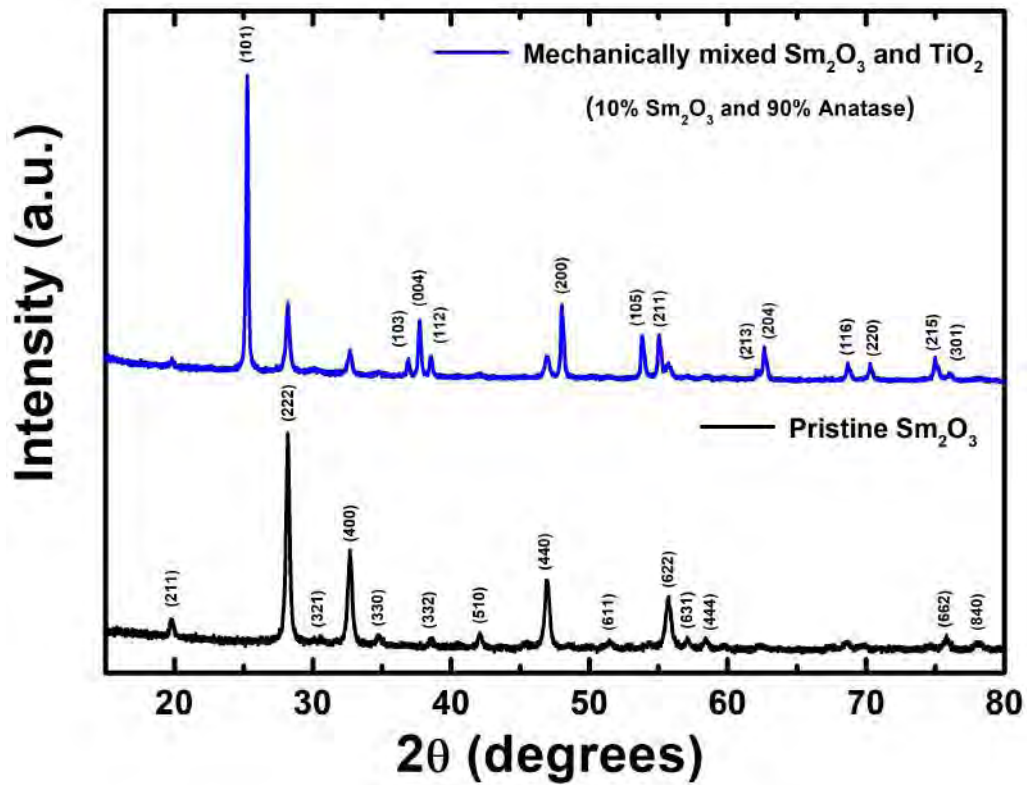


Figure 4.5: X-Ray Diffraction patterns of pure Sm_2O_3 and mechanically mixed pure Sm_2O_3 with pure TiO_2

In order to understand the Sm_2O_3 formation in $Ti_{1-x}Sm_xO_2$ samples, pure Sm_2O_3 was synthesized using samarium nitrate, ethanol and acetic acid. The stoichiometry of the precursors was similar to the stoichiometry of samarium nitrate:ethanol:acetic acid in $Ti_{0.8}Sm_{0.2}O_2$. Then the as synthesized powders were heat treated at $700^\circ C$. The XRD pattern revealed that the heat treated nanoparticles were of pure Sm_2O_3 phase. However, this pure Sm_2O_3 was then mechanically mixed with pure TiO_2 using a quartz mortar for one hour. The XRD pattern of the mechanically mixed nanoparticles showed that they were composed of 90%

anatase phase and 10% Sm_2O_3 phase. The main purpose of this additional experiment was to observe the Sm_2O_3 formation in same experimental environment. The highly crystalline XRD pattern of mechanically mixed pure Sm_2O_3 with pure TiO_2 indicates that the probability of independent Sm_2O_3 phase nucleation during $Ti_{1-x}Sm_xO_2$ synthesis might be ruled out. This implies that the semicrystalline phase of Sm_2O_3 in $Ti_{0.8}Sm_{0.2}O_2$ might be formed around the anatase grain beyond the solid solubility limit of Sm substitution in TiO_2 .

4.2 Thermal property analysis by DSC-TG

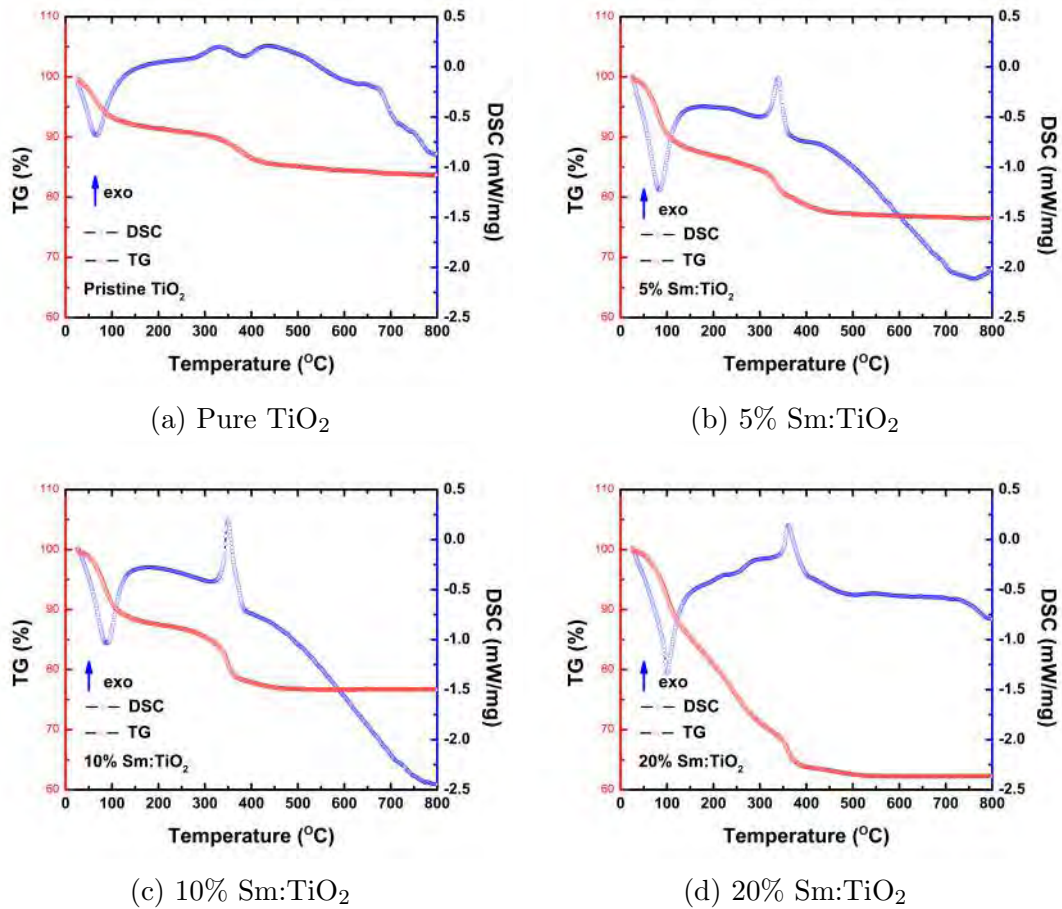


Figure 4.6: DSC-TG analysis of pure and Sm: TiO_2 samples

Fig 4.5 shows the differential scanning calorimetry and thermogravimetry analysis of the samples. For pristine, 5 and 10% Sm: TiO_2 samples, two weight loss regions can be identified. The first one takes place in the temperature range of 25-150 °C which is due to release of the adsorbed water in the samples. The second weight loss between 150-450 °C is due to thermal decomposition of organic compounds in precursors. The sharp fall of TG graph of 20% Sm: TiO_2 sample indicates that the desorption of water was instantly followed by the decomposition of organic materials in this sample. The endothermic peak at 75 °C might be attributed to the desorption of adsorbed water and the exothermic peak at around 350 °C might be attributed to the thermal decomposition of organic compounds.

4.3 Morphology analysis by FESEM

Field emission scanning electron microscopy images of Pristine and Sm:TiO₂ samples show homogeneous distribution of large aggregates of spherical nanoparticles. Suppression in particle size with Sm substitution is visible if carefully noticed. Elemental compositions (Sm, Ti and O) of the pristine and Sm:TiO₂ samples are estimated using energy dispersive X-ray analysis. The proportion of the constituent elements as well as the Ti/Sm ratio are found to be close to the intended values.

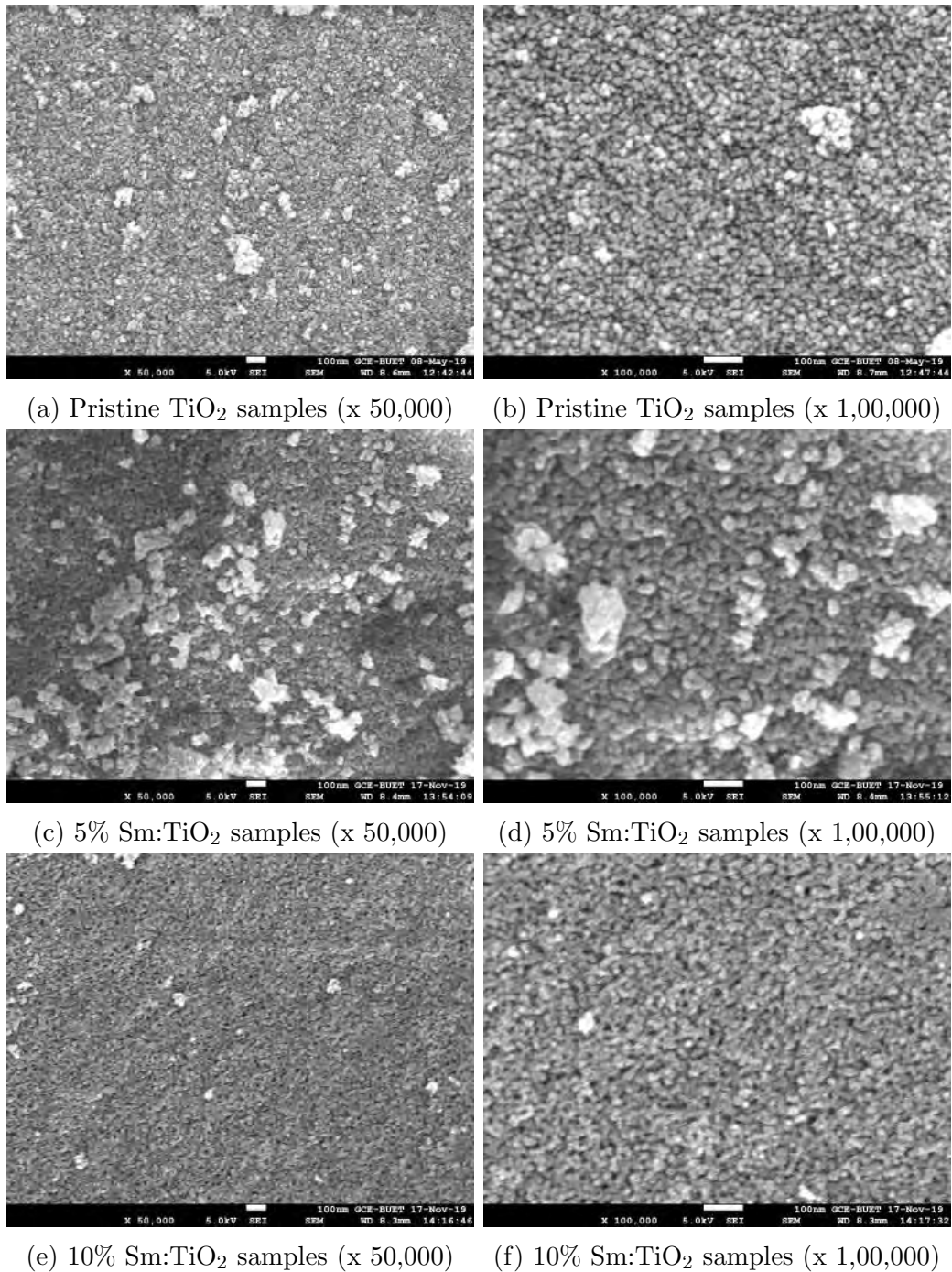


Figure 4.7: Field emission scanning electron microscopy images of Pristine, 5 and 10% Sm:TiO₂ samples

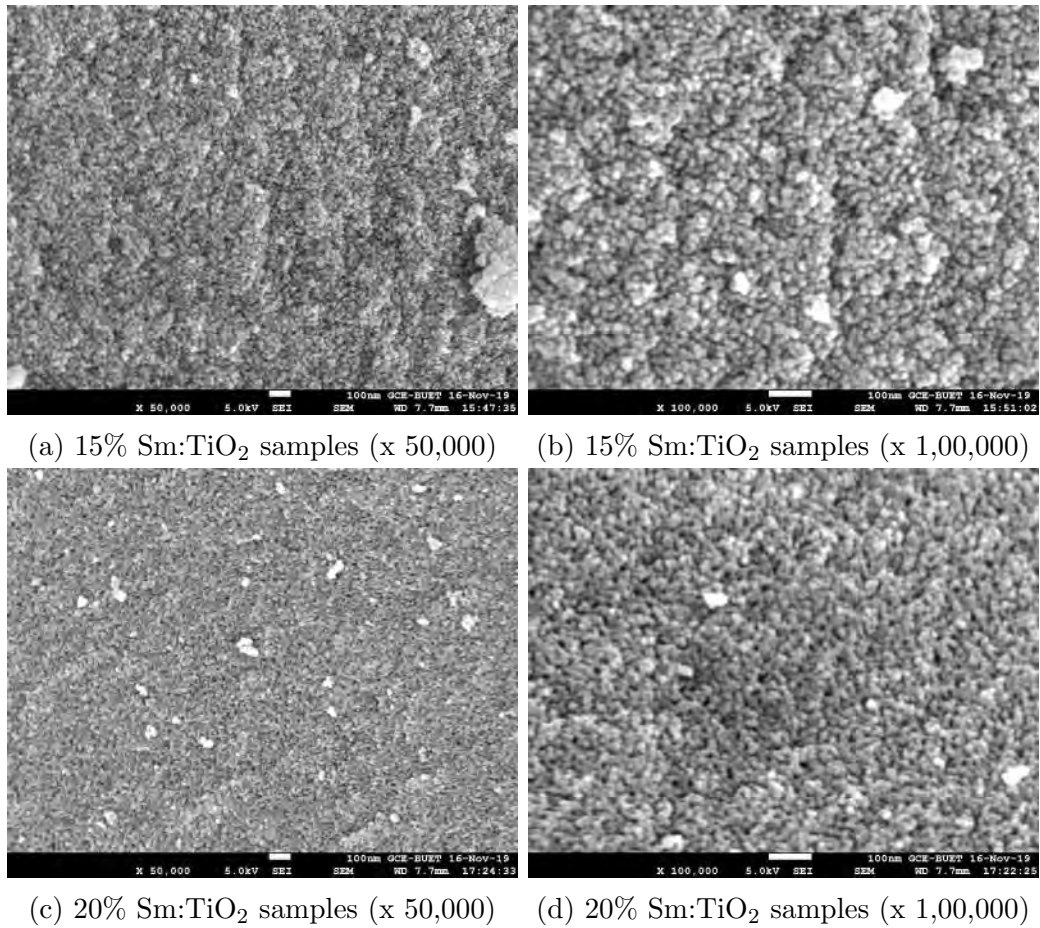


Figure 4.8: Field emission scanning electron microscopy images of 15 and 20% Sm:TiO₂ samples

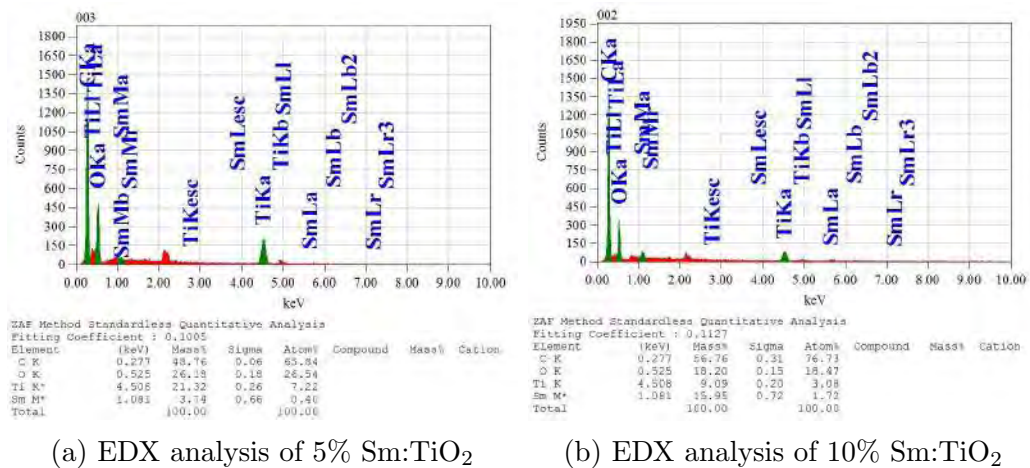
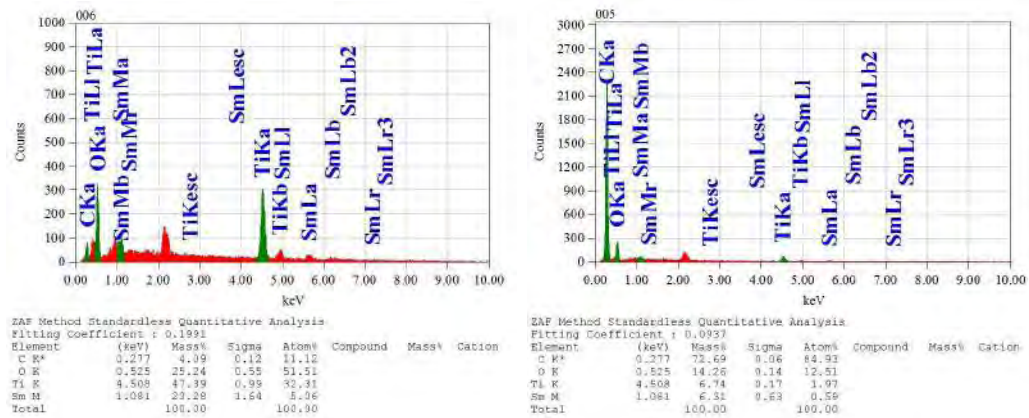


Figure 4.9: Energy dispersive X-ray analysis of elemental composition of 5 and 10% Sm:TiO₂ samples



(a) EDX analysis of 15% Sm:TiO₂ (b) EDX analysis of 20% Sm:TiO₂

Figure 4.10: Energy dispersive X-ray analysis of elemental composition of 15 and 20% Sm:TiO₂ samples

4.4 Structural and morphology analysis by Transmission Electron Microscopy

Figure 11 and 12 show the high resolution images of pristine and Sm:TiO₂ samples taken by Transmission Electron Microscopy. The samples show large micron size aggregates which consist of very small grains. For all samples, grain size distributions were calculated and the distributions were approximated by the lognormal distribution.

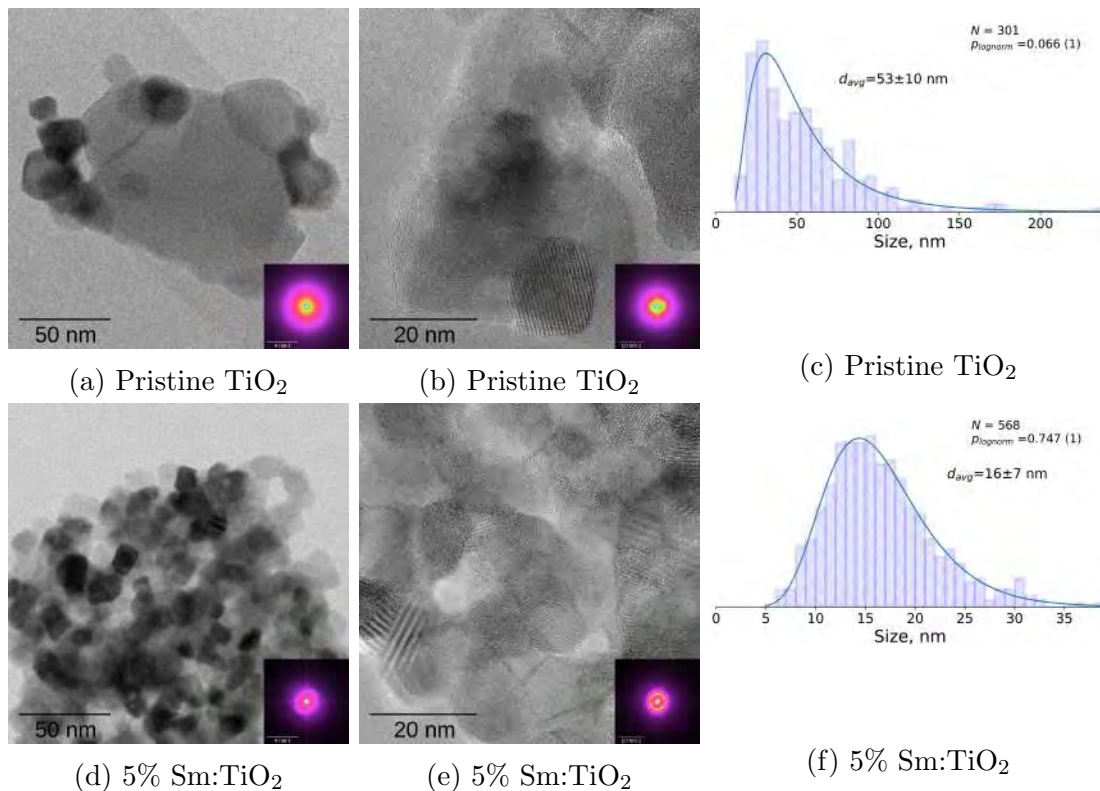


Figure 4.11: (a-f) Comparison of TEM images and grain size distributions of Pristine and 5% Sm:TiO₂ samples

Corresponding mean values with standard deviations were also obtained and shown in figures. The average grain size of the pristine TiO_2 and 5% $\text{Sm}:\text{TiO}_2$ nanoparticles were estimated as $53(\pm 10)$ and $16(\pm 7)$ nm respectively. For 5, 10 and 15% $\text{Sm}:\text{TiO}_2$ nanoparticles, the average grain size were estimated as $12(\pm 3)$, $13(\pm 4)$ and $10(\pm 3)$ nm respectively. The grain size distributions implies that substitution of 5% Sm results in the decrease of grain size but further increase of Sm content did not lead to any significant decrease of grain sizes of the samples.

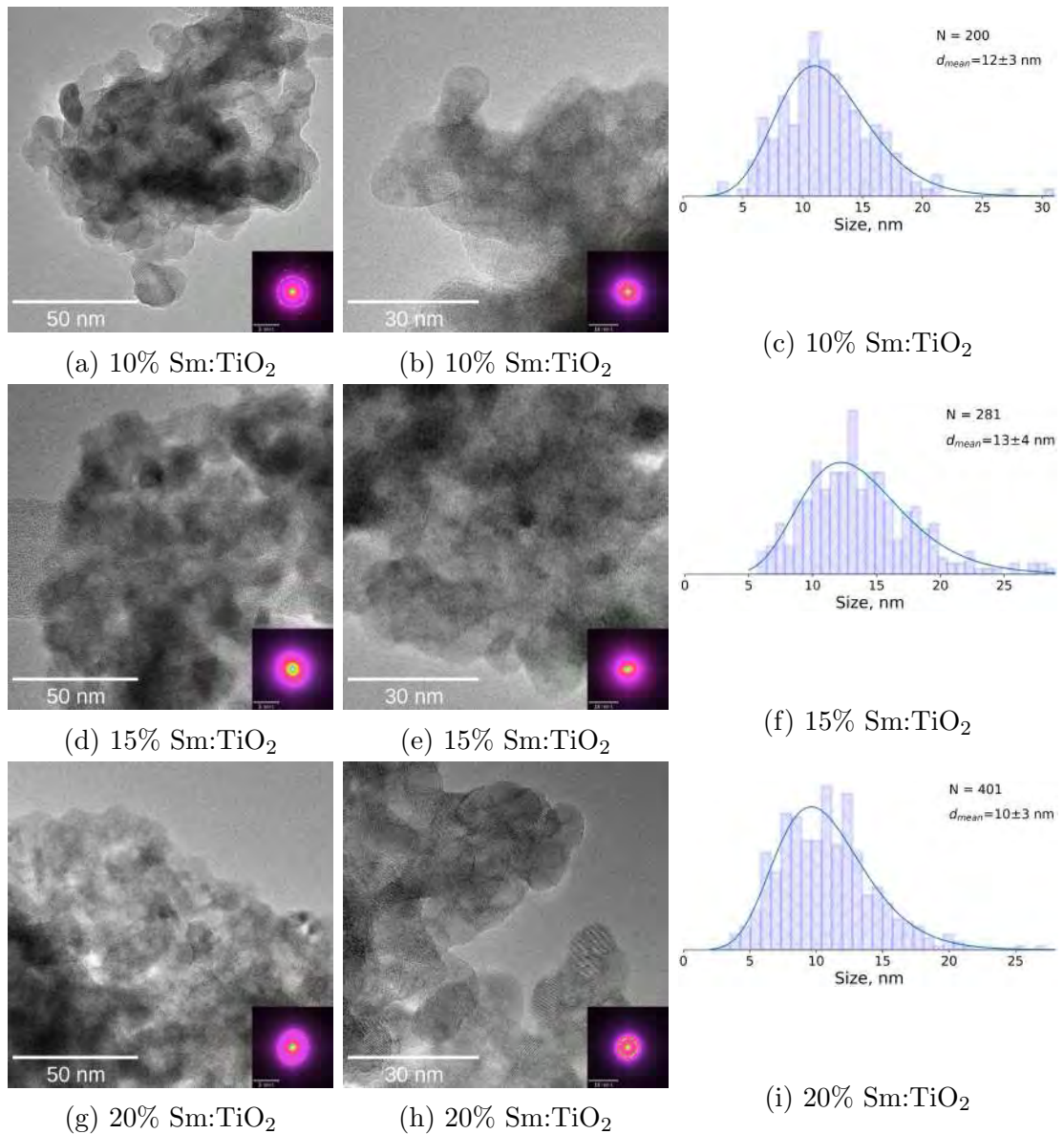


Figure 4.12: (a-i) Comparison of TEM images and grain size distributions of 10, 15 and 20% $\text{Sm}:\text{TiO}_2$ samples

The inset shows the corresponding fast fourier transformed (FFT) images which are recorded in reciprocal space. The bright spots in the FFT image are the indication of highly crystalline nature of pristine TiO_2 and each of these spots resemble different crystallographic planes. FFT of HRTEM images provide fascinating way to calculate the interplanar spacing between two crystallographic planes and the ex-

amples are showed in Figure 4.13 (a) & (b). It is noteworthy to mention that before taking FFT as well as HRTEM image, the electronic transmission should be aligned towards a specific zone axis of the material. For thin film, it's not very difficult task to specify the zone axis before taking images but for aggregated polycrystalline nanoparticles it's impossible to obtain images focusing any specific zone axis due to the overlapping of nanoparticles. For that reason, there remains a deviation between the values of interplanar distances calculated from XRD and HRTEM data.

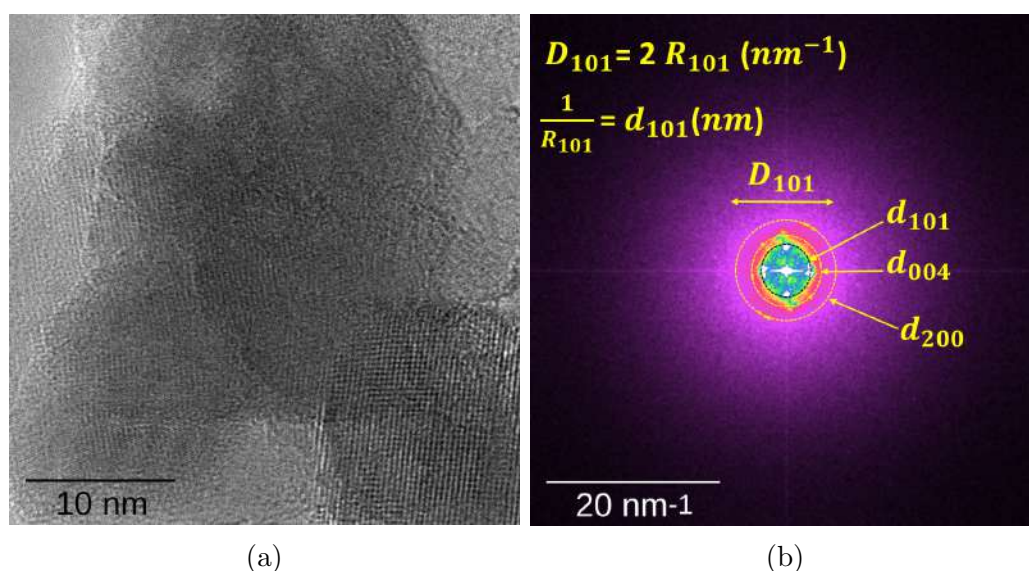


Figure 4.13: High Resolution TEM images and their corresponding FFT images for lattice spacing estimation of Pristine TiO₂

The bright spots can be considered to comprise of a circle and the inverse of the circle radius is the interplanar spacing (d) in nanometer scale. As shown in Fig 4.13 (b), the yellow dotted circles represent (101), (004) and (200) planes of anatase phase. The calculated d spacing values of (101), (004) and (200) planes are 3.42, 2.30 and 1.82 Å respectively. These values can also be obtained from XRD data using Bragg's law, $n \times \lambda = 2d \sin \theta$. From, XRD data, the d spacing values of (101), (004) and (200) planes are 3.52, 2.38 and 1.89 Å respectively. As it's stated before that HRTEM images are taken without specifying any zone axis for polycrystalline aggregated nanoparticles and hence there will be a deviation in the d spacing values obtained from XRD and TEM data. Here, it seems that the observed d spacing values from TEM are within ± 0.1 of the d spacing values estimated from XRD data. However, from the HRTEM images it can be clearly elucidated that no rutile phase was present in the pristine TiO₂ sample.

Selective Area Electron Diffraction patterns of Pristine, 5 and 15% Sm:TiO₂ samples are showed in Fig 4.14. The bright spots in the SAED pattern of Pristine TiO₂ indicate the highly crystalline nature of the nanoparticles. Similarly, the diffused circular rings in the SAED pattern of 5 and 15% Sm:TiO₂ correspond to low degree of crystallinity of the nanoparticles. It is noteworthy to mention that except anatase no other phase is noticed in the electron diffraction patterns. But from X-ray diffraction of 20% Sm:TiO₂, a semi-crystalline phase of Sm₂O₃ was identified.

This led to the concept that the semi-crystalline Sm_2O_3 phase might be formed as very thin layer around the anatase grain and for that reason, the Sm_2O_3 phase could not be distinguishable in HRTEM images as well as in electron diffraction patterns.

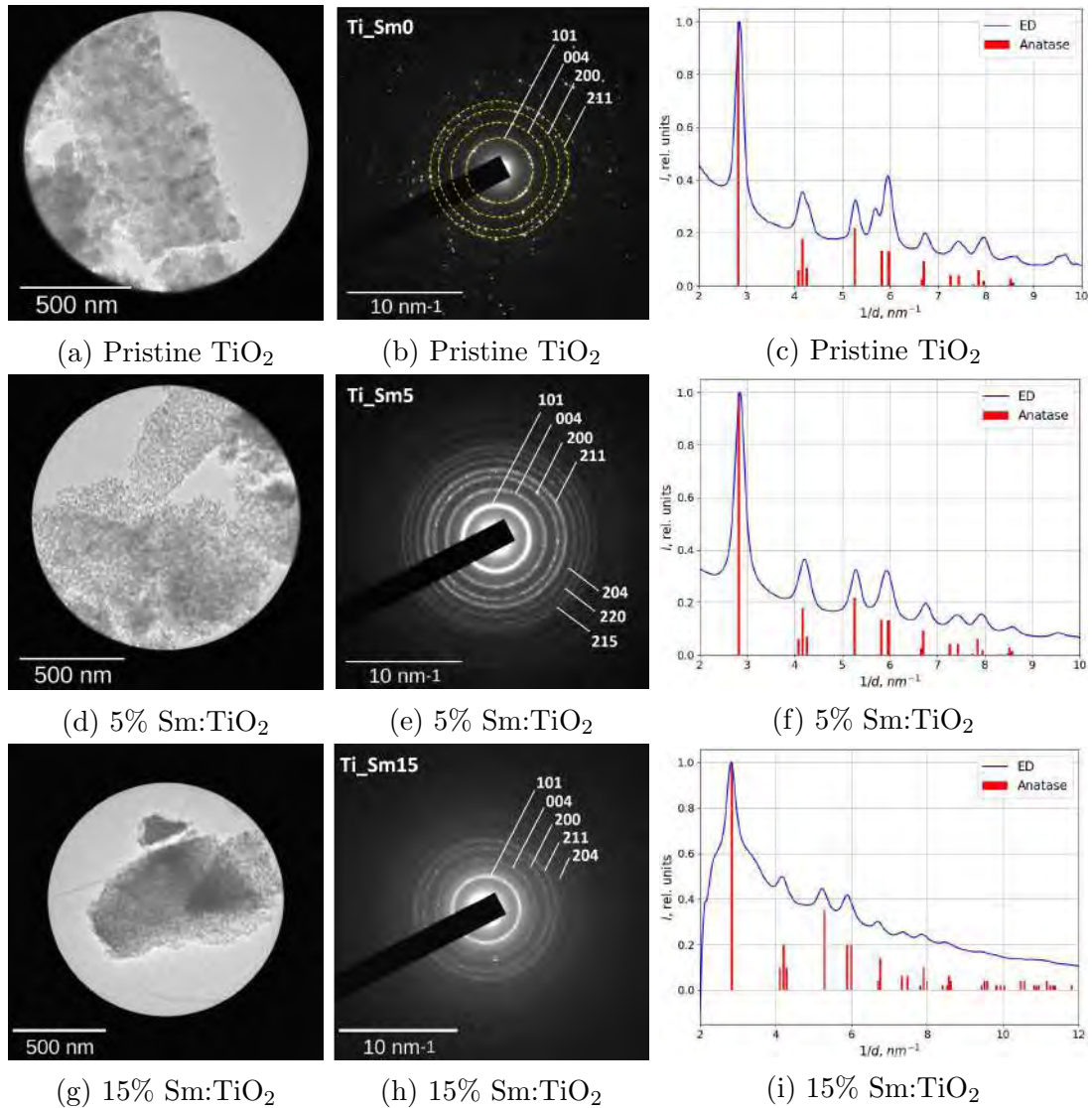


Figure 4.14: Comparison of Selective Area Electron Diffraction (SAED) patterns of Pristine, 5% and 15% $\text{Sm}:\text{TiO}_2$ samples

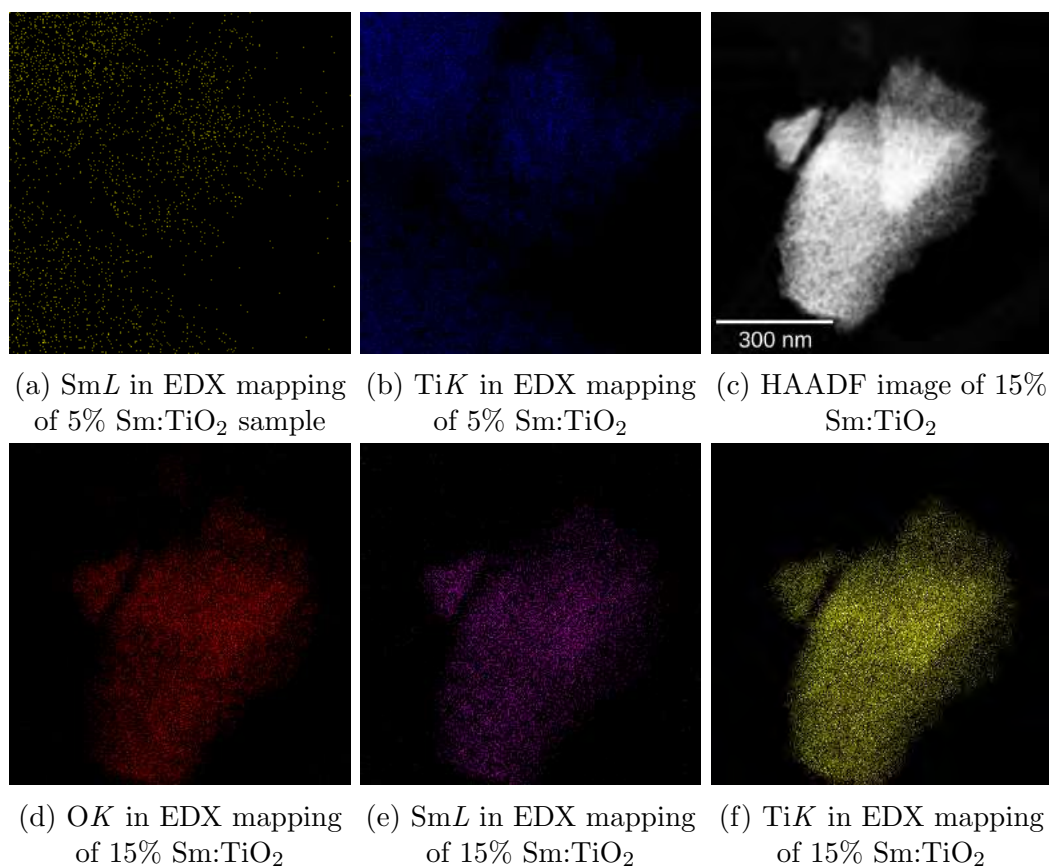


Figure 4.15: EDX mapping shows the homogeneous distribution of Sm, O and Ti in 5% and 15% Sm:TiO₂ samples

4.5 Chemical and electronic states analysis by XPS

In order to observe electronic and chemical states of elements, wide scan XPS spectra of pure and 5% Sm:TiO₂ samples were recorded as showed in Fig 4.16. High resolution XPS spectra were also recorded for core level electrons of C 1s, O 1s, Ti 2p and Sm 3d as showed in Fig 4.17 to 4.20. During heat treatment of the as-prepared samples, the samples could not get rid of carbonaceous elements because of muffle furnace. The carbons from thermally decomposed organic compounds were trapped inside the furnace and adhered to the samples. Total concentration of O 1s, C 1s and Ti 2p states in pristine TiO₂ sample was 51.26%, 27.41% and 21.33% respectively. In 5% Sm:TiO₂ sample, the total concentration of O 1s, C 1s, Ti 2p and Sm 3d states are 52.64%, 24.07%, 20.68% and 2.60% respectively.

Ti 2p core level electrons show two characteristic peaks for Ti $2p_{3/2}$ and $2p_{1/2}$ states. The prominent peak at 458.8 eV in both samples can be attributed to Ti $2p_{3/2}$ which corresponds to Ti^{4+} state. The satellite like peak at 457.1 eV observed in both samples can be attributed to the Ti^{3+} state. The concentration of Ti^{3+} in 5% Sm:TiO₂ sample (1.88%) are found to be higher than in the pristine TiO₂ sample (0.82%). This implies the substitution of Ti^{4+} by Sm^{3+} in the doped sample. However, a small percentage of Ti^0 (0.45%) and Ti^{2+} (1.74%) were also noticed in the doped sample.

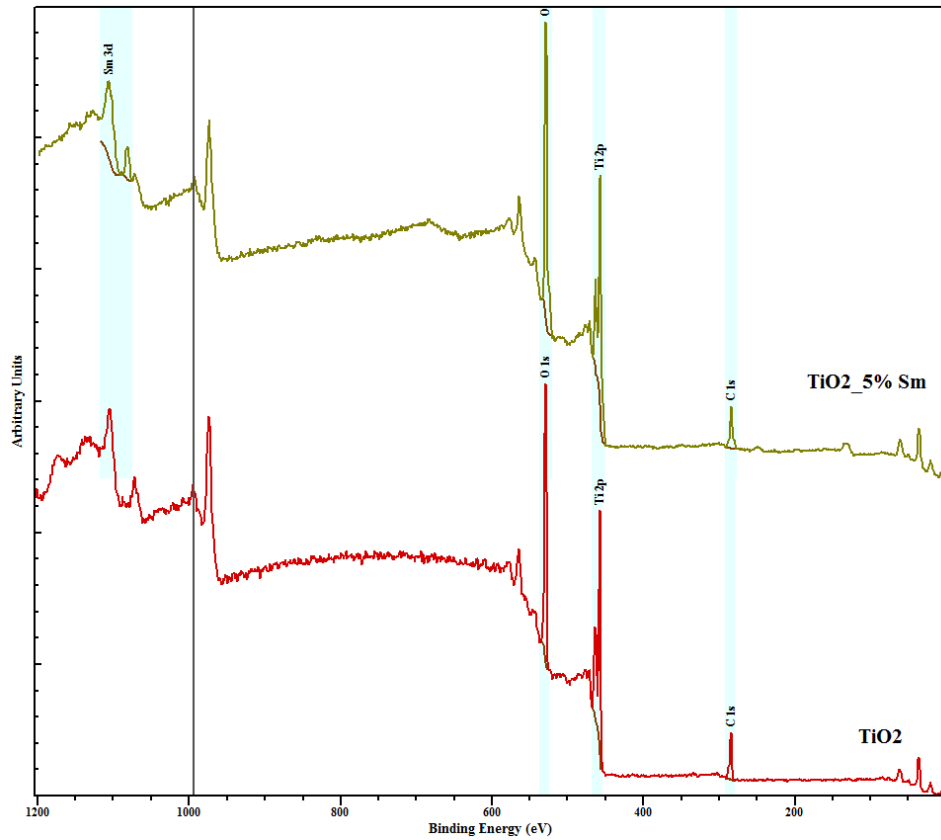


Figure 4.16: X-ray photoelectron spectra of Pristine and 5% Sm:TiO₂ samples

From the high resolution XPS spectra of Sm 3d core level electrons, the two prominent peaks can be identified at 1084 eV and 1108 eV and they correspond to Sm 3d_{3/2} and Sm 3d_{5/2} of Sm³⁺ state. The concentration of Sm³⁺ in doped sample is 2.76%. However, no metallic cluster of Sm was found in the high resolution XPS spectra. The high resolution XPS of O 1s is showed in Fig 4.21. The prominent peak at 529.9 eV in both samples can be attributed to the Ti-O bond in TiO₂ crystal. The wide peak at 531.5 eV can be attributed to the oxygen which is in hydroxyl (OH) bond. The concentration of O 1s electrons in Ti-O and O-H bond was 43.58% and 6.8% respectively for pristine sample. In doped sample, the concentration of O 1s electrons in Ti-O/Sm-O was 43.14% and in O-H bond was 6.69%.

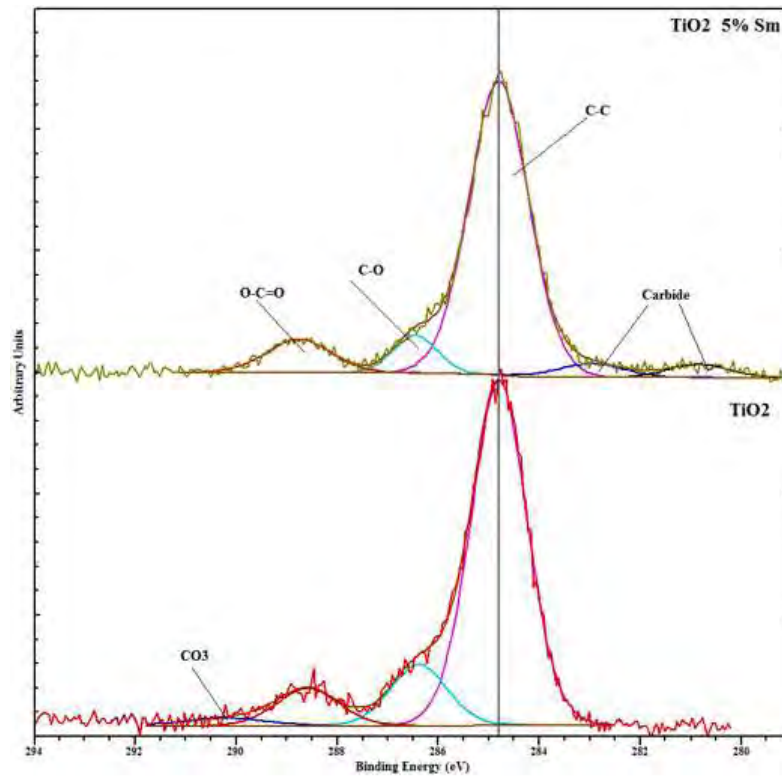


Figure 4.17: X-ray photoelectron spectra of C 1s in 5% Sm:TiO₂ sample

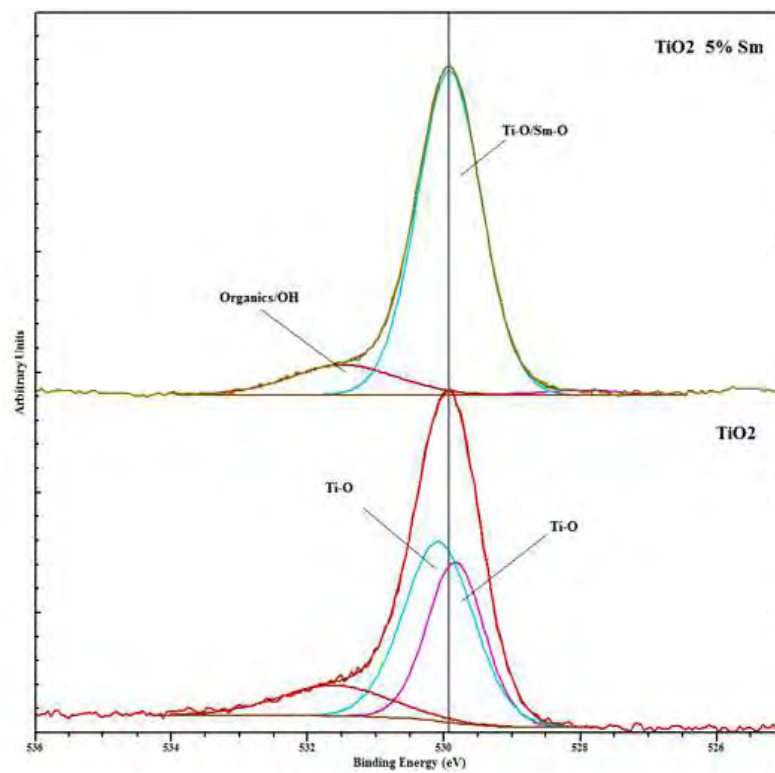


Figure 4.18: X-ray photoelectron spectra of O 1s in 5% Sm:TiO₂ sample

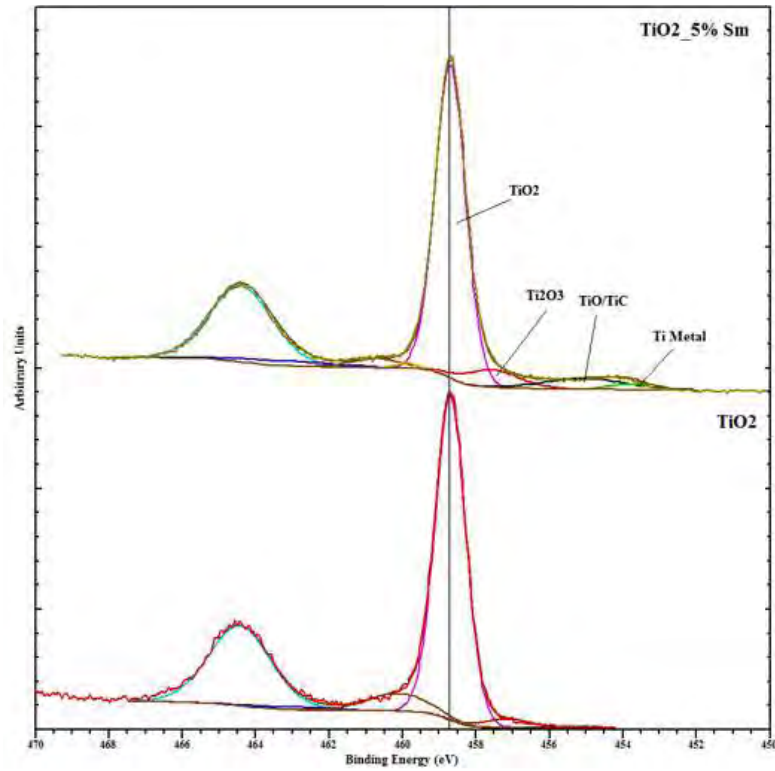


Figure 4.19: X-ray photoelectron spectra of Ti 2p in 5% Sm:TiO₂ sample

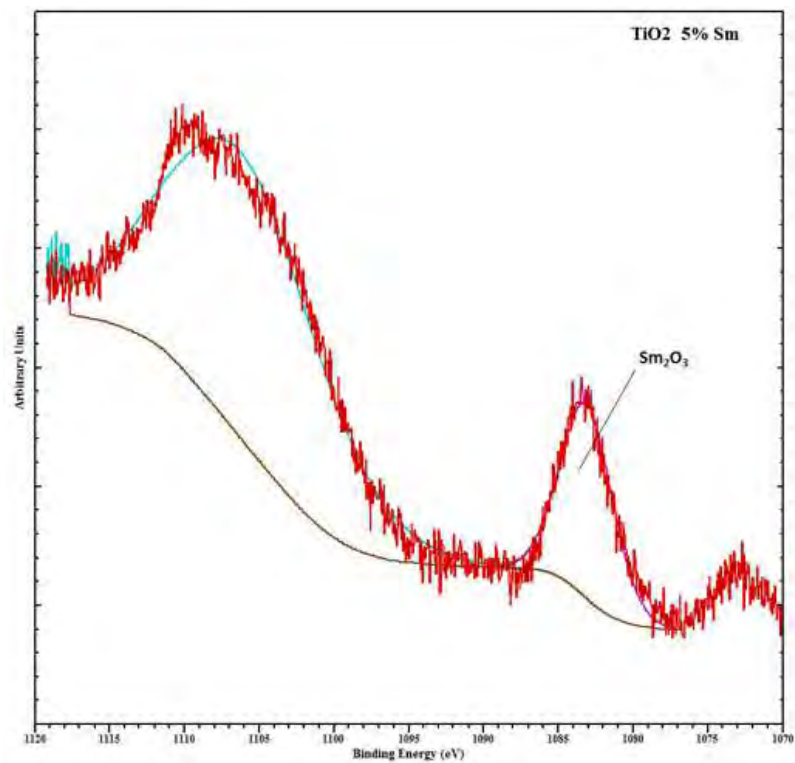


Figure 4.20: X-ray photoelectron spectra of Sm 3d in 5% Sm:TiO₂ sample

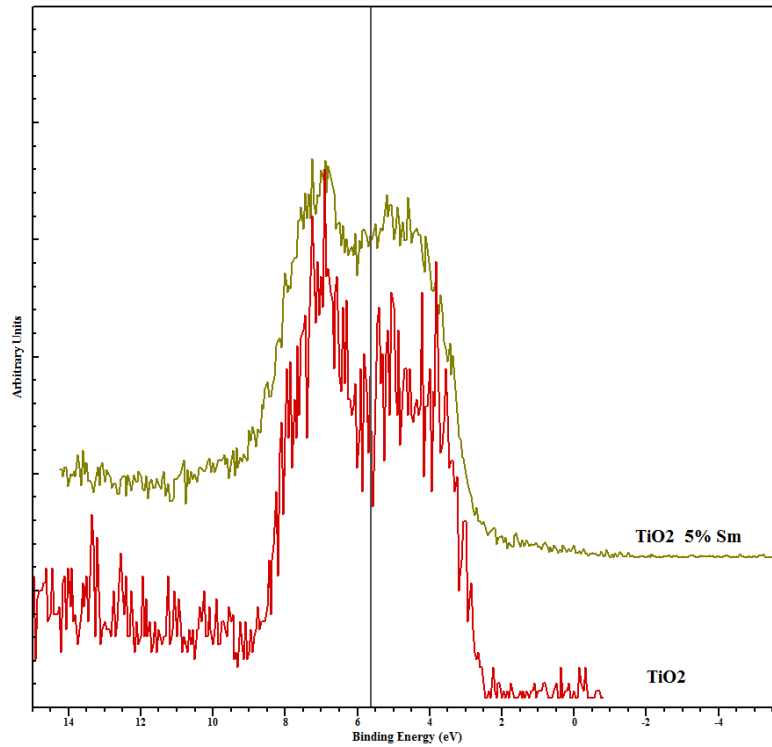


Figure 4.21: Valence band spectra of pristine and 5% Sm:TiO₂ samples

4.6 Optical property analysis by UV-Vis-NIR and Photoluminescence Spectroscopy

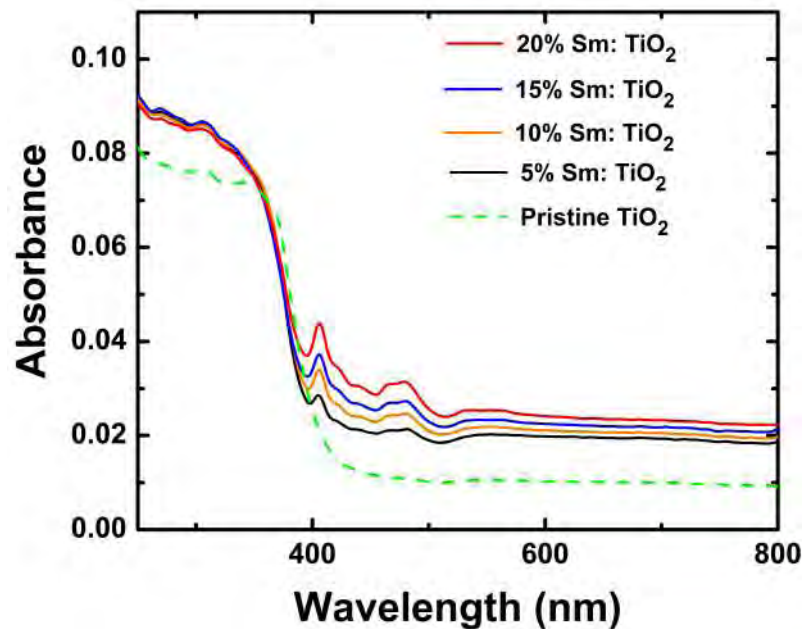


Figure 4.22: Absorption spectra of pristine and Sm:TiO₂ samples obtained from diffused reflectance spectroscopy

The optical absorbance, $F(R) = \frac{(1-R)^2}{2R}$ was estimated from diffused reflectance spectra of the powdered samples and showed in Fig 4.22. Although no redshift

of absorbance edge was noticed due to Sm substitution, two absorbance peaks appeared within visible range and gradually becomes prominent with the increase in percentage of Sm substitution. The appearance of these absorbance peaks might be attributed to the presence of semi-crystalline Sm_2O_3 phase in the Sm:TiO₂ samples. The optical bandgap was obtained by using Kubelka-Munk function as explained in the experimental section. The direct bandgap of the samples shows no significant difference and the value is around 3.15 eV for all samples.

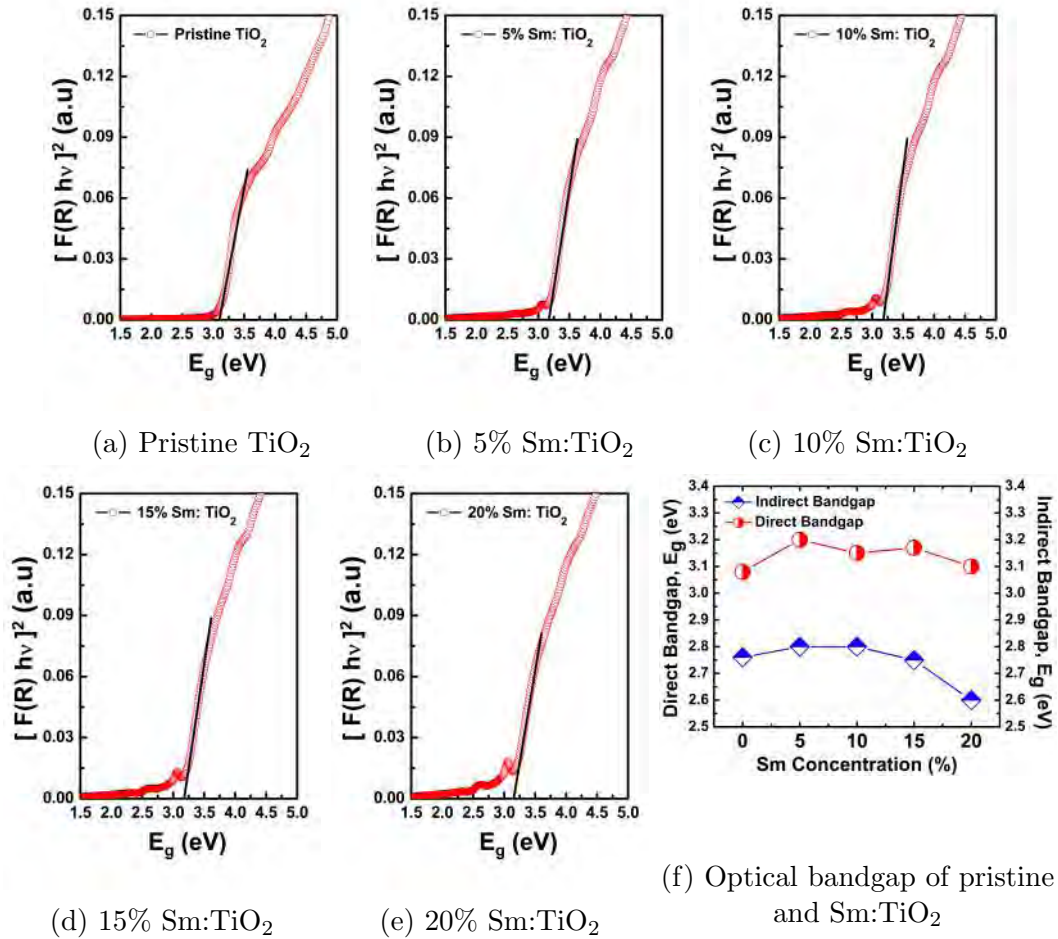


Figure 4.23: Optical bandgap of pristine and Sm:TiO₂ samples estimated by using Kubelka-Munk function

Photoluminescence spectra of pristine and Sm:TiO₂ samples were collected at room temperature using an excitation wavelength of 270 nm. A well-defined green emission peak at 545 nm (2.27 eV) was observed in all PL spectra which might be attributed to the recombination between mobile electrons trapped in the shallow trap centers originated by oxygen vacancies and holes at valence band [71, 72]. The broad peak at 415 nm (2.98 eV) and 456 nm (2.7 eV) in pristine TiO₂ sample could be attributed to the indirect transitions (X_{2a} to Γ_{1b} and Γ_{1b} to V_O) while the high energy peak at 335 nm (≈ 3.7 eV) in $Ti_{0.85}Sm_{0.15}O_2$ sample might be due to direct transition (X_{2b} to X_{1b}) [73].

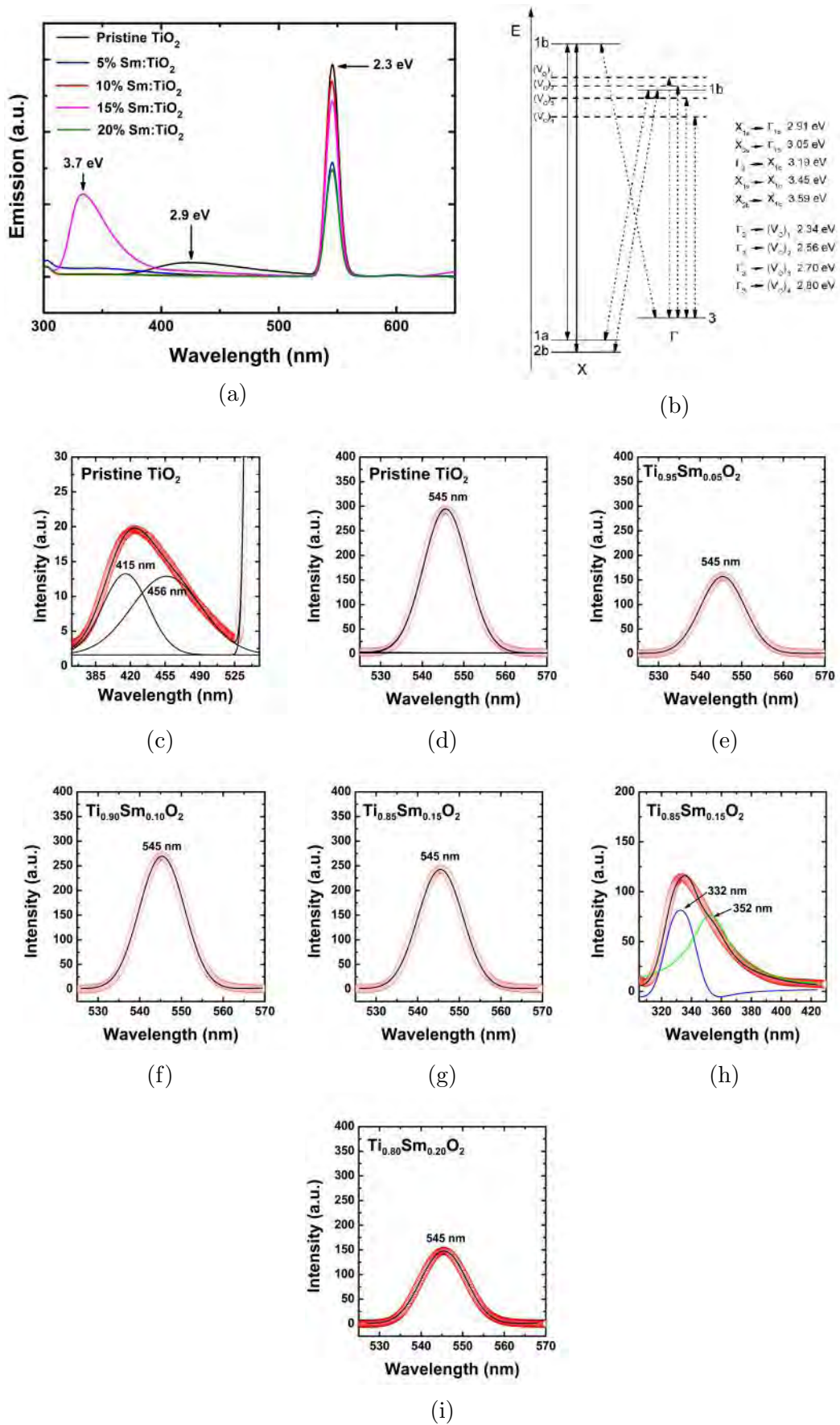


Figure 4.24: (a) Photoluminescence of Pristine TiO_2 and 5% Sm: TiO_2 (*excitation wavelength=270 nm*) (b) Energy level diagram of anatase TiO_2 (c-i) Fitted curve of PL spectra

However, the dominant PL emission at 2.27 eV is much lower than the optical bandgap (≈ 2.7 eV) estimated from UV-Visible spectroscopy of the samples. This implies electrons from valence band absorbed photon energy (≈ 2.7 eV) to reach the conduction band and then they might be trapped in shallow trap centers just below the conduction band while they loss ≈ 0.4 eV of energy and finally emit 2.3 eV of energy due to electron-hole recombination at valence band.

The intensity of this peak was found to be decreasing in the following order: pristine $TiO_2 > Ti_{0.90}Sm_{0.10}O_2 > Ti_{0.85}Sm_{0.15}O_2 > Ti_{0.95}Sm_{0.05}O_2 > Ti_{0.80}Sm_{0.20}O_2$ sample. Higher concentration of oxygen vacancies might be the reason of the decrease in the PL emission intensity in the $Sm : TiO_2$ samples because oxygen vacancies create shallow trap centers just below the conduction band which eventually trap the electrons and reduce the electron-hole recombination process [74]. In XPS of pristine TiO_2 and $Ti_{0.95}Sm_{0.05}O_2$ sample, the concentration of Ti^{3+} was estimated as 0.82% and 1.82% respectively which indicates concentration of oxygen vacancies in $Ti_{0.95}Sm_{0.05}O_2$ sample were higher than the pristine TiO_2 sample.

4.7 Magnetic property analysis by Vibrating Sample Magnetometer

Fig 4.25 to 4.29 shows room temperature M-H graphs of the pristine and Sm:TiO₂ samples. The comparison of M-H graphs of pristine TiO₂ sample shows that a small contribution of diamagnetic behavior was present for higher applied magnetic field ($>10,000$ Oe) at 300 K. The diamagnetic behavior of pristine TiO₂ has been reported several times in literature [75–80].

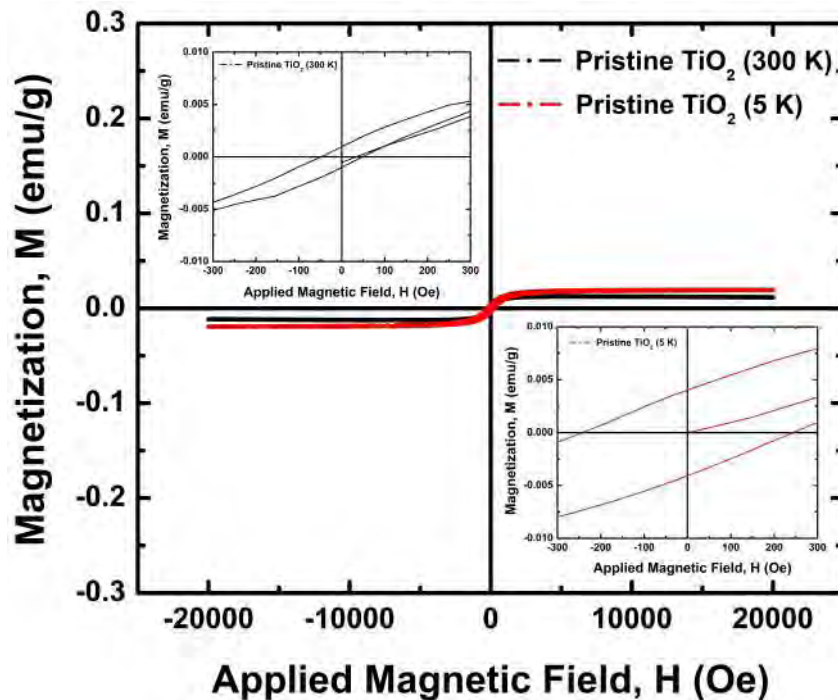


Figure 4.25: M-H graph of Pristine TiO₂

For Sm:TiO₂ samples, M-H graphs observed at 300 K indicate mostly ferromag-

netic behavior and the highest saturation magnetization was found for 5% Sm:TiO₂ sample (0.1 emu/g). At 5 K, the M-H graphs of the Sm:TiO₂ samples consist of both ferromagnetic and paramagnetic behavior. It's been noticed that the paramagnetic contribution was found to be higher with increase in Sm concentration in the samples.

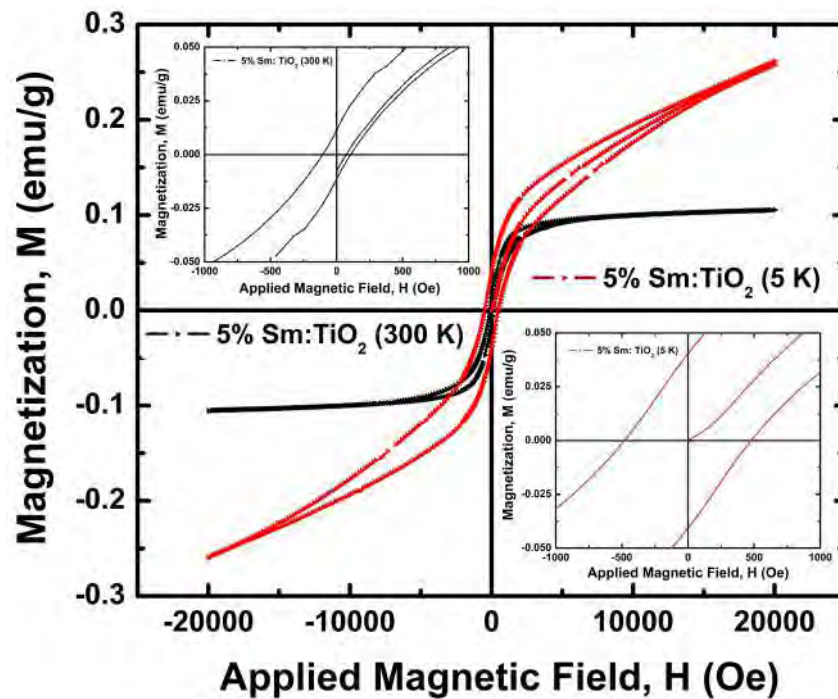


Figure 4.26: M-H graph of 5% Sm:TiO₂

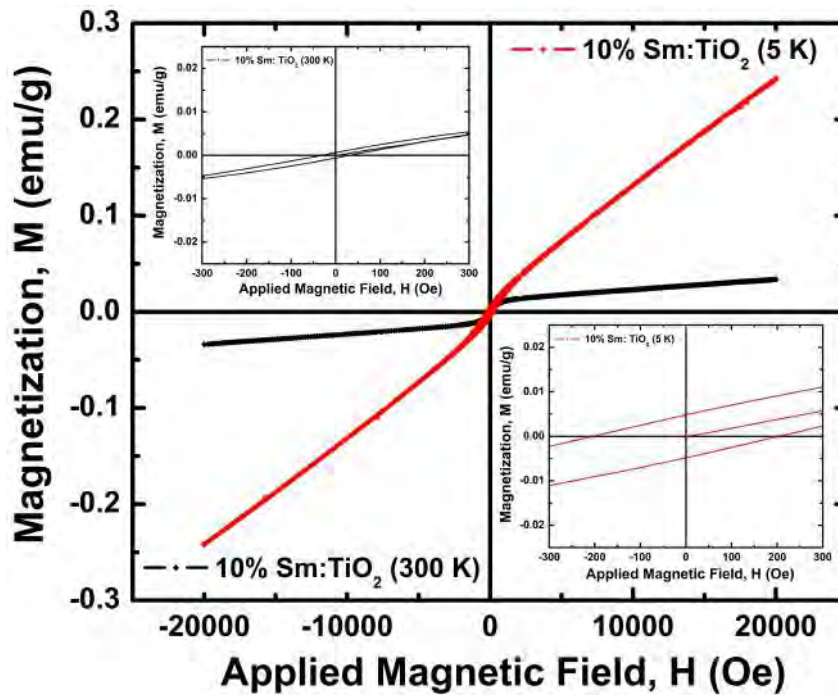


Figure 4.27: M-H graph of 10% Sm:TiO₂

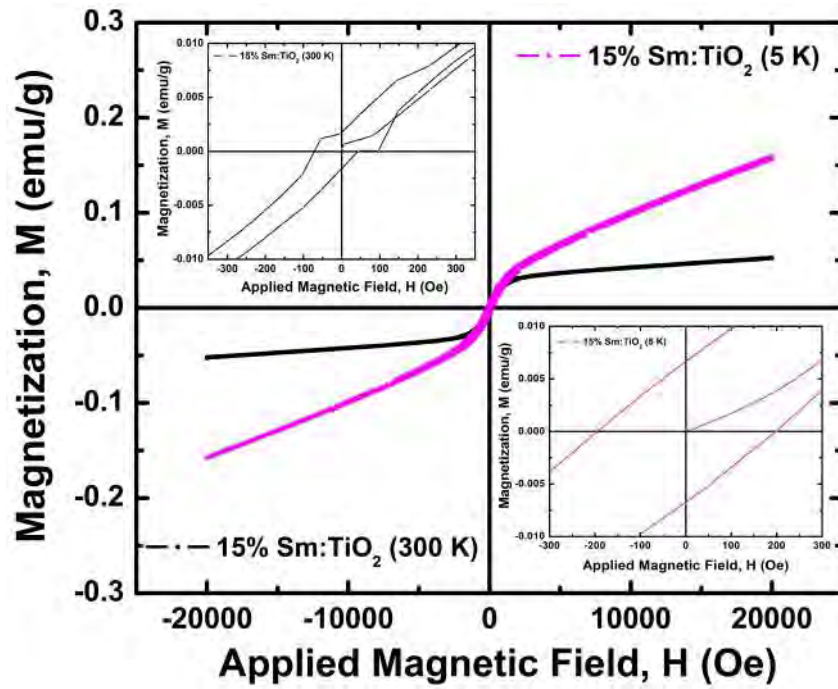


Figure 4.28: M-H graph of 15% Sm:TiO₂

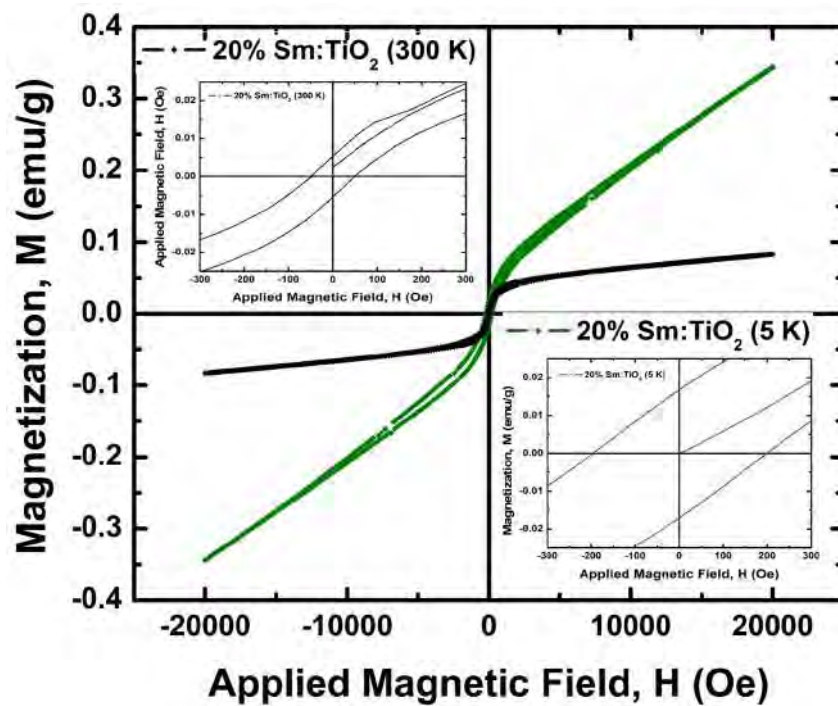
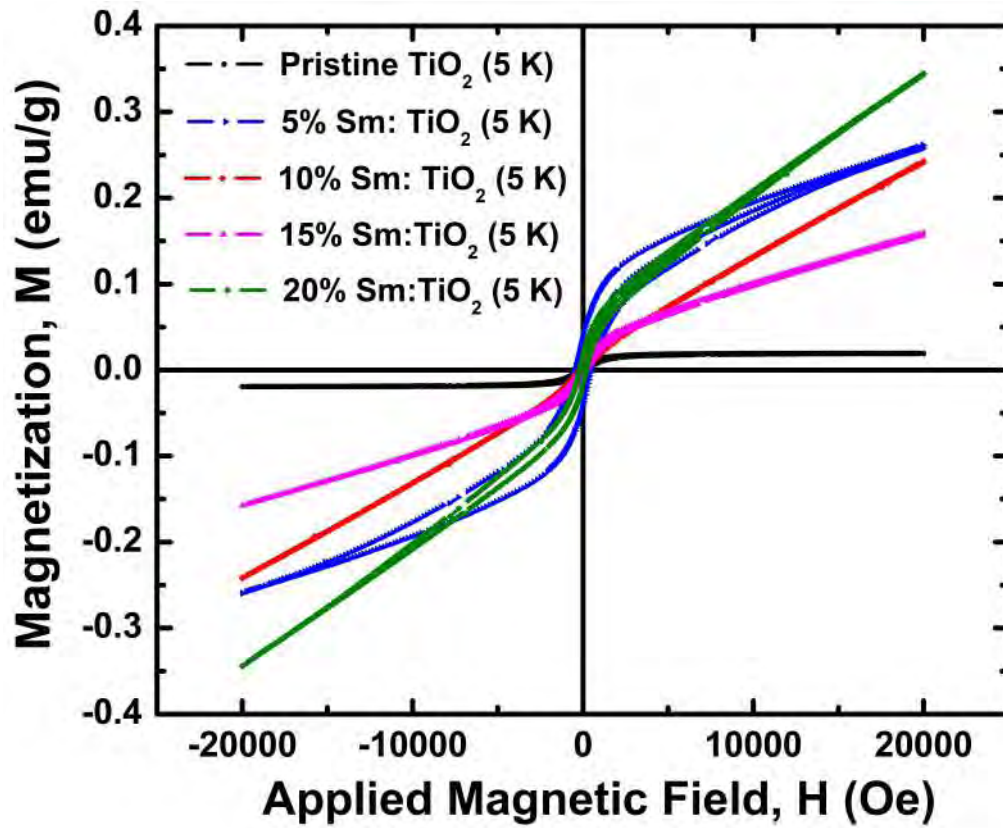
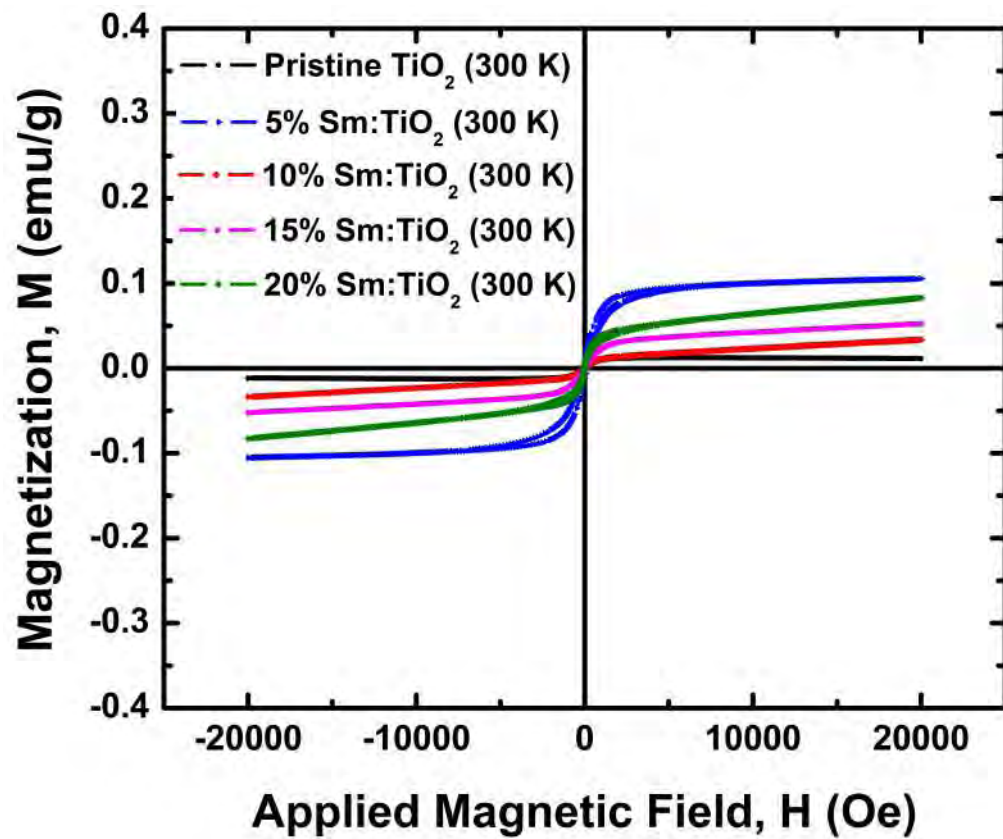


Figure 4.29: M-H graph of 20% Sm:TiO₂



(a)



(b)

Figure 4.30: Magnetization vs. applied field of pristine and Sm:TiO₂ samples at 5 K and 300 K

CHAPTER 5

CONCLUSIONS

The objective of this thesis was to investigate the role of oxygen vacancies on ferromagnetism in TiO_2 which is one of the most promising oxide dilute magnetic semiconductors. In order to create oxygen vacancies, Ti^{4+} was substituted by Sm^{3+} in TiO_2 nanoparticles which has $\sim 40\%$ larger ionic radius (109.8 pm) than Ti^{4+} (74.5 pm) ion. Due to this large variation in ionic radius, significant distortion in TiO_2 lattice is expected along with the suppression in grain growth and structural phase transition phenomena. Despite of the difference in ionic radius which indicates less solid solubility of Sm^{3+} in TiO_2 , high concentration of Sm (20 mol%) was added to investigate the formation of second phase of dopants and their effects in structural, optical and magnetic properties of Anatase TiO_2 beyond solid solubility limit. The salient features of this thesis may be summarized as follows:

- Pristine and Sm: TiO_2 (from 0 to 20 mol% Sm) nanoparticles were synthesized by solgel method.
- X-ray diffraction analysis showed that all Bragg peaks observed in the line scans of all samples were completely matched with Anatase phase of TiO_2 . Above 10 mol% of Sm substitution, a broad hump was detected in X-ray diffraction patterns which was identified as the amorphous Sm_2O_3 phase.
- The substitution of Sm was found to suppress the grain size from 53(± 10) nm of pristine Anatase to 10(± 3) nm of 20 mol% Sm substituted TiO_2 .
- High resolution TEM images and electron diffraction study showed that no metallic clusters of Sm^{3+} ions or crystalline Sm_2O_3 were present in the samples within the detection limit.
- SAED and STEM-EDX analysis posit that the amorphous Sm_2O_3 phase might be present as atomically thin layer around the Anatase phase.
- Optical property analysis by photoluminescence and UV-Vis-NIR spectroscopy suggest that all samples exhibit indirect bandgap and the Sm incorporation reduced the bandgap from 3.0 eV of pristine Anatase to 2.47 eV of 20 mol% Sm: TiO_2 sample.
- The Sm addition increased the concentration of oxygen vacancy which create shallow trap centers just below the conduction band. The presence of these

trap centers manifests the visible photoluminescence due to the recombination of mobile electrons in the trap centers with the holes in the valence band.

- Magnetization vs. applied field characteristics show that Sm:TiO₂ samples show dilute ferromagnetism at room temperature (300 K). At 5 K temperature, an evolution of paramagnetic behavior along with ferromagnetic response was noticed in the M-H graphs of all samples.

CHAPTER 6

SUGGESTIONS FOR FUTURE WORK

- Investigation of magnetization vs. applied field characteristics at several temperatures between 5 K and 300 K in order to understand the evolution of paramagnetic response along with ferromagnetic behavior.
- Investigation of temperature vs. resistivity from 5 K to 300 K in order to observe the semiconducting behavior of the pristine and Sm:TiO₂ samples.
- Investigation of photocatalytic dye degradation by pristine and Sm:TiO₂ samples under both UV and Visible light irradiation.
- Fabrication of Ti_(1-x)Sm_(x)O₂ ($0 \leq x \leq 5$) thin films and study the spin polarization by X-ray Magnetic Circular Dichroism (XMCD).

Bibliography

- [1] TC Kreutz, EG Gwinn, R Artzi, R Naaman, H Pizem, and CN Sukenik. Modification of ferromagnetism in semiconductors by molecular monolayers. *Applied physics letters*, 83(20):4211–4213, 2003.
- [2] Supriyo Datta and Biswajit Das. Electronic analog of the electro-optic modulator. *Applied Physics Letters*, 56(7):665–667, 1990.
- [3] S. Das Sarma, J. Fabian, X. Hu, and I. Zutic. Theoretical perspectives on spintronics and spin-polarized transport. *IEEE Transactions on Magnetics*, 36(5 I):2821–2826, 2000.
- [4] F Matsukura, H Ohno, A Shen, and Y Sugawara. Transport properties and origin of ferromagnetism in (Ga,Mn)As. *Physical Review B*, 57(4):R2037, 1998.
- [5] R. A. de Groot, F. M. Mueller, P. G. van Engen, and K. H. J. Buschow. New class of materials: Half-metallic ferromagnets. *Phys. Rev. Lett.*, 50:2024–2027, Jun 1983.
- [6] JMD Coey and M Venkatesan. Half-metallic ferromagnetism: Example of cro_2 . *Journal of Applied Physics*, 91(10):8345–8350, 2002.
- [7] Jacek K Furdyna. Diluted magnetic semiconductors. *Journal of Applied Physics*, 64(4):R29–R64, 1988.
- [8] H Munekata, H Ohno, S Von Molnar, Armin Segmüller, LL Chang, and L Esaki. Diluted magnetic iii-v semiconductors. *Physical Review Letters*, 63(17):1849, 1989.
- [9] Yuji Matsumoto, Makoto Murakami, Tomoji Shono, Tetsuya Hasegawa, Tomoteru Fukumura, Masashi Kawasaki, Parhat Ahmet, Toyohiro Chikyow, Shinya Koshihara, and Hideomi Koinuma. Room-temperature ferromagnetism in transparent transition metal-doped titanium dioxide. *Science*, 291(5505):854–856, 2001.
- [10] JB Yi, CC Lim, GZ Xing, HM Fan, LH Van, SL Huang, KS Yang, XL Huang, XB Qin, BY Wang, et al. Ferromagnetism in dilute magnetic semiconductors through defect engineering: Li-doped zno. *Physical review letters*, 104(13):137201, 2010.
- [11] Kenji Ueda, Hitoshi Tabata, and Tomoji Kawai. Magnetic and electric properties of transition-metal-doped zno films. *Applied Physics Letters*, 79(7):988–990, 2001.

- [12] SB Ogale, RJ Choudhary, JP Buban, SE Lofland, SR Shinde, SN Kale, VN Kulkarni, J Higgins, C Lanci, JR Simpson, et al. High temperature ferromagnetism with a giant magnetic moment in transparent co-doped $\text{SnO}_{2-\delta}$. *Physical Review Letters*, 91(7):077205, 2003.
- [13] John Philip, Nikoleta Theodoropoulou, Geetha Berera, Jagadeesh S Moodera, and Biswarup Satpati. High-temperature ferromagnetism in manganese-doped indium-tin oxide films. *Applied Physics Letters*, 85(5):777–779, 2004.
- [14] A Sundaresan, R Bhargavi, N Rangarajan, U Siddesh, and CNR Rao. Ferromagnetism as a universal feature of nanoparticles of the otherwise nonmagnetic oxides. *Physical Review B*, 74(16):161306, 2006.
- [15] Nguyen Hoa Hong, Joe Sakai, Nathalie Poirot, and Virginie Brizé. Room-temperature ferromagnetism observed in undoped semiconducting and insulating oxide thin films. *Physical Review B*, 73(13):132404, 2006.
- [16] M Venkatesan, CB Fitzgerald, and JMD Coey. Thin films: unexpected magnetism in a dielectric oxide. *Nature*, 430(7000):630, 2004.
- [17] James L Erskine and EA Stern. Calculation of the m 23 magneto-optical absorption spectrum of ferromagnetic nickel. *Physical Review B*, 12(11):5016, 1975.
- [18] Gerrit van der Laan, Bernard T Thole, George A Sawatzky, Jeroen B Goedkoop, John C Fuggle, Jean-Marc Esteve, Ramesh Karnatak, JP Remeika, and Hanna A Dabkowska. Experimental proof of magnetic x-ray dichroism. *Physical Review B*, 34(9):6529, 1986.
- [19] Fabrice Wilhelm. Magnetic materials probed with polarized x-ray spectroscopies, 2013.
- [20] Gerrit van der Laan and Adriana I Figueroa. X-ray magnetic circular dichroism—a versatile tool to study magnetism. *Coordination Chemistry Reviews*, 277:95–129, 2014.
- [21] T Hayashi, M Tanaka, T Nishinaga, and H Shimada. Magnetic and magnetotransport properties of new iii-v diluted magnetic semiconductors: Gmnas. *Journal of applied physics*, 81(8):4865–4867, 1997.
- [22] H Ohldag, V Solinus, FU Hillebrecht, JB Goedkoop, Marco Finazzi, F Matsukura, and H Ohno. Magnetic moment of mn in the ferromagnetic semiconductor ($\text{Ga}_{0.98}\text{Mn}_{0.02}$) as. *Applied Physics Letters*, 76(20):2928–2930, 2000.
- [23] M Khalid, Eugen Weschke, W Skorupa, M Helm, and Shengqiang Zhou. Ferromagnetism and impurity band in a magnetic semiconductor: Inmnp. *Physical Review B*, 89(12):121301, 2014.
- [24] MA Scarpulla, BL Cardozo, R Farshchi, WM Hlaing Oo, MD McCluskey, KM Yu, and OD Dubon. Ferromagnetism in $\text{Ga}_{(1-x)}\text{Mn}_x\text{P}$: evidence for inter-mn exchange mediated by localized holes within a detached impurity band. *Physical review letters*, 95(20):207204, 2005.

- [25] AX Gray, Jan Minar, S Ueda, PR Stone, Y Yamashita, J Fujii, J Braun, L Plucinski, CM Schneider, G Panaccione, et al. Bulk electronic structure of the dilute magnetic semiconductor $ga_{(1-x)}mn_xas$ through hard x-ray angle-resolved photoemission. *Nature materials*, 11(11):957, 2012.
- [26] Masaki Kobayashi, Iriya Muneta, Yukiharu Takeda, Yoshihisa Harada, Atsushi Fujimori, Juraj Krempaský, Thorsten Schmitt, Shinobu Ohya, Masaaki Tanaka, Masaharu Oshima, et al. Unveiling the impurity band induced ferromagnetism in the magnetic semiconductor (ga, mn) as. *Physical Review B*, 89(20):205204, 2014.
- [27] Slavomír Nemšák, Mathias Gehlmann, Cheng-Tai Kuo, Shih-Chieh Lin, Christoph Schlueter, Ewa Mlynczak, Tien-Lin Lee, Lukasz Plucinski, Hubert Ebert, Igor Di Marco, et al. Element-and momentum-resolved electronic structure of the dilute magnetic semiconductor manganese doped gallium arsenide. *Nature communications*, 9(1):3306, 2018.
- [28] Armela Keqi, Mathias Gehlmann, Giuseppina Conti, Slavomír Nemšák, Arunothai Rattanachata, Jan Minár, L Plucinski, Julien E Rault, Jean Pascal Rueff, M Scarpulla, et al. Electronic structure of the dilute magnetic semiconductor $ga_{(1-x)}mn_xp$ from hard x-ray photoelectron spectroscopy and angle-resolved photoemission. *Physical Review B*, 97(15):155149, 2018.
- [29] Lijuan Zhao, Bei Zhang, Qi Pang, Shihe Yang, Xixiang Zhang, Weikun Ge, and Jiannong Wang. Chemical synthesis and magnetic properties of dilute magnetic zn: Cr crystals. *Applied physics letters*, 89(9):092111, 2006.
- [30] A Haury, A Wasiela, A Arnoult, J Cibert, S Tatarenko, T Dietl, and Y Merle d'Aubigné. Observation of a ferromagnetic transition induced by two-dimensional hole gas in modulation-doped cdmnte quantum wells. *Physical Review Letters*, 79(3):511, 1997.
- [31] Kesong Yang, Rongqin Wu, Lei Shen, Yuan Ping Feng, Ying Dai, and Baibiao Huang. Origin of d 0 magnetism in ii-vi and iii-v semiconductors by substitutional doping at anion site. *Physical Review B*, 81(12):125211, 2010.
- [32] Tomasz Dietl. A ten-year perspective on dilute magnetic semiconductors and oxides. *Nature materials*, 9(12):965, 2010.
- [33] JMD Coey, M Venkatesan, and CB Fitzgerald. Donor impurity band exchange in dilute ferromagnetic oxides. *Nature materials*, 4(2):173, 2005.
- [34] J Philip, A Punnoose, BI Kim, KM Reddy, S Layne, JO Holmes, B Satpati, PR Leclair, TS Santos, and JS Moodera. Carrier-controlled ferromagnetism in transparent oxide semiconductors. *Nature materials*, 5(4):298, 2006.
- [35] JMD Coey. High-temperature ferromagnetism in dilute magnetic oxides. *Journal of applied physics*, 97(10):10D313, 2005.
- [36] Tomasz Dietl. Origin and control of ferromagnetism in dilute magnetic semiconductors and oxides. *Journal of Applied Physics*, 103(7):07D111, 2008.

- [37] JMD Coey and SA Chambers. Oxide dilute magnetic semiconductors—fact or fiction? *MRS bulletin*, 33(11):1053–1058, 2008.
- [38] Y Yamada, K Ueno, T Fukumura, HT Yuan, H Shimotani, Y Iwasa, L Gu, S Tsukimoto, Y Ikuhara, and M Kawasaki. Electrically induced ferromagnetism at room temperature in cobalt-doped titanium dioxide. *Science*, 332(6033):1065–1067, 2011.
- [39] H Saadaoui, X Luo, Z Salman, XY Cui, NN Bao, P Bao, RK Zheng, LT Tseng, YH Du, T Prokscha, et al. Intrinsic ferromagnetism in the diluted magnetic semiconductor co:tio 2. *Physical review letters*, 117(22):227202, 2016.
- [40] Zhihu Sun, Wensheng Yan, Guobin Zhang, Hiroyuki Oyanagi, Ziyu Wu, Qinghua Liu, Wenqing Wu, Tongfei Shi, Zhiyun Pan, Pengshou Xu, et al. Evidence of substitutional co ion clusters in zn 1- x co x o dilute magnetic semiconductors. *Physical Review B*, 77(24):245208, 2008.
- [41] N Sai Krishna, S Kaleemulla, G Amarendra, N Madhusudhana Rao, C Krishnamoorthi, M Kuppan, M Rigana Begam, D Sreekantha Reddy, and I Omkaram. Structural, optical, and magnetic properties of fe doped in2o3 powders. *Materials Research Bulletin*, 61:486–491, 2015.
- [42] Eva Pellicer, Enric Menendez, Jordina Fornell, Josep Nogues, Andre Van-tomme, Kristiaan Temst, and Jordi Sort. Mesoporous oxide-diluted magnetic semiconductors prepared by co implantation in nanocast 3d-ordered in_2o_{3-y} materials. *The Journal of Physical Chemistry C*, 117(33):17084–17091, 2013.
- [43] Shokouh S Farvid, Manu Hegde, and Pavle V Radovanovic. Influence of the host lattice electronic structure on dilute magnetic interactions in polymorphic cr (iii)-doped in2o3 nanocrystals. *Chemistry of Materials*, 25(2):233–244, 2013.
- [44] Kuang Hong Gao, Zhi Qing Li, Tao Du, En Yong Jiang, and Yang Xian Li. Ferromagnetic properties of bulk $cu_{(1-x)}mn_xo$ magnetic semiconductors. *Physical Review B*, 75(17):174444, 2007.
- [45] A Thurber, KM Reddy, V Shutthanandan, Mark H Engelhard, C Wang, Jason Hays, and Alex Punnoose. Ferromagnetism in chemically synthesized ceo_2 nanoparticles by ni doping. *Physical Review B*, 76(16):165206, 2007.
- [46] Vinod K Paidi, Dale L Brewé, John W Freeland, Charles A Roberts, and Johan van Lierop. Role of ce 4 f hybridization in the origin of magnetism in nanoceria. *Physical Review B*, 99(18):180403, 2019.
- [47] T Ohtsuki, A Chainani, Ritsuko Eguchi, M Matsunami, Y Takata, M Taguchi, Y Nishino, K Tamasaku, M Yabashi, T Ishikawa, et al. role of ti 3d carriers in mediating the ferromagnetism of co:tio2 anatase thin films. *Physical review letters*, 106(4):047602, 2011.
- [48] Tiffany C Kaspar, T Droubay, V Shutthanandan, Steve M Heald, Chong M Wang, David E McCreedy, Suntharampillai Thevuthasan, JD Bryan, Daniel R Gamelin, AJ Kellock, et al. Ferromagnetism and structure of epitaxial cr-doped anatase tio 2 thin films. *Physical Review B*, 73(15):155327, 2006.

- [49] Talita E de Souza, Alexandre Mesquita, Angela O de Zevallos, Fanny Beron, Kleber R Pirota, Person P Neves, Antonio C Doriguetto, and Hugo B de Carvalho. Structural and magnetic properties of dilute magnetic oxide based on nanostructured co-doped anatase TiO_2 ($\text{Ti}_{(1-x)}\text{Co}_x\text{O}_{2-\delta}$). *The Journal of Physical Chemistry C*, 117(25):13252–13260, 2013.
- [50] Md Abdullah Al Mamun, Manifa Noor, AKM Atique Ullah, Md Sarowar Hosain, Matin Abdul, Fakhrul Islam, and MA Hakim. Effect of CeO₄ on structural, magnetic and optical properties of ceria nanoparticles. *Materials Research Express*, 6(1):016102, 2018.
- [51] J Daniel Bryan, Steven A Santangelo, Sean C Keveren, and Daniel R Gamelin. Activation of high- T_c ferromagnetism in Co^{2+} : TiO_2 and Cr^{3+} : TiO_2 nanorods and nanocrystals by grain boundary defects. *Journal of the American Chemical Society*, 127(44):15568–15574, 2005.
- [52] Biswajit Choudhury and Amarjyoti Choudhury. Oxygen vacancy and dopant concentration dependent magnetic properties of Mn doped TiO_2 nanoparticle. *Current Applied Physics*, 13(6):1025–1031, 2013.
- [53] Batakrushna Santara, PK Giri, Soumen Dhara, Kenji Imakita, and Minoru Fujii. Oxygen vacancy-mediated enhanced ferromagnetism in undoped and Fe-doped TiO_2 nanoribbons. *Journal of Physics D: Applied Physics*, 47(23):235304, 2014.
- [54] Shih-Yun Chen, Yi-Hsing Lu, Tzu-Wen Huang, Der-Chung Yan, and Chung-Li Dong. Oxygen vacancy dependent magnetism of CeO₂ nanoparticles prepared by thermal decomposition method. *The Journal of Physical Chemistry C*, 114(46):19576–19581, 2010.
- [55] GS Chang, J Forrest, EZ Kurmaev, AN Morozovska, MD Glinchuk, JA McLeod, A Moewes, TP Surkova, and Nguyen Hoa Hong. Oxygen-vacancy-induced ferromagnetism in undoped SnO_2 thin films. *Physical Review B*, 85(16):165319, 2012.
- [56] Hyeon-Jun Lee, Se-Young Jeong, Chae Ryong Cho, and Chul Hong Park. Study of diluted magnetic semiconductor: Co-doped ZnO. *Applied Physics Letters*, 81(21):4020–4022, 2002.
- [57] Nguyen Hoa Hong, Joe Sakai, Ngo Thu Huong, Nathalie Poirot, and Antoine Ruyter. Role of defects in tuning ferromagnetism in diluted magnetic oxide thin films. *Physical Review B*, 72(4):045336, 2005.
- [58] V Fernandes, RJO Mossaneck, P Schio, JJ Klein, AJA De Oliveira, WA Ortiz, N Mattoso, J Varalda, WH Schreiner, M Abbate, et al. Dilute-defect magnetism: Origin of magnetism in nanocrystalline CeO₂. *Physical Review B*, 80(3):035202, 2009.
- [59] NV Skorodumova, SI Simak, Bengt I Lundqvist, IA Abrikosov, and Börje Johansson. Quantum origin of the oxygen storage capability of ceria. *Physical Review Letters*, 89(16):166601, 2002.

- [60] Norifusa Satoh, Toshio Nakashima, and Kimihisa Yamamoto. Metastability of anatase: size dependent and irreversible anatase-rutile phase transition in atomic-level precise titania. *Scientific reports*, 3:1959, 2013.
- [61] Qi Xiao, Zhichun Si, Zhiming Yu, and Guanzhou Qiu. Sol-gel auto-combustion synthesis of samarium-doped tio₂ nanoparticles and their photocatalytic activity under visible light irradiation. *Materials Science and Engineering: B*, 137(1-3):189–194, 2007.
- [62] Yuechan Cao, Zongyan Zhao, Juan Yi, Chenshuo Ma, Dacheng Zhou, Rongfei Wang, Chen Li, and Jianbei Qiu. Luminescence properties of sm³⁺-doped tio₂ nanoparticles: Synthesis, characterization, and mechanism. *Journal of Alloys and Compounds*, 554:12–20, 2013.
- [63] Jianwen Shi, Jingtang Zheng, Yan Hu, and Yucui Zhao. Photocatalytic degradation of methyl orange in water by samarium-doped tio₂. *Environmental Engineering Science*, 25(4):489–496, 2008.
- [64] Lanying Hu, Hongwei Song, Guohui Pan, Bin Yan, Ruifei Qin, Qilin Dai, Libo Fan, Suwen Li, and Xue Bai. Photoluminescence properties of samarium-doped tio₂ semiconductor nanocrystalline powders. *Journal of Luminescence*, 127(2):371–376, 2007.
- [65] V Kiisk, I Sildos, S Lange, V Reedo, T Tätte, M Kirm, and J Aarik. Photoluminescence characterization of pure and sm³⁺-doped thin metaloxide films. *Applied Surface Science*, 247(1-4):412–417, 2005.
- [66] Dong Jin Park, Tohru Sekino, Satoshi Tsukuda, Asuka Hayashi, Takafumi Kusunose, and Shun-Ichiro Tanaka. Photoluminescence of samarium-doped tio₂ nanotubes. *Journal of Solid State Chemistry*, 184(10):2695–2700, 2011.
- [67] V Aware Dinkar, S Jadhav Shridhar, E Navgire Madhukar, E Athare Anil, and H Kolhe Nitin. Sm-doped tio₂ nanoparticles with high photocatalytic activity for ars dye under visible light synthesized by ultrasonic assisted sol-gel method. *Oriental Journal of Chemistry*, 32(2):933–940, 2016.
- [68] Yunfei Ma, Jinlong Zhang, Baozhu Tian, Feng Chen, and Lingzhi Wang. Synthesis and characterization of thermally stable sm, n co-doped tio₂ with highly visible light activity. *Journal of Hazardous Materials*, 182(1-3):386–393, 2010.
- [69] Yan Xiang, Zhu Ma, Jia Zhuang, Honglin Lu, Chunyang Jia, Junsheng Luo, Haimin Li, and Xiaowei Cheng. Enhanced performance for planar perovskite solar cells with samarium-doped tio₂ compact electron transport layers. *The Journal of Physical Chemistry C*, 121(37):20150–20157, 2017.
- [70] Li-Ting Tseng, Xi Luo, Sean Li, and Jiabao Yi. Magnetic properties of sm-doped rutile tio₂ nanorods. *Journal of Alloys and Compounds*, 687:294–299, 2016.
- [71] Tri Tuan Nguyen, Tran Thanh Tung, Dusan Losic, Luu Thi Lan Anh, Xuan Sang Nguyen, et al. Electromigration with enhanced green emission in the titanium dioxide nanotube/graphene composite. *Current Applied Physics*, 19(10):1082–1087, 2019.

- [72] MD Dramićanin, Ž Antić, Sanja Čulubrk, Scott Phillip Ahrenkiel, and JM Nedeljković. Self-referenced luminescence thermometry with sm³⁺ doped tio₂ nanoparticles. *Nanotechnology*, 25(48):485501, 2014.
- [73] Nadica D Abazović, Mirjana I Čomor, Miroslav D Dramićanin, Dragana J Jovanović, S Phillip Ahrenkiel, and Jovan M Nedeljković. Photoluminescence of anatase and rutile tio₂ particles. *The Journal of Physical Chemistry B*, 110(50):25366–25370, 2006.
- [74] Hao Peng, Ruitang Guo, and He Lin. Photocatalytic reduction of co₂ over sm-doped tio₂ nanoparticles. *Journal of Rare Earths*, 2019.
- [75] Shyamsundar Ghosh and PMG Nambissan. Evidence of oxygen and ti vacancy induced ferromagnetism in post-annealed undoped anatase tio₂ nanocrystals: A spectroscopic analysis. *Journal of Solid State Chemistry*, 275:174–180, 2019.
- [76] Li-Ting Tseng, Xi Luo, Nina Bao, Jun Ding, Sean Li, and Jiabao Yi. Structures and properties of transition-metal-doped tio₂ nanorods. *Materials Letters*, 170:142–146, 2016.
- [77] JMD Coey, P Stamenov, RD Gunning, M Venkatesan, and K Paul. Ferromagnetism in defect-ridden oxides and related materials. *New Journal of Physics*, 12(5):053025, 2010.
- [78] Lu Li, Yan Chen, Shihui Jiao, Zhenxing Fang, Xu Liu, Ye Xu, Gangsheng Pang, and Shouhua Feng. Synthesis, microstructure, and properties of black anatase and b phase tio₂ nanoparticles. *Materials & Design*, 100:235–240, 2016.
- [79] Li-Ting Tseng, Xi Luo, Thiam Teck Tan, Sean Li, and Jiabao Yi. Doping concentration dependence of microstructure and magnetic behaviours in co-doped tio₂ nanorods. *Nanoscale research letters*, 9(1):673, 2014.
- [80] Le Zhang, Liping Zhu, Liang Hu, Yaguang Li, Hui Song, and Zhizhen Ye. Interfacial effect on mn-doped tio₂ nanoparticles: from paramagnetism to ferromagnetism. *RSC Advances*, 6(62):57403–57408, 2016.